Characterisation and Development of Nanostructured, Ultrahigh Strength, and Ductile Bainitic Steels

By
Mohamed Y. Sherif
St. Edmund's College, Cambridge

University of Cambridge
Department of Materials Science and Metallurgy
Pembroke Street, Cambridge CB2 3QZ

A dissertation submitted for the
degree of Doctor of Philosophy
at the University of Cambridge
January 2006

To Amin Maalouf

PREFACE

This dissertation is submitted for the degree of Doctor of Philosophy at the University of Cambridge. The research reported herein was conducted under the supervision of Professor H. K. D. H. Bhadeshia in the Department of Materials Science and Metallurgy, University of Cambridge, between October 2003 and October 2005.

This work is to the best of my knowledge original, except where acknowledgement and references are made to previous work. Neither this, nor any substantially similar dissertation has been or is being submitted for any degree, diploma or other qualification at any other university or institution. This dissertation does not exceed the word limit of 60,000 words.

Part of this work has been submitted to appear in the following publication:

M. Y. Sherif and P. P. Chattopadhyay. Microstructure and Mechanical Properties of Bainite-containing Silicon-containing Low-alloy Steels. *Int. Mater. Rev.*, 2005.

Mohamed Sherif

January 2006

ACKNOWLEDGEMENTS

I would like to express my sincere thanks to my supervisor Professor H. K. D. H. Bhadeshia for his support and guidance. I am grateful to Dr P. P. Chattopadhyay for his endless support and encouragement.

I acknowledge financial support from Cambridge Overseas Trust, Trinity College, for providing me the opportunity to pursue research at the University of Cambridge during the last three years. I am greatly indebted to BP Egypt, in particular Mrs Manal Shaheen. This work would not have been possible without financial support from Volvo Technical Development AB, Sweden.

I am grateful to Dr Mary Vickers for numerous fruitful discussions, Kevin, Robert, Brian and other members of the Materials Science Department for their continuous help and friendship. I owe thanks to Drs Javier Santisteban and Edward Oliver, ENGIN-X instrument scientists at ISIS Pulsed Neutron & Muon Source, Didcot, for their help. Special thanks are due to (Ed) whom we had to call in the early hours of the day very often!

I am indebted to Professor M. M. I. Hammouda, Al-azhar University, Cairo, Egypt, for his encouragement and inspiration for studying for the PhD degree at Cambridge.

I wish to thank PT-Group members, in particular Dr Carlos García-Mateo, Pippa, Mathew (Santi), Sourabh & Saurabh, Dr Howard Stone, Richard and Kazu for making my stay at Cambridge an enjoyable one.

I wish to express my thanks to all my friends with special thanks to Akram, Chiho, Merav, Helen, Katerina, Kathy, Sultan, Emel, Mustapha, Zippy, Joachim and Monika, Stéphane, Audrey, Sophie, Shigeki and Sangeeta.

I would like to thank Richard Stallman (RMS) for founding the GNU project from which I have been benefiting enormously.

I was very lucky indeed to meet Sisters Gemma and Josette, Jennifer, Clare, Simon, Frances, Ana and many other wonderful people in St. Edmund's College.

I am greatly indebted to my parents and family for their support, devotion and understanding throughout my life.

ABSTRACT

The purpose of the present work was to characterise and further develop a novel nanostructured type of bainitic steel. Three chemical compositions were considered with different concentrations of Al and Co. The addition of Al and Co is believed to be necessary to produce the desired nanostructure at very low temperatures within a reasonable transformation time.

An overview of the mechanical performance of fully bainitic steels *vs* other steel systems is presented in Chapter 1. An introduction to metallurgical concepts regarding the design and performance of bainite steels is presented in Chapters 1 and 2.

Chapter 2 focuses on the design concepts by which the steel chemical composition was optimised, primarily on the basis of cost and the avoidance of carbide precipitation.

Chapter 3 deals with the evolution of the microstructure during uniaxial tension, studied using X-ray diffraction. The effect of tempering deformed and undeformed structures, and heating to high temperatures, have also been investigated. In this context, data on bainite-containing steels in the literature are found to be rather limited.

Chapter 4 is a comprehensive assessment of the mechanical behaviour of the steels subjected to a variety of processing routes. It is demonstrated that it is possible to outperform current commercially available steels.

The microstructural behaviour of strain-aged and as-transformed steels during uniaxial tension studied using *in situ* neutron diffraction is described in Chapter 5. The evolution of texture with plastic deformation was confirmed as previously observed using conventional X-ray analysis. Evidence regarding the presence of two populations of carbon depleted and carbon-rich austenite and their response to strain, grain rotation, anisotropy, stress partitioning between phases and the lack of work-hardening to overcome the onset of necking are presented.

Contents

Nomenclature

$(\frac{1+\cos^2 2\theta}{\sin^2\theta\cos\theta})$	Lorentz-polarisation factor
2ζ	Effective lattice microstrain
α	Ferrite
α_{1-2}	α_1 peak shift caused by α_2
$\alpha(T)$	The degree of thermal reaction
α_p	The probability of deformation-fault formation between two FCC crystal layers
β	Integral peak breadth
β_{inst}	Instrumental broadening
β_{obs}	The observed integral breadth
β_{size}	The integral breadth contribution due to fine crystallites
β_{strain}	The integral breadth contribution due to lattice non-uniform microstrain
β_{tot}	The total integral breadth
$\Delta 2\theta$	Peak shift, in radians
$\Delta G^{\gamma\alpha}$	The driving force for the bainite transformation
$\Delta G^{\alpha^{'}\gamma}$	The magnitude of the driving force for the martensite transformation
ΔG_M	The magnetic free energy component of the transformation $\gamma \rightarrow \alpha$ in pure iron

ΔG_{NM}	As ΔG_M, but non-magnetic
ΔT_M	The magnetic temperature change caused by a unit change in substitutional solute concentration
ΔT_{NM}	As ΔT_M, but non-magnetic
Δ	Error minimisation function
η	The mixing parameter which determines Lorentzian and Gaussian components in a peak width
γ	Austenite
λ	X-ray radiation wavelength
V	Unit cell volume
Φ	The heating rate, DSC–scanning mode
ϕ_l	A function represents the line profile
σ_t	True stress
θ_i	Bragg angle of the ith reflection
ε	Strain
ε_t	True strain
ε_{hkl}	The elastic lattice strain of the hkl line
ϑ	The angle between the scattering vector and the normal to the crystallites in March-Dollase function
A	The absorption factor
a	Fitting parameter
a_0	Error-corrected lattice parameter
a_γ	Austenite lattice parameter
A_{e1}	The temperature separating α and α+γ phase fields

A_{e3}	The temperature separating α+γ and γ phase fields
a_{α_b}	Bainitic-ferrite lattice parameter
b	Fitting parameter
b_i^{tot}	Total background intensity
B_S	Bainite-start temperature
c_p	The apparent specific heat capacity
C_γ	Austenite carbon content
$C_{T_0'}$	The austenite carbon content given by the $T_0^{'}$ boundary
D	Crystallite size
$d^*(\text{calculated})_i$	Calculated interplanar spacings
$d^*(\text{observed})_i$	Observed interplanar spacings
d_0	Equilibrium interplanar spacing
d_i	The interplanar spacing of the ith reflection
d_{hkl}	Measured lattice-plane spacing
d_{hkl}^0	The stress-free lattice-plane spacing
E	The activation energy
e^{-2M}	The temperature factor
F_K	The structure factor
F_N	Figure of merit
G	The Gaussian component in a peak width
G_1	A refinable parameter in March-Dollase function
h	Planck's constant
hkl	Miller indices

I_{hkl}	The integrated intensity of the *hkl* reflection
I_{α_b}	Bainitic-ferrite line intensity
K	Represents Miller indices (hkl) of a Bragg reflection
k	A constant (equation 1.9)
k_1	A constant in Sherif *et al.* model
k_P	An empirical constant related to the mechanical stability of retained austenite
K_s	The shape factor
k_γ	An empirical constant in Sugimoto *et al.* model
K_{IC}	Fracture toughness
L	The Lorentzian component in a peak width
L_K	A factor contains Lorentz-polarisation and multiplicity factors
L_n	Neutron flight-path
m	Number of refinable parameters in Rietveld method
M_d	The temperature above which no austenite transformation takes place
m_n	Neutron rest-mass
M_S	Martensite-start temperature
m_s	Sample mass, DSC
N	Number of reflection lines
n	Number of the observed peaks of a phase
N_{poss}	Number of possible reflection lines
P	The strain exponent, related to the autocatalytic effect
p	The multiplicity factor

P^*	The texture parameter
P_K	Preferred orientation function
Q_0	The heat flow rate corresponding to the zero-line
Q_a	The parallel scattering vector
Q_i	Quantities used in the least-squares refinement for eliminating peak shifts errors
Q_m	The measured heat flow rate
Q_t	The transverse scattering vector
Q_{bl}	The baseline of a thermal reaction peak
$Q_{i,ex}$	A polynomial function used to extrapolate part of the measured curve in DSC at T_i
$Q_{f,ex}$	Same as $Q_{i,ex}$, but at T_f
R	The gas constant
R_g	The radius of the goniometer
R_{min}	The minimised R-factor, indicative of the goodness-of-fit in the software package PHILIPS ProFit
S	Specimen displacement relative to the goniometer axis
s	The scale factor
S_y	The residual in the intensity refinement function
t	Time-of-flight
T_0	The temperature at which both bainitic ferrite and austenite of similar composition have identical free energy
$T_0^{'}$	As the T_0 temperature but with accounting for stored energy in bainite

T_f	The final peak-temperature
T_i	The initial peak-temperature
T_p	The peak-maximum temperature
$T_{f'}$	The temperature at which a certain degree of phase transformation is attained
U	Caglioti parameter
V	Caglioti parameter
$V_{\gamma-B}$	Volume fraction of blocky austenite
$V_{\gamma-f}$	Volume fraction of thin film austenite
V_γ	Austenite volume fraction
V_γ^0	Initial austenite volume fraction
V_{α_b}	Bainite volume fraction
$V_{\alpha_b}^{max}$	Maximum volume fraction of bainite
W	Caglioti parameter
w_i	The weight assigned to reflection line i in the error minimisation function
x	A unit concentration of substitutional solute
$\bar{x}$	Alloy average carbon concentration
x_c	Carbon atomic fraction
x_{α_b}	Carbon concentration of the bainitic ferrite
y_i	The total observed intensity at step i
y_{bi}	Background intensity at step i
y_{ci}	Calculated intensity at step i

$\alpha^{'}$	Martensite
α_b	Bainitic ferrite
d_{ni}	Refined interplanar spacings
r_i	The reciprocal of y_i
2θ	Scanned range in degrees using X-ray diffraction
AD	The axial divergence error
CIF	Crystallographic information file
DE	Sample displacement error (figure 3.2)
DP	Dual-phase steel
DSC	Differential scanning calorimetry
FCC	Face-centred cubic
FS	Peak shift error due to flat specimen
FWHM	Full width at half maximum
GOF	Goodness-of-fit
HV	Vickers hardness
M	Martensitic steel
n_{incr}	The incremental strain hardening exponent
ppm	Parts per million, by weight
PSD	Position sensitive detector
Q&P	Quenching and partitioning process
R	The peak shift error caused by the displacement of the receiving slit
SEM	Scanning electron microscope
T	The peak shift error due to sample transparency

TE	Total elongation
TEM	Transmission electron microscopy
TRIP	Transformation induced plasticity
UE	Uniform elongation
UTS	Ultimate tensile strength, also TS
YR	Yield ratio
YS	Yield strength
Z	The zero-angle calibration error

Chapter 1

Bainitic Steels—Literature Review

Bainite[†] is a non-equilibrium transformation product of austenite which evolves by cooling at rates such that the diffusion-controlled transformations such as pearlite are not possible, yet the cooling is sufficiently slow to avoid the diffusionless transformation into athermal martensite.

Bainitic microstructures are generally described as non-lamellar aggregates of carbides and plate-shaped ferrite. As shown in figure 1.1, bainite can be classified according to morphology to upper and lower bainite. Upper bainite consists of clusters of platelets of ferrite which share identical crystallographic orientation which are intimately connected to the parent austenite phase in which they grow. An average bainitic ferrite plate is about 10 μm long and 0.2 μm thick [1]. Elongated cementite particles decorate the boundaries of these plates; the amount and continuity of the cementite layer depends on the steel carbon concentration.

As the transformation temperature is reduced some of the carbon precipitates within the ferrite plates as cementite leading to the lower-bainite structure.

The mechanism of the bainite transformation has been a subject to controversy and discussing different schools of thought in detail is beyond the scope of the present work. However, a brief presentation is unavoidable so as to point out to some relevant aspects of mechanisms which are discussed

---

[†] Bainite or bainitic ferrite is henceforth referred to as α_b.

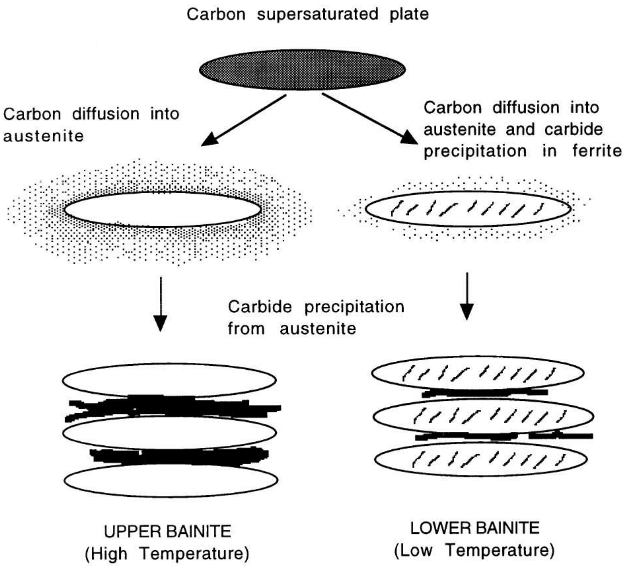

Figure 1.1: Illustration of upper and lower bainite showing the main differences in carbon partitioning and precipitation [2].

in the literature.

1.1 Bainite Transformation Mechanism

Austenite transformation products which form below the temperature of reconstructive transformations are identified as Widmanstätten ferrite, bainite and martensite. The bainite phase is observed at temperatures lower than that necessary for Widmanstätten ferrite to form.

Surface relief as a result of transformation has been observed in steels that undergo either the Widmanstätten ferrite or bainite transformation. However, the crucial aspect concerning the evolution of these intermediate displacive transformation products is the kinetics associated with carbon partitioning. The equilibrium carbon content of ferrite is usually much less than that of austenite.

Bhadeshia envisaged that the nature of the bainite nucleus is similar to that of Widmanstätten ferrite [1]. Unlike Widmanstätten ferrite, carbon diffuses into the residual austenite not during but *after* bainite plate growth. Therefore, the thermodynamic conditions accompanying growth must be the determining factor for a nucleus to evolve either to Widmanstätten ferrite or bainite. If diffusionless growth cannot be sustained, the formation of Widmanstätten ferrite takes place instead of bainite. A stored energy in Widmanstätten ferrite of about 50 J mol^{-1} has been assumed [3], compared with that for bainite at around 400 J mol^{-1}. The chemical free energy change has to be sufficient as to exceed the stored energy for a transformation to take place.

The much higher stored energy in bainite was rationalised on the basis of the absence of favourable strain interactions 'within' bainite sheaves [3].

Hillert argued that the assumed high stored energy in bainite requires high growth velocity which has not been observed experimentally, consequently, carbon supersaturation in bainitic ferrite bears 'no conclusive evidence' [4]. In this context, Oblak and Hehemann had earlier proposed that bainite growth is rapid though occurs in short steps [5].

Hillert adopted the basic bainite transformation model suggested by Hultgren [6], in which, bainite was assumed to form initially as Widmanstätten ferrite plates 'followed by the formation of a mixture of ferrite and cementite in the interjacent spaces.' [4]. Hillert argued that in eutectoid Fe-C alloys, at low temperatures, bainite is promoted over pearlite not due to a martensite-like transformation mode, but rather is related to the high asymmetry in the Fe-C phase diagram [4]. It was suggested that 'The edgewise growth mechanism [of bainite] is the same as for Widmanstätten ferrite' with carbon diffusion controlling growth velocity [4]. As the transformation temperature is lowered, the formation of carbides is enhanced which 'may speed up the edgewise growth.' [4]. The carbides precipitation occurs in the vicinity of advancing bainite plate-tips which results in a 'shorter diffusion distances for carbon away from the advancing tip' [4].

Aaronson *et al.*, have argued in favour of the short-range diffusion of carbon to be the predominant aspect of the bainite transformation mechanism [7].

However, although bainite transformation was assumed to be *martensitic*, proposed carbon diffusion at the γ/α_b interface was believed to cause an increase in the free energy change thereby facilitating the formation of bainite above the M_S temperature [8].

Speer *et al.* have suggested that bainite may grow by a martensite-like growth mechanism which is diffusionless 'followed by, or along with, carbon partitioning into austenite.' [9, 10], with overall kinetics controlled by carbon diffusion, *i.e.* the growth mechanism is both "fully' displacive and 'fully' diffusional.'.
This growth mechanism was also proposed by Muddle and Nie [11] and Saha *et al.* [12].

1.2 The T_0 Concept

"Fully" bainitic steels are free from allotriomorphic ferrite and almost free from athermal martensite. The structure is thus composed of retained austenite, bainitic ferrite and carbides. Carbides, however, can be suppressed by alloying with elements such as Si, Al and P. It is essential to understand the issues governing the formation of carbides in bainite in different varieties of steel and the mechanical properties achievable thereof in greater detail.

As shown in figure 1.2, bainite growth by a diffusionless mechanism has to occur at a temperature just below T_0, when the free energy of bainitic ferrite falls below that of austenite of same composition [13].

The stored energy in bainitic ferrite is accounted for by raising its free energy curve by an amount equal to the strain energy due to transformation, giving the $T_0^{'}$ curve (figure 1.2). During isothermal transformation the excess carbon in the bainite partitions into the residual austenite, forcing the next plate to grow from carbon-enriched austenite [1]. The process finally ceases as the austenite carbon content reaches $T_0^{'}$ value, leading to the so-called 'the incomplete reaction phenomenon' [14]. It is important to realise that this scenario is valid only for carbide-free bainitic steels.

Application of the lever-rule allows the estimation of the maximum fraction of bainite ($V_{\alpha_b}^{max}$) at any temperature:

$$V_{\alpha_b}^{max} = \frac{C_{T_0^{'}} - \bar{x}}{C_{T_0^{'}} - x_{\alpha_b}} \tag{1.1}$$

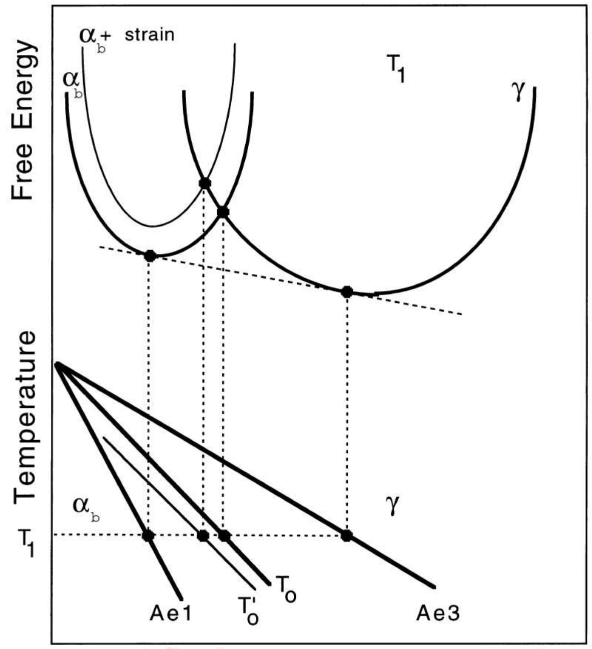

Figure 1.2: Schematic illustration of the T_0 and $T_0^{'}$ curves [1]. T_1 is the temperature corresponding to the free energy curves.

where $C_{T_0'}$ is the austenite carbon content given by the $T_0^{'}$ boundary, $\bar{x}$ is the alloy average carbon concentration and x_{α_b} is the carbon concentration of the bainitic ferrite. The thermodynamic restriction imposed by the $T_0^{'}$ curve on the extent of bainite transformation can result in the formation of pools of retained austenite with a coarse, blocky morphology. However, austenite also appears in the form of thin films trapped in between bainitic ferrite plates, as shown in figure 1.3.

1.2.1 Effect of Alloying Elements on the T_0 Curve

The effect of substitutional solutes on the T_0 temperature is given by [16]:

$$\Delta T_0 = \frac{x(b_{NM}\Delta T_{NM} + b_M \Delta T_M)}{b_{NM} + b_M} \tag{1.2}$$

where x is a unit concentration of the substitutional solute, ΔT_{NM} and

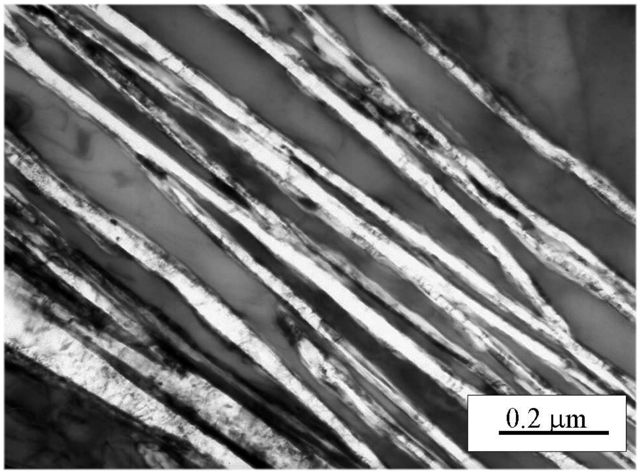

Figure 1.3: Bright field TEM (transmission electron microscopy) micrograph exhibiting the fineness of retained austenite films (dark) in a bainitic microstructure [15].

ΔT_M are the non-magnetic and magnetic temperature changes due to a unit change in the concentration of the substitutional solute. Values of a and b are listed in table 1.1. The combined effects of multiple substitutional elements are approximated by assuming additivity [16]:

$$\Delta T_0 = \frac{\Sigma_i x_i (b_{NM}\Delta T_{NM_i} + b_M \Delta T_{M_i})}{b_{NM} + b_M} \tag{1.3}$$

By allowing for 400 J mol^{-1} stored energy in bainitic ferrite, the $T_0^{'}$ curve for a plain carbon steel is given by [16]:

$$T_0^{'}(\mathrm{K}) \simeq 970 - 80x_c \tag{1.4}$$

so, for a given alloy it is modified to:

$$T_0^{'}(\mathrm{K}) \simeq 970 - 80x_c - \Delta T_0 \tag{1.5}$$

where x_c is the atomic fraction of carbon.

Function	a	b	Temperature Range
$\Delta G_{NM}^{\gamma\alpha}$	-6660	7	900>T>300 K
$\Delta G_{M}^{\gamma\alpha}$	650	-1	900>T>620 K
$\Delta G_{M}^{\gamma\alpha}$	0	0	T<620 K

Table 1.1: Approximate values for non-magnetic (ΔG_{NM}) and magnetic (ΔG_M) free energy components of the transformation $\gamma \rightarrow \alpha$ in pure iron. The formula $\Delta G = a + bT$ J mol^{-1} should be used for estimating the free energy changes [17].

Solute	ΔT_M (K) per at.%	ΔT_{NM} (K) per at.%
Si	-3	0
Mn	-37.5	-39.5
Ni	-6	-18
Mo	-26	-17
Cr	-19	-18
V	-44	-32
Co	19.5	16
Al	8	15
Cu	4.5	-11.5

Table 1.2: Values of ΔT_M and ΔT_{NM} for some substitutional elements [18].

It is apparent from table 1.2 that Mn has the largest effect in depressing the T_0 temperature. On the contrary, Co and Al increase T_0, thereby facilitating the formation of a greater volume fraction of bainitic ferrite.

On the other hand, Quidort and Bouaziz proposed that the incomplete bainite reaction or the 'transformation stasis' is a result of the reduction in transformation driving force due to plastic straining of the austenite matrix [19]. The authors pointed out to the difficulties associated with accurately determining carbon content in retained austenite in order to validate the T_0 concept. Furthermore, they argued for possible inaccuracies which might be associated with the calculation of T_0 compositions being dependent on extrapolated thermodynamic data from higher temperatures.

The above theory has been discussed by Caballero and Bhadeshia where it was argued that the plastic work calculated in [19] should be divided by unit quantity of bainite instead of the fraction of remaining austenite [20].

1.3 Transformations Beyond T_0 Concentration

Hillert argued that even if the diffusionless growth of bainite has stopped, further transformation into Widmanstätten ferrite should still be possible [4].

Tsuzaki *et al.* observed the formation of large carbide plates in the carbon-rich austenite, the austenite later decomposing into ferrite [21], in a steel of composition Fe-2Si-0.6C (wt%). It is obvious that carbide precipitation was the main reason for further austenite decomposition despite that the alloy had been alloyed with 2 wt% Si.

In the work of Tsuzaki *et al.*, the bainite was initially carbide-free, consistent with the alloy high-Si concentration. However, the ferrite formed at later stages of bainite transformation possessed a variant which was different from that of the early formed bainitic ferrite.

Chang observed the formation of lenticular bainite first, followed by pearlite along the grain boundary after heat treating a steel of composition Fe-0.46C-2.1Si-2.15Mn (wt%) at 510°C, demonstrating that the formation of the diffusion-controlled pearlite transformation lags behind bainite [22].

1.4 Effect of Si, Al and P on Bainite Transformation

Silicon, when present in an amount greater than 1 wt% contributes significantly to the enrichment of carbon in austenite by inhibiting carbide precipitation. The TRIP phenomenon, caused by strain-induced martensite transformation of austenite is said to be responsible for improved elongation. In TRIP-aided steels, Si also contributes to the solid-solution strengthening of ferrite. Silicon has also been reported to lower the lower-bainite start temperature [22].

Silicon does harm the surface quality of steels and limits their use in galvanised products. Attempts have therefore been made to substitute silicon with Al or P [23].

Aluminium is promising as a carbide-suppressing element, but does not contribute to the strengthening of ferrite. Results obtained in TRIP-aided steels (table 1.3) containing various levels of Al and Si are shown in figures 1.4 and 1.5. As shown in figure 1.4, for the same holding time, the amount of untransformed retained austenite was less in the Al-steel compared with Si-steel, with Al-Si steel exhibiting the lowest amount of retained austenite.

Figure 1.5 shows that, for all steels investigated, carbon content of austenite was comparable.

It is therefore concluded that full or partial substitution of Si with Al does not decelerate bainite transformation nor it affects the carbon content of retained austenite.

wt%	C	Mn	Si	Al	P	S	N
Al1	0.11	1.55	0.059	1.5	0.012	0.007	0.017
Si1	0.11	1.53	1.5	0.043	0.008	0.006	0.0035
Al-Si	0.115	1.51	0.49	0.38	0.003	0.009	0.03

Table 1.3: Chemical composition of steels investigated by Jacques *et al.* [24].

Mertens *et al.* demonstrated the pronounced effect of Al in accelerating bainite transformation kinetics in comparison with Si [25], consistent with

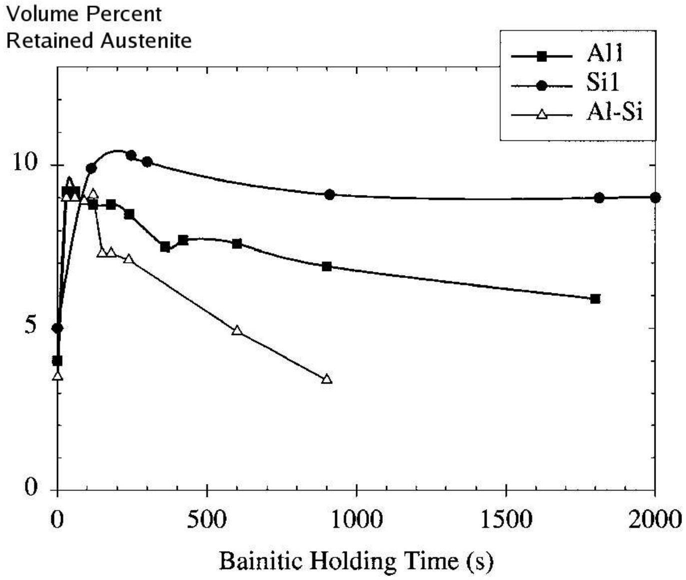

Figure 1.4: Volume fraction of retained austenite as a function of bainite holding time at 375°C [24]. The steels have the composition shown in table 1.3.

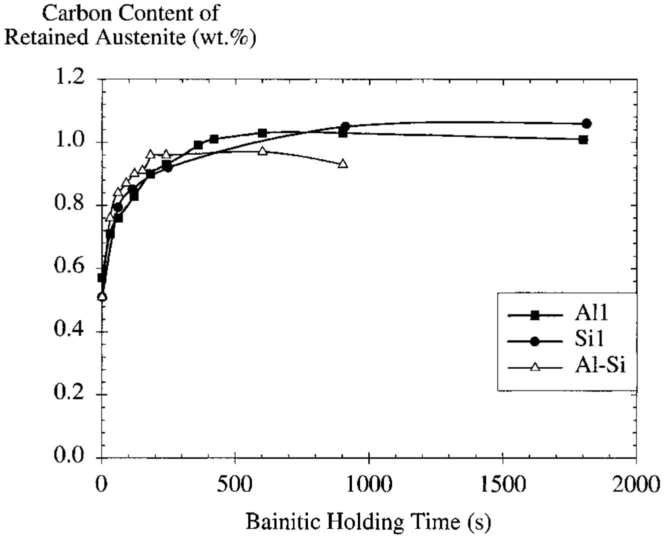

Figure 1.5: Carbon content of retained austenite as a function of bainite holding time at 375°C [24]. Compositions are shown in table 1.3.

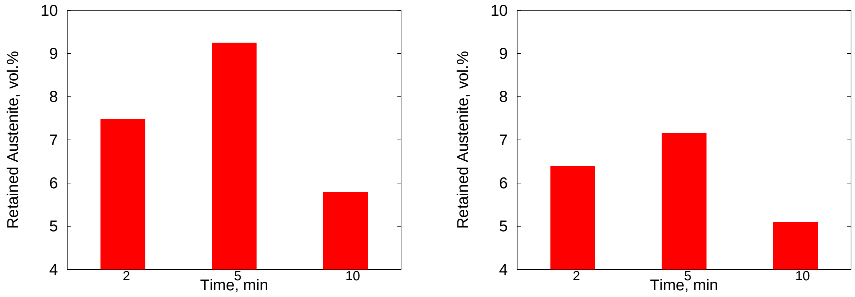

(a) Fe-0.22C-1.55Si-1.55Mn-0.035Nb-0.028Al (b) Fe-0.19C-1.5Si-1.54Mn-0.024Al

Figure 1.6: Variation of retained austenite content with holding time at 400°C [34]. Compositions are in wt%. Both steels also contain 20–40 N (ppm).

the results in table 1.2.

Phosphorus contributes to the solid-solution strengthening of ferrite [26, 27]. Pichler *et al.* have shown that the addition of 0.001 wt% P allowed the reduction of Si content with a significant improvement in strength [28]. However, as discussed by Wang and Van der Zwaag, it is uncertain how efficient phosphorus is in preventing carbide precipitation [29]. Therefore, it is difficult to determine the amount of phosphorus required. Furthermore, the possible precipitation of phosphide (Fe_3P) has negative effect on the steel properties [30]. This necessitates limiting the P concentration.

Mo is also effective as a ferrite solid-solution strengthening element which inhibits carbide precipitation [31, 32].

1.5 Isothermal Transformation to Bainite

The temperature and transformation time determine the phase fractions and the carbon content of the retained austenite, which in turn determine the mechanical properties [27, 33–42].

The austenite volume fraction peaks with time as shown in figure 1.6 [34]. Prolonged holding caused carbide precipitation thereby destabilising the austenite.

Figure 1.7 shows the effect of bainite transformation temperature on the

extent of transformation. For the same holding time, the fraction of bainite transformed was greater when transforming at higher temperatures.
Figure 1.7(a) shows that silicon enhances the retention of the residual austenite.

1.6 Stability of the Retained Austenite

The blocky morphology of austenite is detrimental to toughness when the austenite transforms into high-carbon, untempered martensite at an early stage of deformation. On the other hand, austenite films which have a higher carbon content are much more stable and remain untransformed to later stages of deformation [44–48].

The ratio of films to blocky austenite should exceed about 0.9 for optimum properties [49]:

$$(V_{\gamma-f}/V_{\gamma-B}) = V_{\alpha_b}/(6 - 7.7V_{\alpha_b}) > 0.9 \tag{1.6}$$

where $V_{\gamma-f}$ and $V_{\gamma-B}$ are the volume fractions of film and blocky morphologies respectively and V_{α_b} is that of bainite.

Following Zackay [50], the potential of enhancing ductility through the TRIP effect was popularised in automobile applications with the aim of improving the crash-worthiness of cold-formable automobile parts.

The TRIP effect was originally observed in fully austenitic steels with sufficient Ni and Mn to maintain the M_S temperature below room temperature. However, such alloying elements are expensive.

In 1987, Matsumura *et al.* reported the potential of bainite in TRIP-aided carbide-free steels, where as a result of the transformation, austenite carbon-enrichment takes place [51, 52]. In this way expensive elements are no longer necessary to retain γ [53–55].

Unlike the usual practice of subjecting a high-Si steel to isothermal bainite transformation directly by quenching from the γ-phase field, it is also possible to intercritically anneal and then isothermally transform to α_b, with

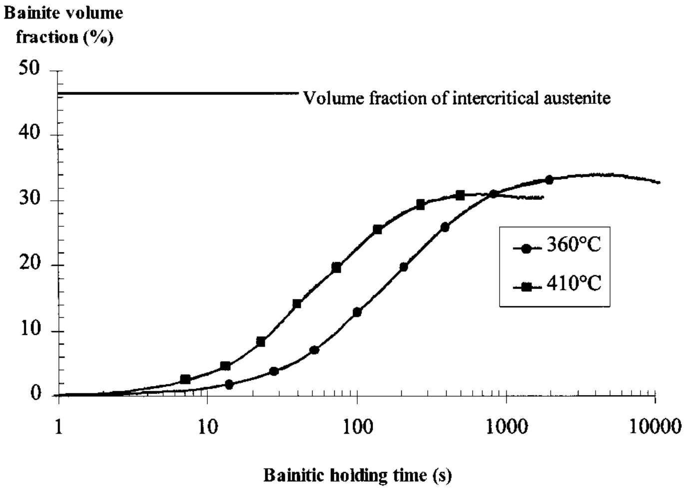

(a) HSi

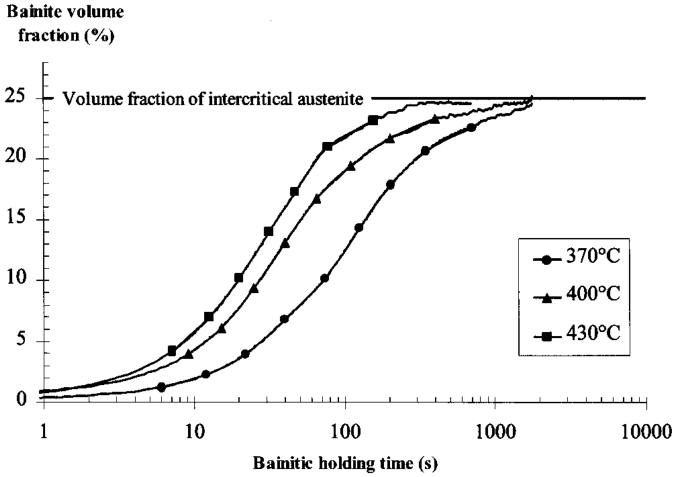

(b) LSi

Figure 1.7: Volume fraction of bainite as a function of transformation time for (a) Fe-0.29C-1.4Mn-1.5Si; (b) Fe-0.16C-1.3Mn-0.38Si (wt%) [43].

more refined austenite regions.

The strain-induced transformation of retained austenite has been modelled using the Austin and Rickett-type equation formulated by Burke [56]:

$$-\frac{dV_\gamma}{d\varepsilon} = k_P V_\gamma^2 \varepsilon^{P-1} \tag{1.7}$$

where V_γ is the austenite volume fraction, ε is the plastic strain, k_P is an empirical constant and P is the strain exponent which is related to the autocatalytic effect.

With the assumption that k_P and P are independent of V_γ, and by considering $V_\gamma = V_\gamma^0$ at $\varepsilon = 0$, equation 1.7 can be integrated as follows [52]:

$$\frac{1}{V_\gamma} - \frac{1}{V_\gamma^0} = \frac{k_P}{P}\varepsilon^P \quad or \quad V_\gamma = \frac{V_\gamma^0}{1 + (k_P/P)V_\gamma^0 \varepsilon^P} \tag{1.8}$$

As shown in figure 1.8, the log-log plot of $(1/V_\gamma - 1/V_\gamma^0)$ *vs* ε of the experimental steel yielded a slope $P = 1$ comparable to that of dual-phase steel. However, a value of $P = 3$ was obtained in conventional TRIP metastable austenitic stainless steels. Thus, the expression for the experimental steel was formulated as [52]:

$$-\frac{dV_\gamma}{d\varepsilon} = kV_\gamma^2 \tag{1.9}$$

for the special case where $P = 1$. k is a constant. Equation 1.9 indicates a negligible autocatalytic effect. The suppression of autocatalysis was attributed to the presence of phases such as ferrite, in the microstructure.

For a given steel, the volume fraction, chemical stability and morphology of the retained austenite play a crucial role in the TRIP effect. A higher volume fraction of austenite is expected to contain a lower carbon concentration, whereas a much lower austenite content may be so rich in carbon that it does not transform at all [37]. While a large austenite grain will transform at an earlier stage of straining, austenite grains of sub-micron sizes may remain untransformed up to necking [36, 57].

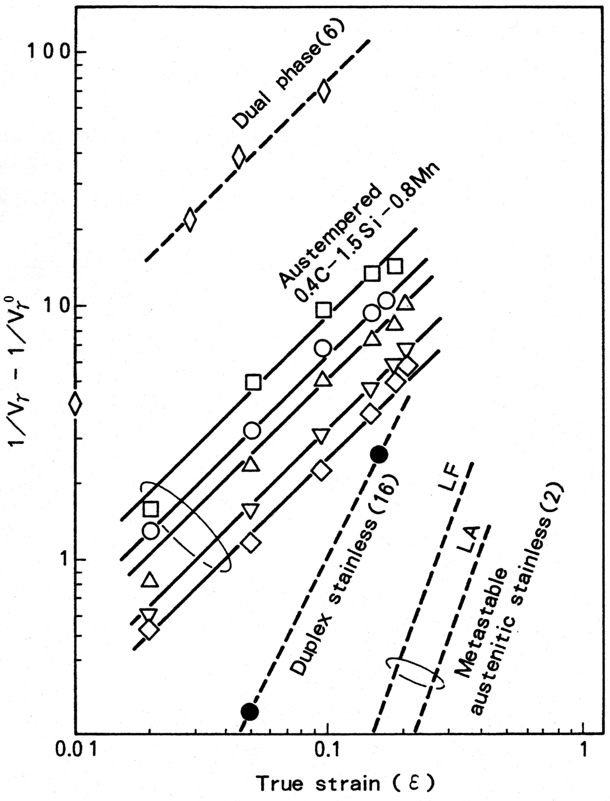

Figure 1.8: Austenite transformation *vs* strain of the experimental TRIP-aided steel [52]. Other steel types are also shown for comparison.

As far as TRIP-aided multiphase steels are concerned, the characteristics of austenite in the final microstructure are inherited during intercritical annealing when fine granules of austenite appear along the boundaries of ferrite grains. During subsequent quenching and holding at the bainite transformation temperature, the reaction proceeds by the growth of bainitic ferrite plates resulting in further carbon-enrichment and modification of the morphology of the residual austenite [58].

The above discussion suggests the dependence of bainitic transformation in such steels on the intercritical and isothermal transformation conditions, both of which are influenced by the steel composition.

The carbon content of retained austenite C_γ can be estimated as a function of the overall carbon concentration [59]:

$$C_\gamma = \bar{x} + V_{\alpha_b}(\bar{x} - x_{\alpha_b})/(1 - V_{\alpha_b}) \tag{1.10}$$

Bhadeshia and Edmonds identified an austenite stability parameter as the ratio of retained austenite and athermal martensite formed during final quenching to room temperature [49]. Figure 1.9 shows the variation of the stability parameter as a function of austenite carbon content for 0.43C-2.0Si (wt%) steel transformed at 270°C and 363°C.

While the microstructure of the steel transformed at 363°C comprised bainitic ferrite, retained austenite and some martensite, the steel transformed at 270°C additionally contained some carbides within the bainitic ferrite.

Figure 1.9 demonstrates greater austenite stability in the bainitic steels due to its size being smaller than that achieved in the plain carbon-steels.

Tsuzaki *et al.* reported a maximum amount of carbon-enrichment in austenite of 1.61 wt% in the case of a 0.6C–2Si (wt%) steel transformed at 450°C for 50 s. The measured austenite carbon content was lower than the paraequilibrium value of 3.59 wt% [21], presumably because of the incomplete reaction phenomenon. The carbon concentration in the bainitic ferrite was found to be 0.19 wt% at the lowest, indicating a significant degree of supersaturation.

In early work on TRIP-aided steels, the enhancement in elongation was ascribed to the martensitic transformation of retained austenite under ten-

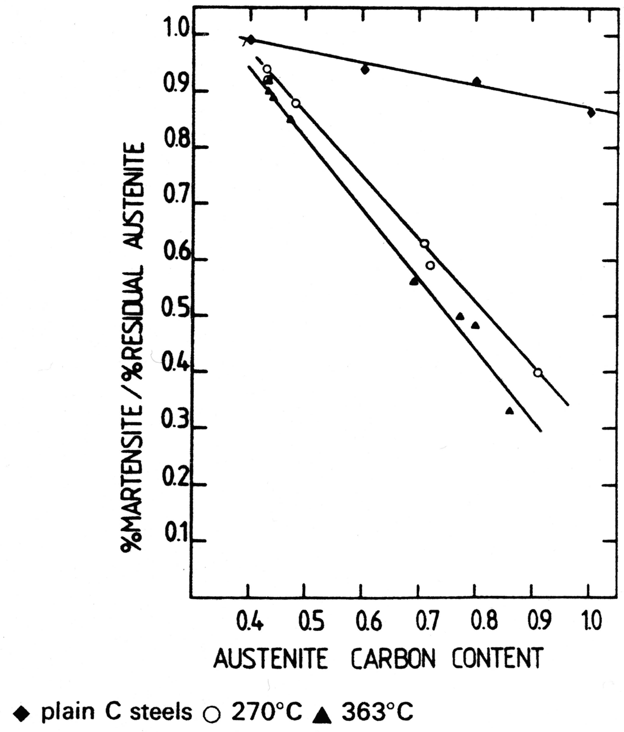

Figure 1.9: The austenite stability parameter as a function of carbon content, in wt% [49].

sion. Recent work has emphasised the contribution of microconstituents other than austenite in the overall deformation behaviour [60–63].

According to Jacques *et al.*, an enhanced strength-ductility balance may be attributed to dislocation density strengthening in allotriomorphic ferrite [61]. On the other hand, Perlade *et al.* assumed that the improvement is due to dislocation density strengthening in the austenite phase due to martensitic transformation [64].

It has been reported that ductility is not only influenced by retained austenite but also by the fraction of ferrite [63].

Bhadeshia has demonstrated that only about 2% of the large elongation observed (15–30%) may be accounted for by transformation plasticity *per se* [65].

During deformation, strain at first concentrates in the softest phase [66].

Harder phases deform plastically only after the soft constituents have strain-hardened. The soft phases 'cushion' against the strain due to martensite, thereby inhibiting bursts of transformation and reducing the autocatalytic effect. The presence of hard phases reduces the mean stress in the austenite, therefore delaying strain-induced martensitic transformation, rendering the transformation process more progressive, which is beneficial to ductility.

1.7 Bainite-containing Steels

The attractive mechanical performance of microstructures which contain carbide-free bainite is now well-established [47, 49, 51, 52, 57, 67–76].

1.7.1 Fully Bainitic Steels

The ductility of fully bainitic steels (containing carbides) is generally improved by reducing the average carbon content whilst strength can be maintained using substitutional solutes [77]. Fully bainitic low-carbon steels exhibit better elongation than quenched and tempered-martensite steels of equivalent strength, but the reverse is true at high-carbon concentrations [77].

Lower bainite usually exhibits higher toughness than upper bainite presumably due to the finer carbides [1]. The achievable strength and toughness in bainitic steels has primarily been attributed to the fineness of the microstructure [78].

Cementite is known to be brittle [1]. The coarsest cementite particle governs the toughness rather than the average size [79]. In lower bainite, when compared with upper-bainite structures, the cracks generated from the finer carbide particles are smaller and hence more difficult to propagate, leading to an improved toughness [1].

The refinement of the bainite packet size also enhances the toughness. As shown in figure 1.10, the ductile-brittle transition temperature of fully bainitic steels has been found to decrease with finer prior austenite grains.

In spite of the appealing mechanical performance, bainitic steels have limitations when compared with pearlitic and tempered-martensite steels.

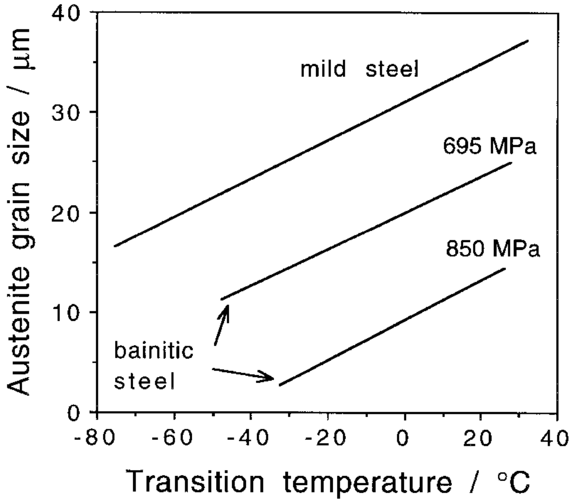

Figure 1.10: Effect of austenite grain refinement on the impact transition temperature [80].

A conventional bainitic microstructure is superior to pearlite of comparable composition only in the low-hardness regime [81]. Moreover, the coarse carbide particles in high-strength bainitic steels appear to be the most detrimental constituent [82–84].

Following the completion of the bainite transformation, and during cooling to room temperature, the possible formation of untempered athermal martensite due to the decomposition of the unstable residual austenite further worsens the mechanical performance. Such limitations prompted the search for carbide-free bainitic steels with austenite which is chemically stable exhibiting M_S well below room temperature.

Carbide-free bainitic steels comprise fine plates of bainitic ferrite separated by carbon-enriched austenite films with adequate resistance to carbide precipitation. Suppression of carbide precipitation during bainite transformation has been achieved, for example, through the addition of 1.5 wt% silicon which has very low solubility in cementite and greatly retards its growth [85–87].

Very Fine Bainite

During the last two decades, ultrafine- (<500 nm) and nano-grained (<100 nm) polycrystalline materials with exceptional mechanical properties have been discovered [88, 89]. However, due to production and ductility shortfalls, their technological viability is limited.

While utilisation of conventional powder metallurgy techniques suffers from limitations with respect to the expected increase in grains surface chemical reactivity and therefore limited thermal stability of very fine powders, contamination and possible residual porosity [90], severe plastic deformation techniques have yet to mature with respect to the shape and geometry of the components produced.

Caballero and Bhadeshia have developed a high-carbon high-silicon carbide-free bainite with very thin austenite films forming an intimate composite, with a controlling scale of 20–30 nm (figure 1.3) [20, 91].

The microstructure exhibits an excellent combination of strength and ductility as shall be demonstrated in the present work. The strength comes from the fine scale of the structure whereas the ductility is associated with the texture of γ and α_b.

The production of the steel is straightforward; involves an affordable conventional heat-treatment process. This is believed to be a significant advantage over other production techniques usually adopted for the synthesis of nanostructured materials. The optimisation of alloy composition was needed to comply with conventional heat-treatment procedures whilst keeping the desired microstructure.

There is a wide variation in microstructural scale as a function of the bainite transformation temperature (figure 1.11).

On the other hand, carbon content in retained austenite is generally found to decrease with an increase in the transformation temperature [94, 95].

The relationship shown in figure 1.12 [92] indicates an increase in the yield strength with the decrease in transformation temperature. This corresponds to the decrease in bainite plate thickness and the appearance of twins in austenite when the latter is transformed below 380°C. By contrast,

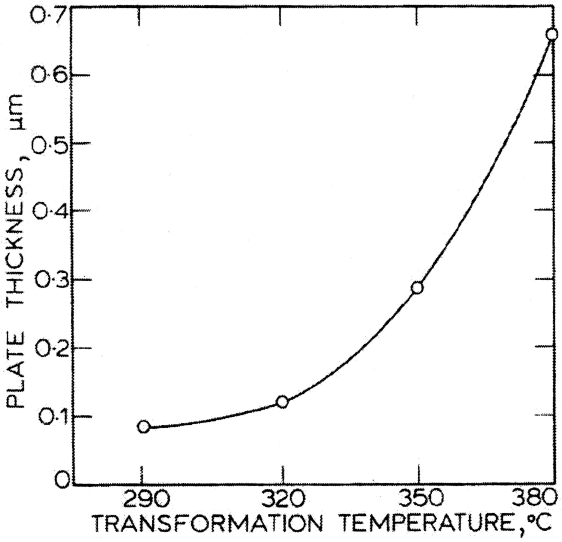

(a) Steels containing 0.65–0.99 C and 2–2.78 Si (wt%), with and without Cr [92]

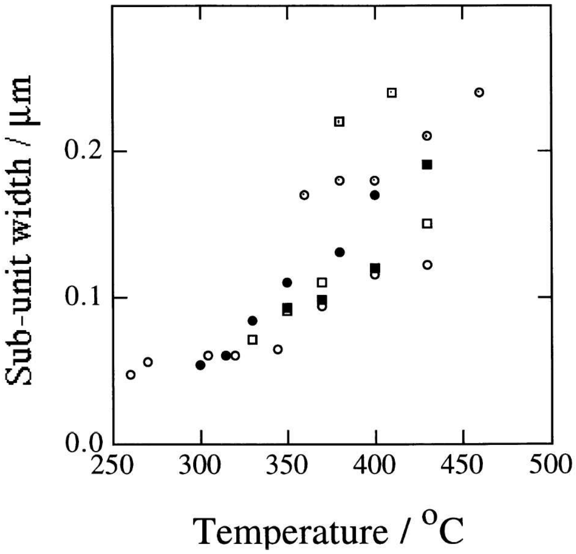

(b) Different steel compositions [93]

Figure 1.11: Bainite plate width *vs* transformation temperature.

an increase in the austenite volume fraction at a given transformation temperature was held responsible for the decrease in the yield strength.

Figure 1.12 also shows that the ultimate tensile strength is generally less sensitive to retained austenite content except at the higher transformation

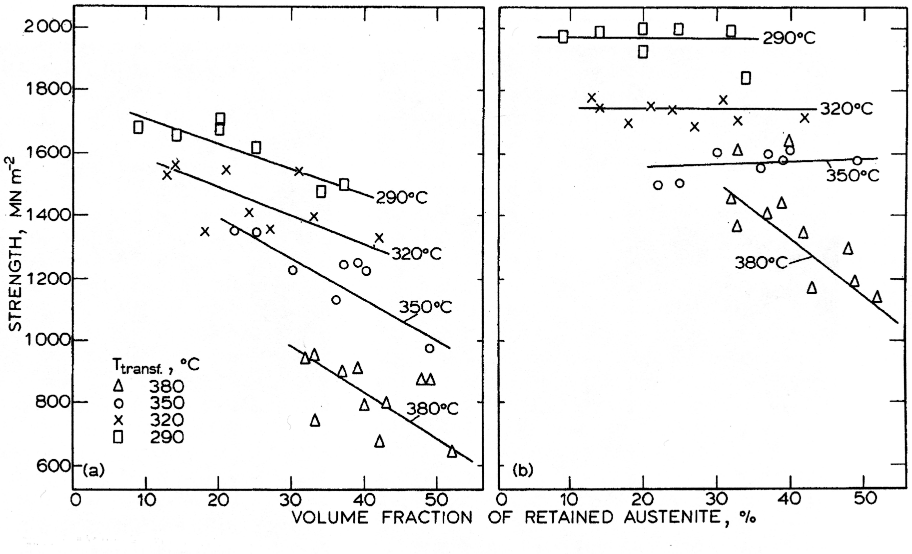

Figure 1.12: (a) Effect of volume fraction of austenite and corresponding transformation temperature on yield strength; (b) effect on tensile strength [92].

temperature of 380°C. The latter may be attributed to the fact that V_γ exceeds 0.3, leading to much blocky austenite.

Figure 1.13 reveals the manner in which the elongation is influenced by V_γ, reaching a maximum except for steels transformed at lower temperatures. The maximum has been associated with the homogeneous distribution of thin films of austenite, beyond which the appearance of austenite pools at larger fractions adversely affects elongation. The stress-strain curves associated with austenite content which was below, at and above that of the optimum are shown in figure 1.14.

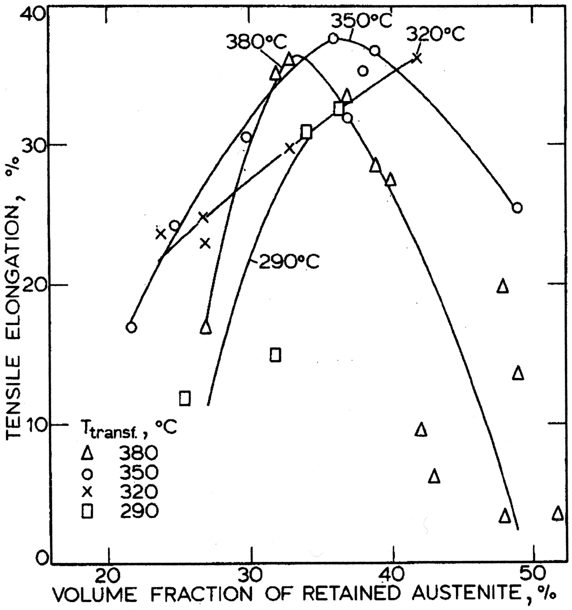

Figure 1.13: Volume fraction of retained austenite *vs* tensile elongation [92].

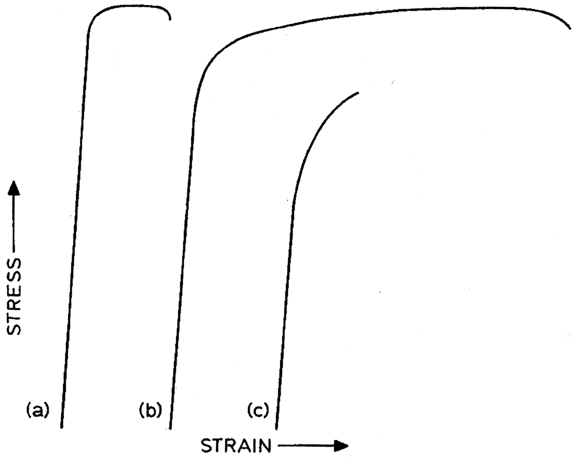

Figure 1.14: Stress-strain curves of steel with (a) low austenite volume fraction; (b) optimum volume fraction and (c) high volume fraction [92].

1.8 Summary

Bainitic ferrite phase in steel structures contribute significantly not only to mechanical properties but more importantly to the ability to design specific steel microstructures for various applications. In this regard, the following remarks may be summarised:

1. The suppression of carbide precipitation during bainite transformation by alloying using minimum levels of silicon or other carbide-suppressing elements such as Al and P is crucial.
2. The importance of achieving an optimum content of *stable* retained austenite has been demonstrated in the published literature.
3. The achievement of very fine bainite can lead to exceptional mechanical properties not normally available in low-alloy *affordable* steels.
4. The observed continuous work-hardening exhibited in bainitic steels containing retained austenite due to the progressive martensitic transformation is held responsible for this good ductility.

Chapter 2

Steel Design & Production

2.1 Introduction

The objective of the work described in this chapter is to provide details about the design, optimisation and production of the steel investigated.

2.2 Steel Design

As previously mentioned in Chapter 1, several attempts have been made to assess the potential of fully bainitic steels. In particular, Caballero and Bhadeshia's work was directed towards the design of a steel with a bainitic matrix, for defence applications which necessitated a Charpy energy of about 40 J at -40°C, a fracture toughness (K_{IC}) of 125 MPa $m^{1/2}$, yield strength of 1000 MPa, ultimate tensile strength of 1100 MPa and a minimum elongation of 12% [96–98].

The design of the steel was based on shifting the $T_0^{'}$ curve to a greater austenite carbon content at any transformation temperature by adjusting the substitutional solute content, thereby:

- allowing for more carbon-enrichment in austenite as bainite forms, in order to increase its stability;
- obtaining a higher volume fraction of bainitic ferrite;
- accelerating the rate of transformation.

A higher carbon content in austenite increases its chemical and mechanical stability against transformation into martensite [99–101]. As will be seen later in this thesis, austenite is most beneficial when it transforms at the late stages of deformation. Increasing the volume fraction of bainite transformed has the effect of reducing the undesirable, mechanically unstable, blocky morphology of austenite [44] and at the same time increases the strength of the steel. In this context, increasing the amount of bainite transformed by reducing the transformation temperature may not enhance austenite carbon-enrichment if a greater amount of carbon becomes trapped in the bainitic ferrite [102].

2.2.1 Optimisation of Steel Composition

Carbon

Carbon is very effective in suppressing the bainite-start temperature with the aim of refining the microstructural scale [103].

Silicon

Silicon suppresses cementite precipitation, particularly from austenite during bainite growth. The carbon then partitions into the austenite, thereby stabilising it to ambient temperature.

The designed alloy contained about 1.5 wt% Si, and in some heats Al (1–1.3 wt%) was also added. Silicon has negligible effect on the T_0 curve.

Manganese

Manganese greatly enhances austenite stability [104], but it shifts the T_0 curve to lower carbon concentrations [18]. Therefore, its concentration was limited to about 2 wt% to ensure hardenability.

Mn is also a ferrite strengthening element [105].

Cobalt and Aluminium

The low-temperature bainite transformation can be very slow [106]. Cobalt and aluminium both increase the free energy change for the $\gamma \rightarrow \alpha_b$ transformation (figure 2.1) and hence can be used to accelerate the rate of reaction [107].

Aluminium also retards cementite precipitation. However, it does not contribute as much to ferrite solid solution strengthening [23]. In the present work, Co and Al concentrations were varied as listed in table 2.1.

Alloy	C	Si	Mn	Mo	Cr	Co	Al	P	S	Fe
Sp9	0.83	1.57	1.98	0.24	1.02	1.54	–	–	–	Bal.
Sp9c	0.8	1.59	2.01	0.24	1	1.51	–	0.002	0.002	Bal.
Sp10c	0.79	1.56	1.98	0.24	1.01	1.51	1.01	0.002	0.002	Bal.
Sp11c	0.78	1.6	2.02	0.24	1.01	3.87	1.37	0.002	0.002	Bal.

Table 2.1: Chemical compositions of alloys investigated in the present work (wt%).

The time required for the initiation of bainite transformation was calculated as shown in figure 2.2(a). For comparison, the kinetics representing a *slow* steel are shown in figure 2.2(b). The start of the bainite transformation in steel Fe-2Si-3Mn-C with 1 wt% carbon at 140°C would require a year. On the other hand, the time required can be greatly reduced to only 4.6 months in steel Sp9c with same carbon concentration and transformation temperature. Figure 2.2(c) demonstrates the profound effect of carbon on both the B_S and M_S temperatures.

On the basis of the preliminary kinetic analysis, a maximum practical alloy carbon concentration would be around 0.8 wt%, which was adopted. The acceleration due to Co and Al is apparent in the data listed in table 2.2.

Alloy	B_S (°C)	M_S (°C)	Time (s)
Sp9c	235	80	5120
Sp10c	280	132	3860
Sp11c	415	220	2040

Table 2.2: Kinetic parameters calculated using MUCG73. The time is the delay in seconds before bainite transformation starts (calculated at 234°C for all alloys).

Given that the measured bulk carbon concentration per alloy is similar, the addition of Co and or Al resulted in an increase in the B_S and M_S

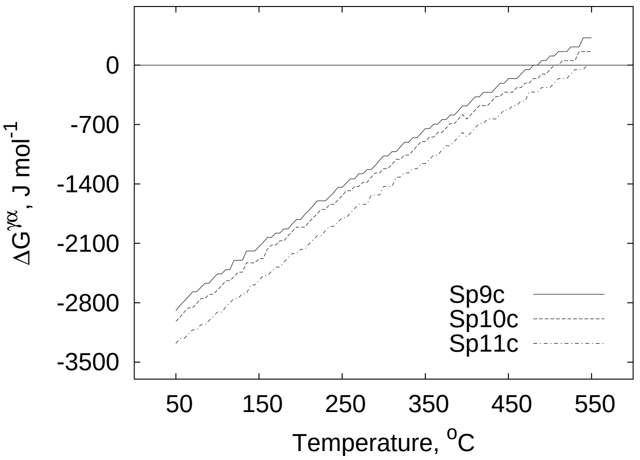

Figure 2.1: The driving force ($\Delta G^{\gamma\alpha}$) available for bainite transformation *vs* temperature for some of the alloys listed in table 2.1. Thermodynamic calculations were carried out using MTDATA.

temperatures and a significant decrease in the time before bainite starts to form. Furthermore, at a given transformation temperature, the increased driving force has the effect of shifting the T_0' curve to higher carbon concentrations [18] (figure 2.3).

Accordingly, it is speculated that the austenite retained in Sp11c would be the richest in carbon amongst the three alloys.

The martensite-start temperature of Sp11c must be less than that calculated (table 2.2) [109]. Even at as low transformation temperatures as 200°C, a carbide-free bainitic microstructure was obtained.

Molybdenum

Molybdenum was added to inhibit austenite grain-boundary embrittlement due to the presence of impurities such as phosphorus [96]. Mo also increases hardenability and slightly enhances strength [82]. Mo is a ferrite stabilising element, but nevertheless suppresses the kinetics of ferrite and pearlite formation which is useful if a bainite microstructure is desired.

Mo also reduces the B_S temperature [110]. Its content was limited to about 0.24 wt% to avoid shifting the T_0 curve to lower carbon concentra-

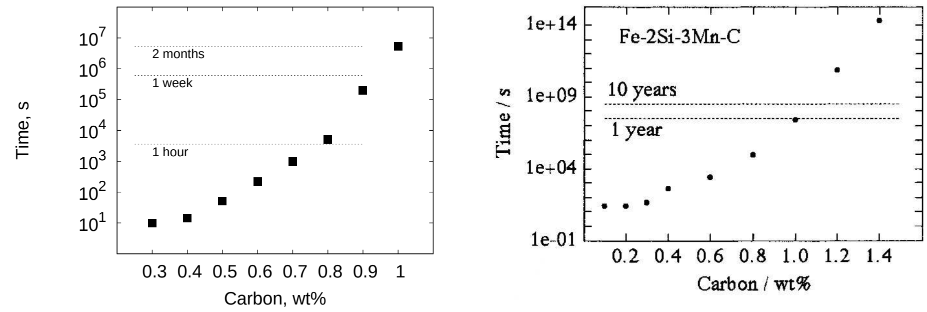

(a) Time required for bainite transformation to start calculated just one degree Celsius below the bainite-start temperature

(b) The calculated time necessary for the initiation of bainite transformation *vs* carbon concentration [106]

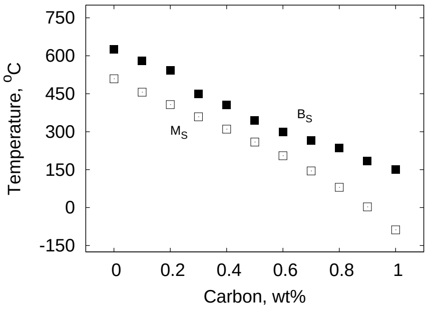

(c) Change in bainite and martensite-start temperatures as the carbon concentration varied. In this case carbon has reduced both B_S and M_S temperatures

Figure 2.2: (a) and (c): Kinetic parameters of steel Sp9c *vs* carbon concentration, calculated using MUCG73 [108]. Note that figure 2.2(a) represents transformation kinetics of the *slowest* alloy of the system studied here, *i.e.* steel Sp9c. (b) Kinetic parameters of a *slow* bainitic steel.

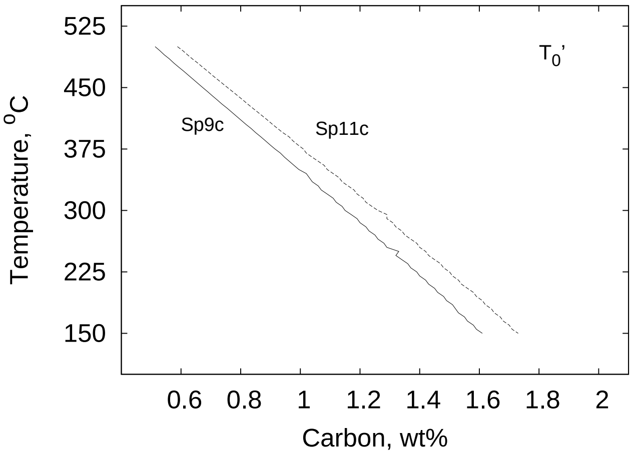

Figure 2.3: T_0' curves of Sp9c and Sp11c. Calculations were carried out using MTDATA. An energy of 400 J mol^{-1} was assumed to be stored in bainite [3].

tions [18].

Chromium

Chromium significantly increases the hardenability and depresses the B_S temperature and shifts the T_0 curve to lower carbon concentrations [18, 23].

2.3 Experimental Procedures

Steel ingots of the composition shown in table 2.1 were provided by Corus UK, hot-rolled down to slabs of 40 mm thickness. Samples were cut and then homogenised at 1200 °C for 48 h in a vacuum furnace. Then they were left in the furnace to cool down to room temperature over a period of 24 h resulting in a fully pearlitic microstructure. The slow cooling was necessary to avoid athermal martensite formation which may introduce cracks, thus permanently affecting the integrity of the sample. Figure 2.4 illustrates cracks generated in a steel structure by quenching in water from the γ-phase field.

Tensile testing samples were then machined from the relatively soft homogenised lumps which are pearlitic, since the bainitic microstructure is too

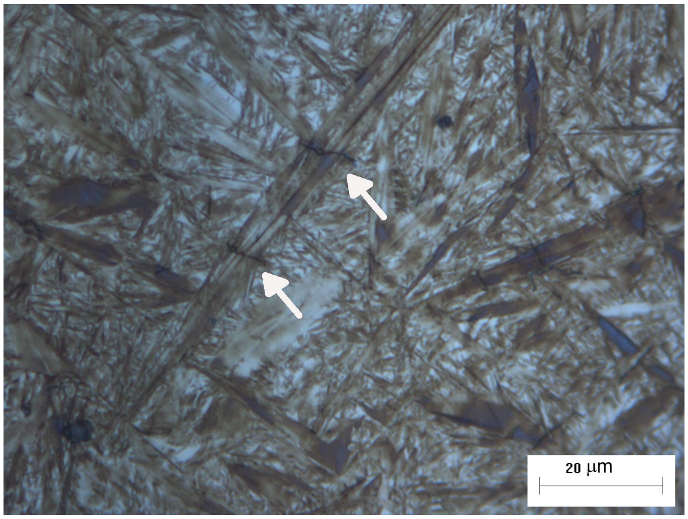

Figure 2.4: Sp10c microstructure featuring cracks generated in an athermal martensite plate (arrowed). The M_S temperature was calculated using MUCG73 and found to be 136°C.

hard (about 600 HV) to easily machine.

2.3.1 Heat-treatment

It was important to ensure complete dissolution of cementite present in the as-homogenised pearlitic structure during subsequent austenitisation. Figure 2.5 shows thermodynamic calculations which were used to set the austenitisation parameters listed in table 2.3.

To avoid oxidation, austenitisation was carried out in a tube-furnace with a continuous flow of commercial purity argon. Prior to austenitisation, during sample loading at moderate temperatures, the furnace was evacuated and repeatedly flushed with argon.

After holding at the γ-phase field for sufficient time to ensure a fully austenitic state but not so long as to give grain coarsening, the samples were transformed in another furnace which was kept at the chosen bainite transformation temperature (table 2.4). Transformation times were selected from previous work to ensure cessation of reaction [111].

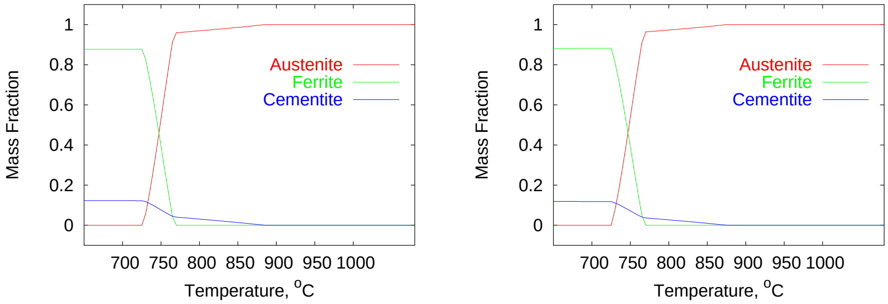

(a) Steel Sp9 (b) Steel Sp9c

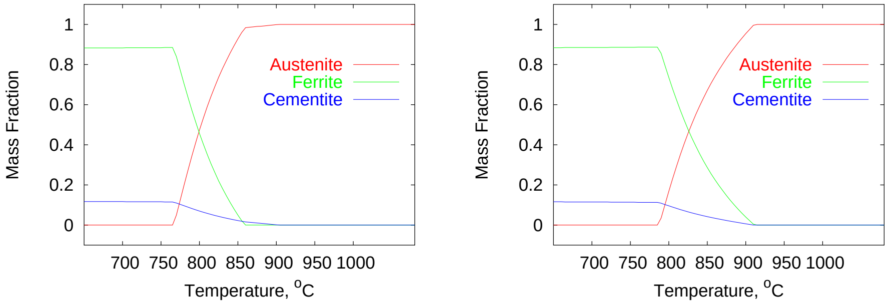

(c) Steel Sp10c (d) Steel Sp11c

Figure 2.5: Evolution of equilibrium phase fractions. During calculations using MTDATA, only austenite, ferrite and cementite were allowed to exist.

Steel	Cementite dissolved at (°C)	Austenitisation temperature (°C)	Duration (min)
Sp9	890	920	30
Sp9c	830	900	30
Sp10c	905	920	30
Sp11c	915	1000	15

Table 2.3: Austenitisation parameters.

Transformation temperature (°C)	Duration
200	3 days
250	15–16 h
300	6 h

Table 2.4: Bainite transformation parameters.

2.4 Summary

In this chapter, the basic concepts behind the design of the novel bainitic carbide-free steels, and their heat-treatments, were discussed. The following points may be summarised:

1. It seems possible to make these nanostructured steels using conventional heat-treatments combined with alloy design and without the addition of expensive alloying elements.
2. The microstructure can be generated using reasonable transformation times.

Chapter 3

X-ray Diffraction Analysis

3.1 Introduction

The objective of the present chapter is to provide an understanding of microstructural evolution and phase interactions during the uniaxial straining in tension of bainitic steels characterised using X-ray diffractometry. Some observations regarding microstructural behaviour due to continuous heating to high temperature and tempering are also reported.

3.2 Experimental Procedures

A characterisation programme using X-ray diffraction has been carried out to investigate microstructural evolution of bainitic steels as a function of plastic strain. Tensile test samples were heat-treated as mentioned in tables 2.3 and 2.4. As a result, the microstructure consisted of only austenite and bainitic ferrite.

After heat-treatment, the 5 mm diameter samples were subjected to uniaxial tensile load and strained as indicated in table 3.1. All tests were carried out at room temperature using an INSTRON 8500 fitted with 100 kN load cell, with a cross-head speed of 0.01 mm min^{-1}. Elongation was recorded *via* an electronic data acquisition system coupled with an extensometer with a gauge length of 10 mm.

Upon straining, the metastable austenite transforms into martensite which inherits the chemical composition of the austenite. Martensite has only a slightly body-centred tetragonal crystal structure which makes it difficult to distinguish it from ferritic phases using X-ray diffraction. Peak separation becomes more difficult when the reflection lines are broadened by microstructural features such as fine crystallites and or non-uniform microstrains.

Alloy	Transformation temperature (°C)	Strain level 0	0.01	0.03	0.1	Fractured
Sp9c	200	√	√	√	—	√
	250	√	√	√	√	√
	300	√	√	√	√	√
Sp10c	200	√				
	250	√				
	300	√				√

Table 3.1: Samples prepared for X-ray investigation. Note that only the Sp9c sample transformed at 250°C and strained up to failure using a cross-head speed of 0.1 mm min^{-1}.

Figure 3.1 illustrates some of the stress-strain curves obtained. There is in some cases a good balance between strength and ductility. The data will be discussed further in the following chapter.

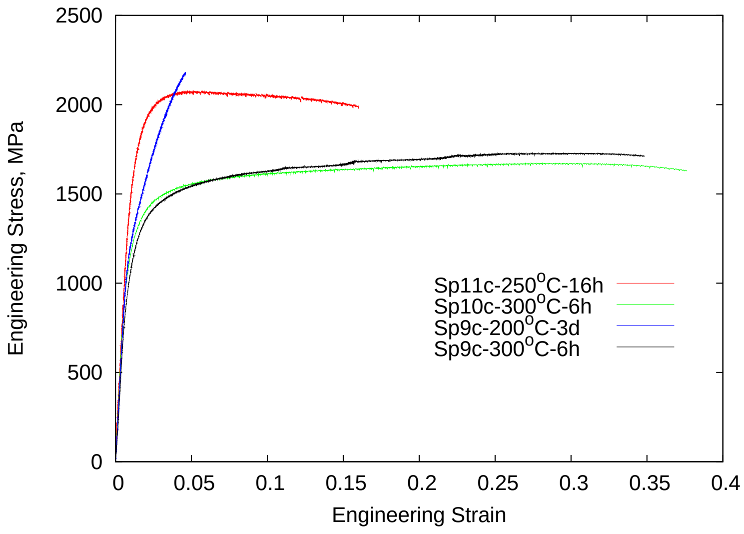

Figure 3.1: Engineering stress-engineering strain curves of the three classes of steel transformed to bainite at different temperatures.

Four discs were cut from each unloaded sample, normal to the tensile axis. They were chemically etched to remove any surface layers affected by the machining, which may introduce errors in the analysis.

A PHILIPS PW 1730 diffractometer was used, operated at 45 kV and 40 mA using unfiltered Cu-K_{α_1} radiation of wavelength 1.5406 Å. A continuous scanning mode was chosen. The angular step width was 0.025° 2θ with a collecting time about 16 s at each step. The scanned 2θ range was 32–104°, giving 5 austenite and 4 ferrite peaks.

The diffractometer optics are listed in table 3.2.

Filter	None
Divergence slit	1°
Anti-scatter slit	1°
Receiving slit	Fixed, 0.2 mm
Soller slits	None
Monochromators	Secondary, graphite

Table 3.2: X-ray diffractometer settings.

3.3 Common Errors in Counter Diffractometry

Some of the common errors are:

- Instrument misalignment;
- specimen displacement;
- zero-shift;
- flat specimen;
- transparency.

Amongst these, the specimen displacement and zero-shift errors are the most serious in lattice parameter determination [112]. Figure 3.2 shows the magnitudes of the variety of common errors in counter diffractometry [113].

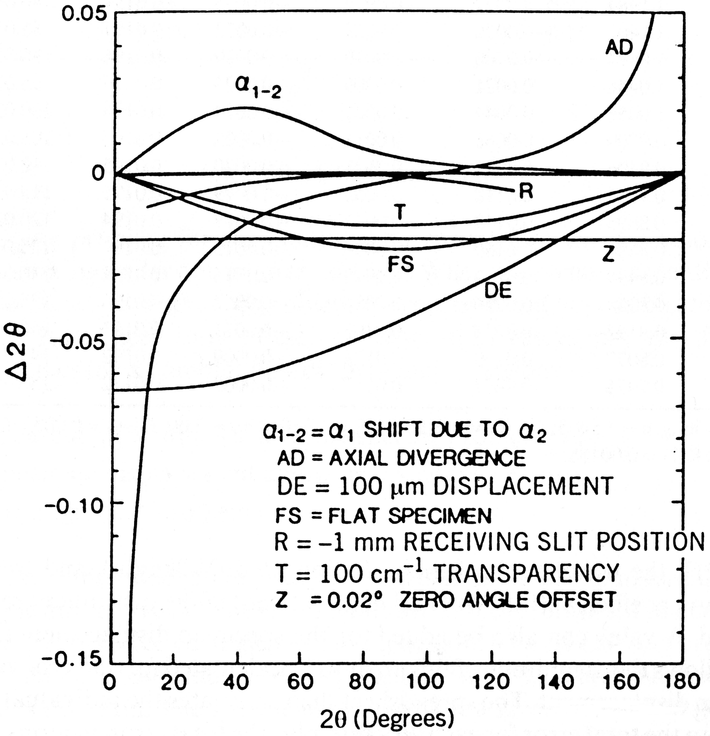

Figure 3.2: Common sources of peak shifts in X-ray diffraction. The flat specimen error was assessed by constantly illuminating 13 mm of the specimen length [113].

3.3.1 Specimen Displacement Error

Specimen-surface displacement from the goniometer axis of rotation causes peak shifts. A shift towards higher 2θ occurs if the specimen is within the focusing circle and *vice versa* [114].
The shift of peak's c.g. (centre of gravity) is given by [114]:

$$\Delta 2\theta = 2S\cos\theta / R_g \tag{3.1}$$

where $\Delta 2\theta$ is the peak shift in radians, S is the specimen displacement relative to the goniometer axis and R_g the radius of the goniometer.
It is difficult to measure the displacement S experimentally, so, other means must be considered to correct the corresponding error.

Correcting for the Specimen Displacement Error

For a cubic system, the peak shift diminishes to zero at $2\theta = 180°$, equation 3.1. A classical method to circumvent this systematic error is therefore by carrying out a simple extrapolation procedure. Extrapolation is conducted using 'apparent' lattice parameters calculated from all reflection lines of the phase concerned against a function, for instance $\cos\theta\cot\theta$, to a value of the lattice parameter a_0 where $\theta = 90°$ thereby eliminating the error.

3.3.2 Zero-shift Error

Zero-shift or zero-angle calibration error can to a large extent be avoided *via* adjustment and calibration of the diffractometer. However, it cannot be eliminated completely due to inevitable inaccuracies in the diffractometer's mechanical movement [115].

Correcting for the Zero-shift Error

In case of unindexed diffraction patterns, a correction method has previously been proposed [115]. The method uses a reflection pair whose interplanar spacing ratio is known and exact, for instance, two orders of reflection from the same crystal plane. This procedure is unnecessary here since the crystal structure of the phases (α_b,γ) is known.

Both errors, the specimen displacement and the zero-shift errors are in fact small and generally it is difficult to consider peak shifts caused by each source of error independently.

As shown in figure 3.2, for the relatively narrow angular range investigated, the specimen displacement error can be assumed to be constant and similar in magnitude to the zero-shift error.

3.3.3 Cohen's Method

Systematic and random errors causing peak shifts were corrected using the least-squares method proposed by Cohen [116], implemented in the commercial software PHILIPS X'Pert Plus which uses the Rietveld method for crystal structure refinement.

The basic principle in Cohen's method is that if the errors, which depend on the Bragg angle, can be expressed in the form of a mathematical function, the combined systematic and random errors can be eliminated from the data using the linear least-squares method. The method is analogous to the graphical extrapolation procedure discussed earlier with the advantage that it is also applicable to non-cubic crystal systems [117–119].

The quantities used in the least-squares refinement are:

$$Q_i = \frac{1}{d_i^2} = 4\left(\frac{\sin\theta_i}{\lambda}\right)^2 \tag{3.2}$$

where d_i is the interplanar spacing of the ith reflection, θ_i is its Bragg angle and λ is the wavelength.

Q_i can be written as a polynomial expression [120]:

$$Q_i = \sum_{j=1}^{m_u} a_{ij} x_j \tag{3.3}$$

where a_{ij} is the jth term coefficient, x_j is an unknown parameter and m_u is the number of unknown cell parameters.

In a general case such as the triclinic system, for a reflection i with Miller indices hkl, a_{ij} may be written as:

$$a_{i1} = h^2, a_{i2} = k^2, a_{i3} = l^2, a_{i4} = 2kl, a_{i5} = 2lh, a_{i6} = 2hk \tag{3.4}$$

and the unknown parameter, in reciprocal-lattice coordinates, can be expressed as:

$$x_1 = a^{*^2}, x_2 = b^{*^2}, x_3 = c^{*^2}, x_4 = b^* c^* \cos\alpha^*, x_5 = c^* a^* \cos\beta^*, x_6 = a^* b^* \cos\gamma^* \tag{3.5}$$

where a^*, b^*, c^*, α^*, β^* and γ^* are the reciprocal-lattice constants.
It follows that, the minimisation function can be given as [120]:

$$\Delta = \sum_i^N w_i [d^*(\text{observed})_i^2 - d^*(\text{calculated})_i^2]^2 \tag{3.6}$$

where N is the number of reflection lines, w_i is the weight assigned to each reflection line, $d^*(\text{observed})_i$ and $d^*(\text{calculated})_i$ are the observed and calculated interplanar spacings respectively. The scheme used herein was to assign the same weight for all observed reflections.

3.4 Rietveld Method

3.4.1 Cell Refinement

A crystallographic information file CIF † containing approximate lattice parameters of both crystal structures (α_b,γ) is compared with the observed reflections. Using equation 3.6, new cell parameters are calculated from the new d_{ni} values of the observed reflection lines. This process is then repeated until there is no increase in the figure of merit [121]:

$$F_N = \frac{1}{\overline{|\Delta 2\theta|}} \frac{N}{N_{\text{poss}}} \tag{3.7}$$

where $\overline{|\Delta 2\theta|}$ is the mean absolute difference between observed and calculated Bragg angles, N is the number of observed lines and N_{poss} is the number of possible reflection lines.

The analysis included the following refinable parameters:
(a) background (global parameter). Modelled as a third-order polynomial

---

† The CIF file contains information about approximate phase lattice parameter, space group, site occupation factor (taken as 1 for the iron atom in both α_b,γ) and parameters regarding the thermal displacements of atoms.

function of $2\theta_i$; (b) scale factors; (c) zero-shift error (global parameter); (d) lattice parameters; (e) profile parameters (Caglioti parameters [122]). Only U and W were refined; (discussed later in equation 3.10). No profile parameter was allowed to have a negative magnitude; (f) peak shape parameters (the mixing parameter η; equation 3.17). A single peak shape parameter was refined per phase. Peak width analysis for determining crystallite sizes and lattice effective microstrains was not performed using the Rietveld method; (g) asymmetry parameter was refined in some cases where peaks exhibited prominent asymmetry; (h) thermal parameters; and (i) preferred orientation parameters.

The refinement procedure has been carried out in a sequential manner to avoid trapping in a false minimum.

Presumably due to the initial assumption that martensite is no different from α_b, the quality of fit was not exceptionally high with GOF (goodness-of-fit) around 2% on average. Therefore, for the determination of crystallite sizes and lattice effective microstrains of phases, the *profile fitting* software PHILIPS ProFit has been utilised for this purpose which exhibited a better fit to diffraction spectra.

3.4.2 Mathematical Background

It is important to note that Rietveld method incorporates the calculation of diffraction intensity at pre-determined angular steps. A comparison *vs* the measured spectrum would thus enable adequate determination of peak positions especially in the cases where peak overlapping is pronounced. Precise lattice parameters can then be determined incorporating the previously mentioned Cohen's method.

However, the comparison between the observed and calculated intensities is carried out on the basis of the minimisation of the residual S_y given by [123]:

$$S_y = \sum_i r_i (y_i - y_{ci})^2 \tag{3.8}$$

where y_i is the total observed intensity at step i, r_i equals $1/y_i$ and y_{ci} is the calculated intensity at step i. This minimisation process is performed over the entire scanned 2θ range simultaneously. The y_{ci} value at a step i is determined from $|F_K|^2$ value (F_K is the structure factor) calculated using the provided structural model by summing over the calculated contributions from neighbouring Bragg reflections (within a specified 2θ range) in addition to the background. y_{ci} can be written as:

$$y_{ci} = s \sum_K L_K |F_K|^2 \phi_l (2\theta_i - 2\theta_K) P_K A + y_{bi} \tag{3.9}$$

where s is the scale factor, K represents Miller indices (hkl) of a Bragg reflection, L_K is a factor which contains Lorentz-polarisation and multiplicity factors, ϕ_l is the function which represents the reflection-line profile, P_K is the preferred orientation function, A is the absorption factor and y_{bi} is the background intensity at step i.

The minimisation process carried out using equation 3.8 results in a set of equations, *normal equations*, which include the derivatives of all the y_{ci}'s with respect to each refinable parameter. Consequently, an $m \times m$ matrix, *normal matrix* is created where m is the number of refinable parameters. This matrix is soluble by inversion. That is to say, during the course of structural refinement, all refinable parameters are refined as to arrive at a solution where it would ideally be the seeked minimum.

3.4.3 Correcting for Texture

As shown in equation 3.9, a correction for preferred orientation can easily be incorporated in the refinement process. Errors due to preferred orientation have been dominant in the present work since the specimens underwent large deformations up to failure.

3.5 Instrumental Broadening

The estimation of the instrumental broadening is crucial for correcting the breadths of observed reflections. Instrumental broadening was measured using Si powder with grain sizes large enough to avoid the broadening which might be caused by fine crystallites. Identical diffractometer optics and working conditions have been used throughout. The integral breadths of

Si powder reflections were determined *via* fitting the observed Si line profiles to a pseudo-Voigt function [†]. The integral breadths of Si lines were subsequently fitted to the relationship proposed by Caglioti *et al.* [122]:

$$\beta^2 = U\tan^2\theta + V\tan\theta + W \tag{3.10}$$

where β is the broadening measured at Bragg angle θ and U, V, W are the profile parameters. Although equation 3.10 is not theoretically justified, it has been used to describe the nonlinear variation of instrumental broadening with Bragg angle [125].

The values of U, V and W obtained are listed in table 3.3:

U	0.0085878
V	0.0216716
W	0.0122995

Table 3.3: Caglioti parameters for the silicon diffraction profile, used to correct for the instrumental broadening.

3.5.1 Stripping Instrumental Broadening

Stripping the instrumental broadening from observed integral breadth depends on the shape of the peak considered.

For purely Lorentzian peaks:

$$\beta_{obs} = \beta_{size} + \beta_{strain} + \beta_{inst} \tag{3.11}$$

and for purely Gaussian peaks:

$$\beta_{obs}^2 = \beta_{size}^2 + \beta_{strain}^2 + \beta_{inst}^2 \tag{3.12}$$

where β_{obs} is the observed integral breadth, β_{size} is the integral breadth due to fine crystallites, β_{strain} is the integral breadth due to lattice microstrain and β_{inst} is the integral breadth due to instrument.

[†] Integral breadth β has been used in the present work as a measure of 'peak width' rather than FWHM (full width at half maximum) since the former is believed to make more use of the data. Furthermore, it was reported that the use of FWHM overestimates crystallite sizes and underestimates effective lattice microstrains [124].

Since the general case here is that a peak width is a mix of L and G components, for mixed shape peaks, the data were analysed twice as if peak shapes are purely Lorentzian and once more as if they are purely Gaussian. Accordingly, it was believed that the 'real' value would lie in between these Lorentzian and Gaussian values. That is to say, after stripping the instrumental broadening, two crystallite size values [†] and two lattice microstrain values were obtained per experiment. Therefore, microstructural features of a phase were assessed by means of a range of values whose limits represented the parameter's values obtained assuming pure Gaussian or pure Lorentzian peak shapes. The actual parameter's value would therefore lie within the given range.

It is important to note that values obtained by this technique are not absolute, rather, they are relative values given the complex nature of the problem [117].

3.6 Crystallite Size & Microstrain

It is known that peak broadening in diffraction patterns occurs due to the presence of fine crystallites or 'diffracting domains', as well as residual stresses in grains [118].

Non-uniform straining of grains causes peak broadening in diffraction patterns whereas the practically rare uniform strain induces peak shifts as shown in figure 3.3.

It is therefore problematic to separate the broadening due to different sources in the case at hand since both sources of line broadening co-exist.
However, a suitable method for separating broadening due to crystallite size and strain has earlier been proposed by Hall [126] and Williamson and Hall [127].

3.6.1 Williamson-Hall Plot

The Williamson-Hall plot, as shown in figure 3.4, can be used to separate the broadening due to crystallite size and lattice microstrain with the *implicit*

[†] Crystallite size determined in the present work represents the volume-average [118].

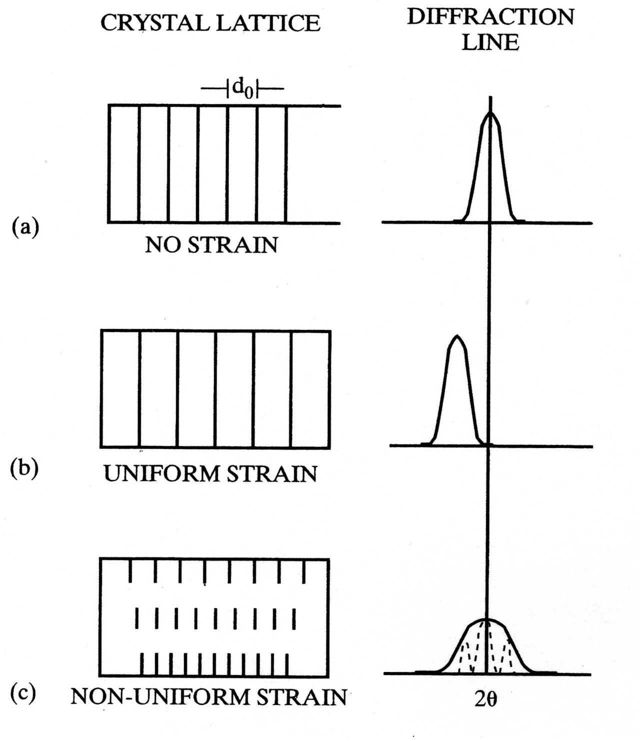

Figure 3.3: Peak shifts and broadening due to crystal strain [118]. d_0 is the equilibrium spacing.

assumption that peak shapes are Lorentzian.

The total integral breadth ($\beta_{obs} - \beta_{inst}$) can be expressed as [126, 128]:

$$\beta_{tot} = 2\zeta \tan\theta + \frac{K_s \lambda}{D \cos\theta} \tag{3.13}$$

where 2ζ is the effective lattice microstrain, θ is the Bragg angle, K_s is the shape factor, λ is the wavelength of the radiation used and D is the crystallite size.
The right-hand term is classically named after Scherrer.

K_s in fact is *not* a constant. Its value is usually taken as 1 but it can range from 0.7–1.70 depending on factors such as the crystallite shape and the width-measure, whether it is the FWHM or the integral breadth [117]. In the present investigation, since the integral breadth was considered, K_s value was taken to equal 1.05 [117].

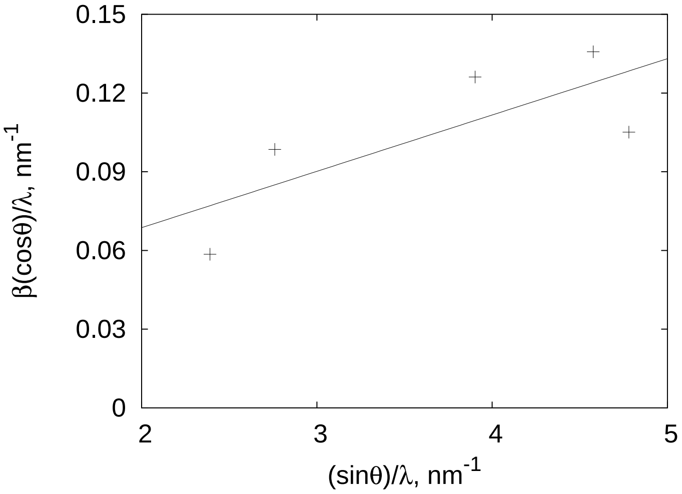

Figure 3.4: Williamson-Hall plot of the austenite phase in sample Sp9c transformed at 300°C and strained up to 0.1 ε.

Equation 3.13 can be re-written as:

$$\frac{\beta_{tot}\cos\theta}{\lambda} = \frac{1.05}{D} + 2\zeta\frac{\sin\theta}{\lambda} \tag{3.14}$$

Plotting equation 3.14 gives the Williamson-Hall plot where the intercept of the fitted straight line with y axis approximately yields the inverse of the crystallite size and the slope yields the effective lattice microstrain.

With the assumption that lattice microstrains and fine crystallite size induce Gaussian peak shape, the following equation assumes that the squares of the breadths are additive [117, 127]:

$$\beta_{tot}^2 = (2\zeta\tan\theta)^2 + \left(\frac{1.05\lambda}{D\cos\theta}\right)^2 \tag{3.15}$$

Therefore, equation 3.15 has also been utilised in the current analysis.

Line profiles were fitted to a pseudo-Voigt function using the software package PHILIPS ProFit. The package allowed a flexible control over the refinement process and provided a high degree of accuracy in profile fitting with average minimised R-factor of no more than few tenths per cent.

The minimised R-factor is given by:

$$R_{min} = \frac{\sum_i (y_i - y_{ci})^2}{\sum_i (y_i - b_i^{tot})^2} \tag{3.16}$$

where b_i^{tot} is the total background intensity. All intensities are in counts. The pseudo-Voigt function is:

$$\mathrm{p-V} = \eta L + (1-\eta)G \tag{3.17}$$

where L is the Lorentzian component, G is the Gaussian component and η is the mixing parameter.

During the profile fitting procedure, η was refined to capture the weights of both components L and G in each peak width. This refinement yielded an excellent fit; almost all peak shapes observed were a mix of Lorentzian and Gaussian functions.

3.7 Microstructural Parameters

3.7.1 Sp9c–Transformed at 200°C

Lattice parameters of both phases, austenite and bainitic ferrite in alloy Sp9c transformed at 200, 250 and 300°C were obtained as a function of the applied plastic strain and up to the fracture point.

In a recently published study on conventional TRIP-aided steels with the microstructure generally composed of austenite/athermal martensite in a ferrite matrix, the effect of plastic deformation in uniaxial tension on austenite and ferrite lattice parameters was not clear [129]. The authors could not perform a least-squares linear fit to calculated apparent lattice parameters of observed reflection lines due to nonlinearities.

As shown in figure 3.5(a), in Sp9c transformed at 200°C, the general trend of the austenite lattice parameter is that it decreases as a function of strain. However, after an initial drop in a_γ value, a_γ seemed to remain constant at intermediate strains before fracture. As shown in figure 3.5(b), a similar trend was also observed for a_{α_b}. It was noticeable, however, that a_{α_b} at 0.03 strain level exhibited the highest value in this series of experiments.

In the work of Streicher-Clarke *et al.*, the effect of deformation in biaxial tension and plane strain on the austenite and ferrite lattice parameters

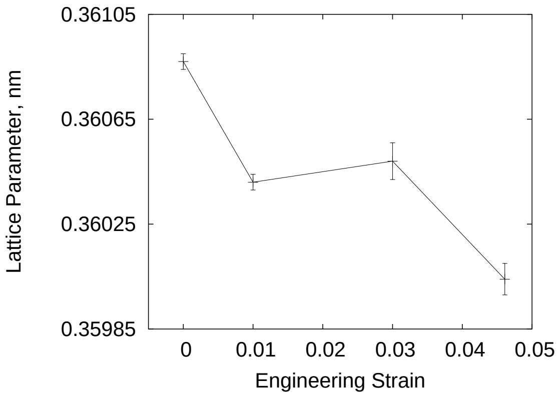

(a) Change in a_γ *vs* strain

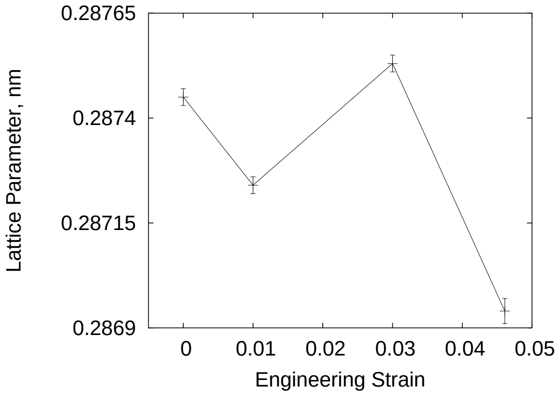

(b) Change in a_{α_b} *vs* strain

Figure 3.5: Lattice parameter change with strain of the alloy Sp9c transformed at 200°C.

was found to increase the lattice parameter of both phases as strain increased [129].

It might be possible to relate lattice parameter changes with strain to the residual stresses which may present. However, an assessment of the residual stresses in a phase on the basis of the change in its lattice parameter is arguable [130] and the classical method to determine the state of the phase is by conducting the $\sin^2\psi$ analysis method[†] [118, 131]. Furthermore, in

---

[†] Residual stresses are calculated using the expression: $\frac{d_{\phi\Psi}-d_0}{d_0} = \frac{1+\nu}{E_y}\sigma_\phi \sin^2\Psi - \frac{\nu}{E_y}(\sigma_{11}+\sigma_{22})$, where $d_{\phi\Psi}$ is the d-spacing of the crystal planes oriented at an angle Ψ to the surface normal, ν is Poisson ratio, E_y is Young modulus, σ_{11} and σ_{22} are the principal stresses parallel to the surface and σ_ϕ is the measured stress, in a direction at

heavily deformed steel structures, diffraction data are normally collected from anisotropically distorted crystals which make the analysis more difficult as shall be presented in the following section.

In fact, as far as the austenite phase is concerned, an increase in a_γ can sometimes be ascribed to compositional changes due to selective martensitic transformation which preferentially takes place in austenite regions with lower carbon content [60, 132].

According to Sugimoto *et al.*, tensile deformation of low-alloy TRIP-aided dual-phase steels induces compressive residual stresses in ferrite while the harder phase, the austenite, was reported to be under tensile residual stresses [133]. Similar results were also reported by Song *et al.* where pre-straining of a steel microstructure with bainitic ferrite as the matrix yielded residual stresses in both phases [134]. In their work, the amount of compressive residual stresses developed in the bainitic ferrite matrix was lower than that observed in steels with polygonal ferrite and annealed martensite matrices. This was ascribed to the smaller amount of the 'second phase' (the retained austenite) in the former case. That is to say, these residual stresses are a result of the interaction of stress fields caused by martensitic transformation and macrostresses due to plastic deformation.

Streicher-Clarke *et al.* carried out the $\sin^2\psi$ analysis to further investigate their observation regarding the increase in the ferrite lattice parameter with strain [129]. The residual stress state of the austenite phase was not assessed using this analysis. It was possible to confirm compressive residual stresses in ferrite parallel to the sheet surface. The increase in apparent ferrite lattice parameters with effective strain was ascribed to tensile strains normal to the surface which was attributed to a Poisson effect given the fact that the stress perpendicular to the sheet surface is zero [129].

The $\sin^2\psi$ analysis was also performed on samples deformed in uniaxial tension [129]. Less compressive stress values were observed in comparison with biaxial tension and plane strain samples, which was explained as a result of the enhanced accommodation of the ferrite matrix relative to the $\gamma \rightarrow \alpha'$

---

an angle ϕ to σ_{11}. By plotting $\frac{d_{\phi\Psi}-d_0}{d_0}$ *vs* $\sin^2\Psi$, the stress σ_ϕ can be calculated if E_y, ν and d_0 are known.

transformation in uniaxial tension.
Interestingly, Streicher-Clarke *et al.* suggested the increase in the apparent austenite lattice parameters with effective strain to be caused by 'surface compressive residual stresses' [129]. The authors admitted the difficulty associated with having residual stresses with the same sign in both phases.

For the case at hand, it is speculated that the austenite phase was in tension, however, during the course of straining martensitic transformation decreased the level of the tensile residual stress [133].

As for bainitic ferrite, the initial increase in a_{α_b} at 0.03 strain could be explained in terms of the development of tensile strain normal to the sample surface caused by a Poisson effect, which suggests the bainitic ferrite planes parallel to the surface being under compression. This is difficult to confirm without further analysis using the $\sin^2\psi$ technique.
However, the general trend of a_{α_b} is that it decreases with strain suggesting increasing the degree of compressive residual stress.

For this particular sample the tensile load was the greatest with strength above 2 GPa (figure 3.1).

Figure 3.6 shows estimated crystallite sizes and microstrains of austenite as a function of tensile strain. As expected, the γ crystallite size tends to decrease with strain [†]. Figure 3.6(b) represents the austenite-lattice effective microstrain *vs* applied macrostrain.

As shown in figure 3.6(b), data at 0.03 ε could not be fitted and in general there seem no change in the austenite lattice microstrain with macrostrain.

3.7.2 Sp9c–Transformed at 300°C

As shown in figure 3.7(a), the behaviour of this specimen resembles that which transformed at 200°C.

Figure 3.7(b) shows that the bainitic ferrite apparently exhibiting compressive residual stresses with macrostrain, with a slight increase in a_{α_b} at 0.1 ε, presumably due to structural anisotropy.

[†] Note that in some cases, due to data scattering caused by anisotropies, reflection lines width could only be fitted assuming Lorentzian or Gaussian peaks profile. Hence crystallite size range was represented by a single data point.

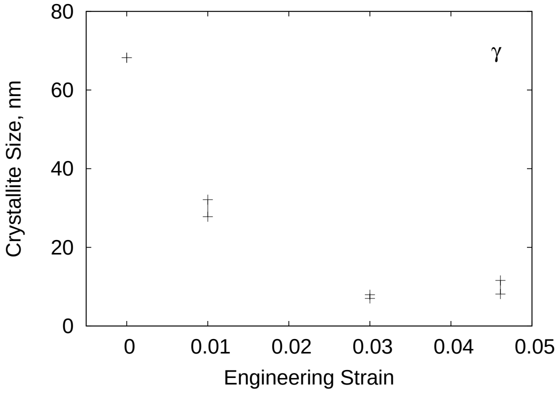

(a) Change in crystallite sizes *vs* strain

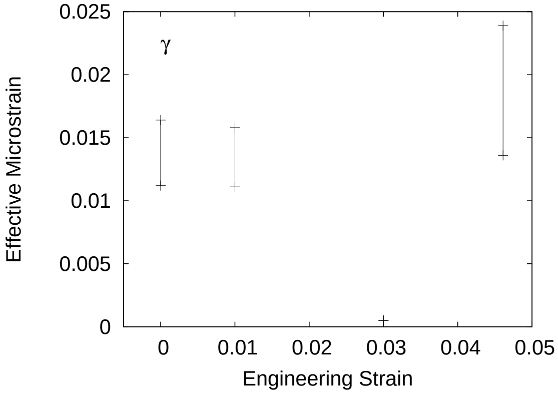

(b) Effective lattice microstrain *vs* strain

Figure 3.6: Microstructural parameters of the retained austenite in alloy Sp9c transformed at 200°C *vs* strain.

As presented in figure 3.8(a), the variation of retained austenite crystallite sizes as a function of macrostrain of steel Sp9c transformed at 300°C exhibited a similar trend compared with transformation at 200°C. However, the coarser initial grains have a wider range of sizes in comparison with the latter case. Crystallite size at fracture (0.35 ε) was found to be very fine 7.3–7.6 nm.

Effective microstrain data *vs* macrostrain were not clear, figure 3.8(b). Furthermore, the regression line in the Williamson-Hall plot for the fractured specimen's data could not be fitted.

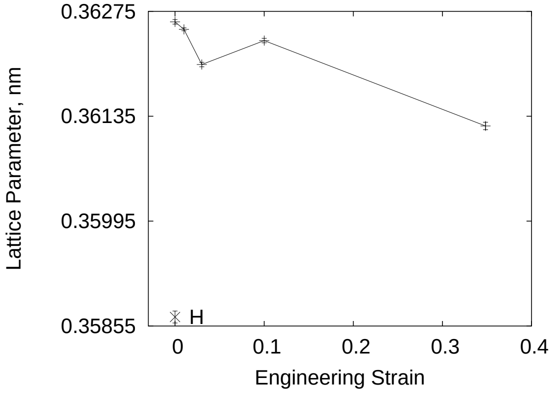

(a) Change in a_γ *vs* strain

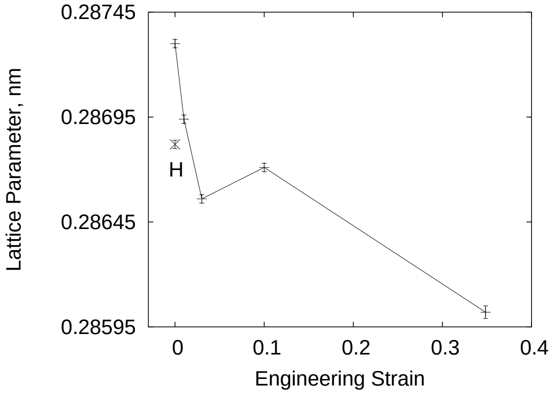

(b) Change in a_{α_b} *vs* strain

Figure 3.7: Lattice parameter change with strain of the alloy Sp9c transformed at 300°C. (H) represents specimen continuously heated from 35 to 600°C with 25°C min^{-1}.

3.7.3 Sp9c–Transformed at 250°C

As shown in figure 3.9, the austenite and bainitic ferrite in the steel transformed at 250°C behave differently when compared with steels transformed at 200 and 300°C.

As shown in figure 3.9(a), the initial increase in a_γ with macrostrain suggests that austenite is under tension which might be expected. It is also clear that the lattice parameter value was almost constant in latter stages of deformation up to failure, presumably caused by martensite transformation.

On the other hand, the results of a_{α_b} were not clear and it is difficult to

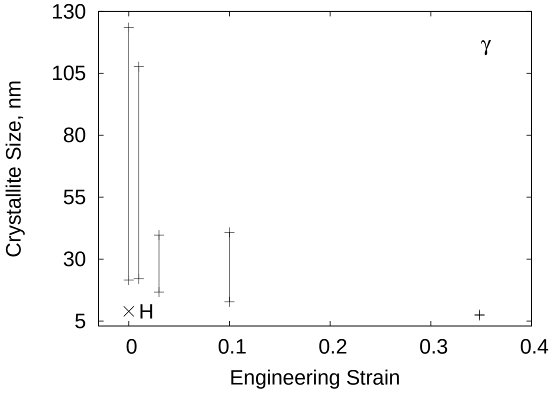

(a) Change in crystallite sizes *vs* strain

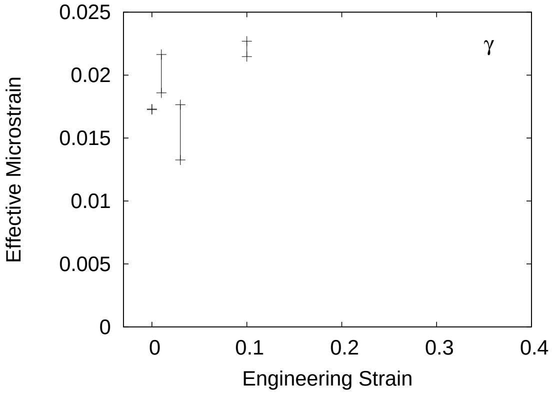

(b) Effective lattice microstrain *vs* strain

Figure 3.8: Retained austenite microstructural parameters of the alloy Sp9c transformed at 300°C *vs* strain. Data point (H) denotes a specimen which underwent continuous heating from 35–600°C with 25°C min^{-1}–will be discussed in the following sections.

make a conclusion as to the state of the bainitic ferrite phase.

As shown in figure 3.10, the trends are similar to previous steels transformed at different temperatures. Coherent diffracting domains in austenite exhibit smaller sizes with greater plastic strain. The experimental results presented in figure 3.10(b) are not conclusive. However, there might be a tendency towards lower lattice microstrain in the austenite with higher plastic strain levels. Lattice microstrains calculated from peak broadening do not give an indication to the nature of the strain whether compressive or tensile [118].

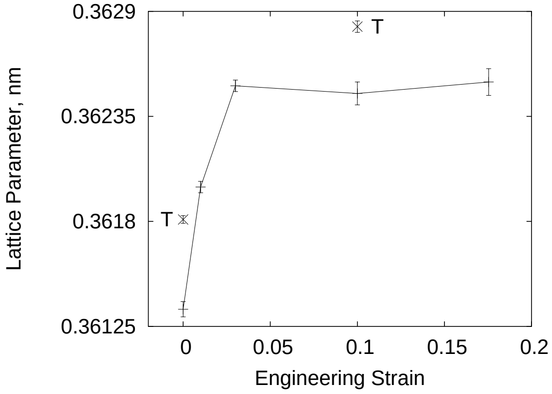

(a) Change in a_γ *vs* strain

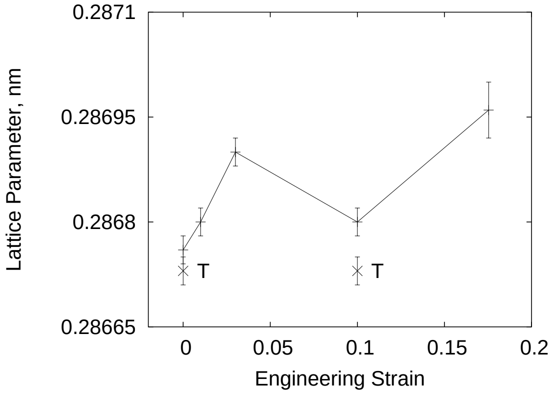

(b) Change in a_{α_b} *vs* strain

Figure 3.9: Lattice parameters change with strain of the alloy Sp9c transformed at 250°C. (T) indicates that the X-ray specimen has been tempered at 300°C for 2 h.

Apparently, any analysis based on the change of the lattice parameter and or effective lattice microstrain is not sufficient to indicate the state of the residual stress in a phase within a mixed microstructure. For the austenite phase for example, considering the rate by which the austenite transforms into martensite which develops compressive residual stresses in γ, and microstrains introduced during macrostraining might give a further clue. The initial state of the phase concerned, and the nature of surrounding phases are also important parameters. It has been proved that the phases in unstrained as-transformed steel microstructures are not stress-free [135]. Bainite trans-

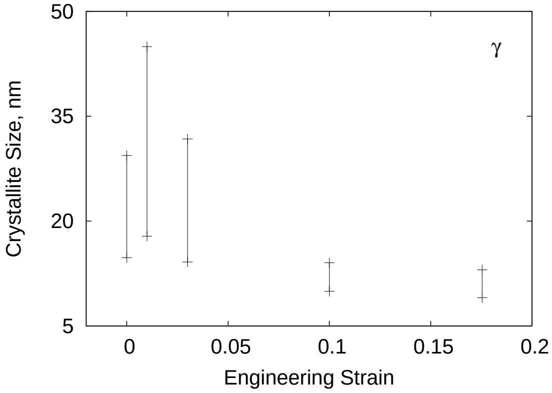

(a) Change in crystallite sizes *vs* strain

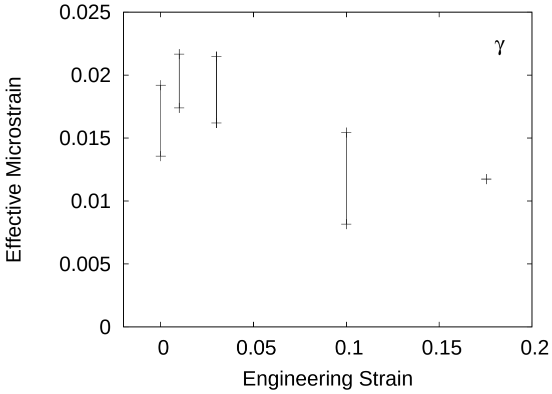

(b) Effective lattice microstrain *vs* strain

Figure 3.10: Microstructural parameters of the retained austenite in alloy Sp9c transformed at 250°C as a function of strain.

formation itself is accompanied by shape and volume changes which is the case with martensitic transformation. Many parameters have to be taken into account to understand the overall microstructural behaviour.

3.7.4 Bainitic Ferrite

The overlap of martensite peaks with those of bainitic ferrite may bias the data obtained *via* line profile analysis. So, only bainitic ferrite peaks recorded in the as-transformed unstrained samples were analysed.

Figure 3.11(a) shows the reduction of the average α_b crystallite size in Sp9c as the transformation temperature is lowered . Figure 3.12(a) shows a similar trend for alloy Sp10c. This is consistent with previous work reported by Sandvik and Nevalainen [92] and Chang and Bhadeshia [93] using transmission electron microscopy.

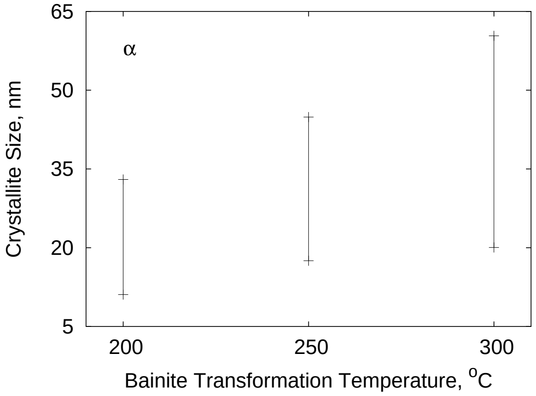

(a) Variation of α_b crystallite size *vs* transformation temperature

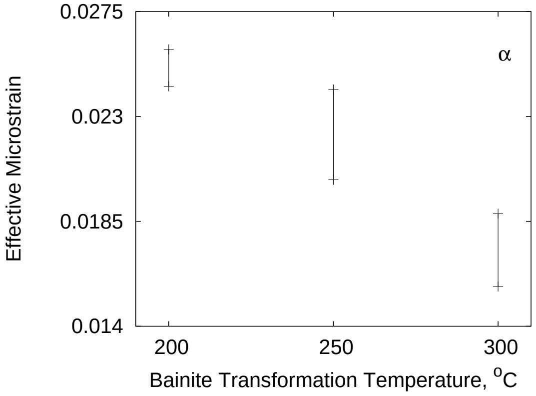

(b) Variation of α_b crystal lattice microstrain *vs* transformation temperature

Figure 3.11: Microstructural parameters of the bainitic ferrite phase in Sp9c unstrained specimens as a function of transformation temperature.

In figure 3.11(b), the effective lattice microstrains developed in α_b during bainite transformation were higher at lower temperatures. Similar results were observed in steel Sp10c (figure 3.12(b)). The results in figures 3.11(b) and 3.12(b) suggest higher dislocation density in bainite formed at lower temperatures [2].

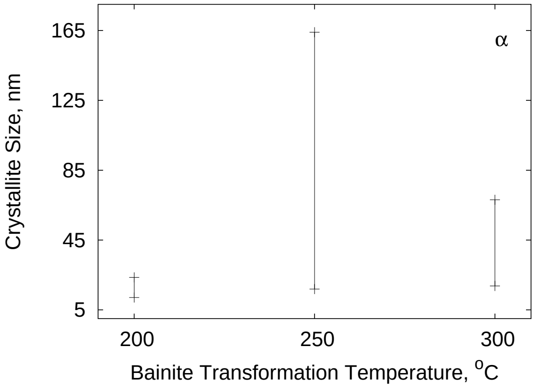

(a) Variation of α_b crystallite size *vs* transformation temperature

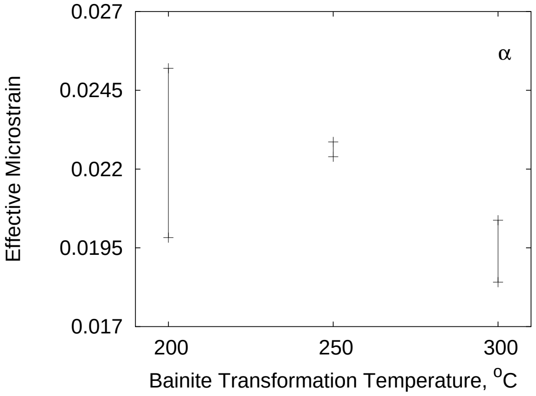

(b) Variation of α_b crystal lattice microstrain *vs* transformation temperature

Figure 3.12: Microstructural parameters of the bainitic ferrite phase in Sp10c unstrained specimens as a function of transformation temperature.

Summary

Tensile deformation at ambient temperature leads to complex changes in the austenite lattice parameter, which can be ascribed to compositional change and or the presence of residual stresses. Strain-induced martensite relaxes the stresses in austenite crystals. Bainitic ferrite plates decrease in scale as transformation temperature is lowered. Transformation at lower temperatures also results in a higher dislocation density. Measured austenite crystallites were finer as plastic strain increased. Changes in lattice parameters and effective lattice microstrains do not reveal the sign of the residual stress. Further experimental assessment is thus needed.

Effect of Tempering

The effect of low-temperature tempering (at 300°C for 2 h) on Sp9c (250°C) was presented in figure 3.9. There is an increase in a_γ caused by tempering in both the unstrained and strained (0.1 ε) specimens.

Barbé *et al.* studied the properties of a laboratory casting of metastable austenite with a composition similar to that found in TRIP-aided steels [136]. The austenite composition was Fe-1.87C-1.53Mn-1.57Si wt%. Following deformation, a heat-treatment at 300°C for 20 minutes caused a_γ to revert to its pre-deformation value [136]. A similar finding has recently been reported by Kaputkin *et al.* [137]. Given the high-silicon content in Sp9c, and the low tempering temperature, it is unlikely that carbide precipitation took place [138]. The increase in a_γ due to tempering can therefore be explained in terms of carbon partitioning from α_b into γ. On the other hand a_{α_b} decreased by tempering. Partitioning of carbon atoms to austenite during tempering has been reported by van Genderen *et al.* [139]. In the current case, the carbon content in retained austenite using the new value of a_γ yielded 1.33 wt% carbon instead of the previously calculated value of 1.16 wt%.

It is also possible to ascribe the decrease in a_{α_b} to carbon atoms segregation to lattice defects within the bainitic ferrite [140].

The austenite lattice microstrain was found to be nearly unchanged in both the tempered (0.0102–0.0154) and untempered (0.0082–0.0154) strained specimens. Austenite crystallite size calculations for the tempered specimen showed a coarser austenite crystallites of 14–23 nm compared with 10–14 nm in the untempered specimen. It is possible that the tempering process resulted in the formation of a larger defect-free domains, probably through dislocation rearrangements.

The same trends were also observed for the unstrained, untempered and tempered specimens. However, the increase in austenite crystallite size was greater from 15–29 nm to 25–154 nm upon tempering at 300°C for 2 h.

Transformed at, (°C)	**Sp9c** a_γ nm	C_γ wt%	**Sp10c** a_γ nm	C_γ wt%
200	0.36087±0.00003	1.00±0.01	0.36114±0.00003	0.91±0.01
250	0.36134±0.00004	1.16±0.02	0.36320±0.00003	1.63±0.01
300	0.36261±0.00003	1.60±0.01	0.36303±0.00002	1.57±0.01
300-3 h+ 250-7 h	—	—	0.36330±0.00004	1.67±0.01

Table 3.4: Carbon content in retained austenite of Sp9c and Sp10c specimens after the completion of the bainitic transformation. Specimens are as-transformed.

3.7.5 Austenite Carbon Content

The carbon content in austenite was calculated using the following relationship [141–143]:

$$\begin{aligned} a_\gamma(\text{nm}) = 0.35770 + 0.00065 \times \text{C} + 0.00010 \times \text{Mn} \\ -0.00002 \times \text{Ni} + 0.00006 \times \text{Cr} + 0.00056 \times \text{N} \\ +0.00028 \times \text{Al} - 0.00004 \times \text{Co} + 0.00014 \times \text{Cu} \\ +0.00053 \times \text{Mo} + 0.00079 \times \text{Nb} + 0.00032 \times \text{Ti} \\ +0.00017 \times \text{V} + 0.00057 \times \text{W} \end{aligned} \tag{3.18}$$

where concentrations are in at.%.

The calculated carbon contents in the retained austenite in steels Sp9c and Sp10c heat-treated under various conditions are presented in table 3.4. The results represent unstrained specimens to avoid confusion from residual stresses effects.

Despite the increase in bainite that can form at lower temperatures, the retained austenite does not further enrich, reportedly because of the trapping of carbon in defects in bainitic ferrite [102]. After all, the dislocation density in bainitic ferrite also increases as the transformation temperature is reduced [2].

In steel Sp9c, the maximum C_γ was achieved upon transforming at 300°C.

This was not the case in steel Sp10c which peaked in C_γ at 250°C instead of 300°C.

Effect of Heating to High Temperature

As shown in figure 3.7, (points marked H), an unstrained Sp9c specimen transformed at 300°C was continuously heated from 35 at 25°C min^{-1} to 600°C in a tube-furnace with a dynamic atmosphere of commercial purity argon. This resulted in the transformation of austenite into ferrite and carbides with some of the austenite retained with a_γ of 0.35867±0.00008 nm corresponding to 0.24 ± 0.03 wt% carbon (figure 3.13).

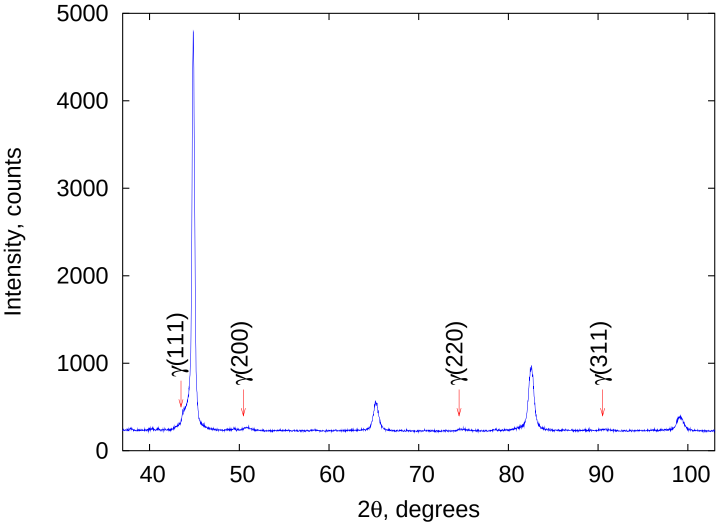

Figure 3.13: X-ray diffraction pattern of Sp9c specimen transformed at 300°C, unstrained, then continuously heated from 35 to 600°C at 25°C min^{-1}. Note that some austenite reflections remain.

The remaining austenite phase fraction was estimated to be 0.075 ± 0.015. The presence of austenite after heating to 600°C is indicative of the high resistance against decomposition. a_{α_b} was also found to decrease with heating to 600°C, presumably due to carbide precipitation.

In figure 3.8, the observed austenite crystallite size ranged from 8.9–9 nm, less than the minimum value in the starting microstructure. Nevertheless, the measured austenite fraction is very small, consequently, it is thought that the observation of a smaller crystallite size is a result of experimental error introduced by only measuring a small number of austenite regions, rather than being a real physical effect. The effective lattice microstrain could not be determined for this sample.

3.7.6 Comparison with Alloy Sp10c

Lattice Parameters

Sp10c has a larger a_γ relative to alloy Sp9c for the same transformation temperature, figure 3.14 and table 3.4. This is indicative of greater carbon-enrichment in the austenite in Sp10c. This is justified since, for the same transformation period, the content of bainite is greater in the more rapidly transforming Sp10c.

Figure 3.14(a) shows the decrease in a_γ of both Sp9c and Sp10c as the bainite transformation temperature is lowered.

In figure 3.14(b), a_{α_b} in steel Sp10c was observed to increase steadily with decreasing transformation temperature. The same trend was observed for alloy Sp9c with the exception of the specimen transformed at 250°C. This lattice parameter increase is consistent with an increase in carbon content.

Lattice Microstrains

Figure 3.15 represents the microstrains in Sp9c and Sp10c as-transformed samples.

Over the entire transformation temperature range, the higher microstrain in γ of Sp10c compared with Sp9c is consistent with the austenite lattice parameters in both alloys. The higher austenite microstrains in Sp10c are therefore due to compositional changes from carbon partitioning into the austenite.

3.7.7 Lattice Distortion

Figure 3.16 shows the lattice parameters of austenite and bainitic ferrite in steel Sp10c transformed at 300°C, unstrained and fractured at 0.376 ε. Two diffraction patterns were recorded from differently oriented samples of the fractured steel (figure 3.17). One sample was cut such that, its surface was

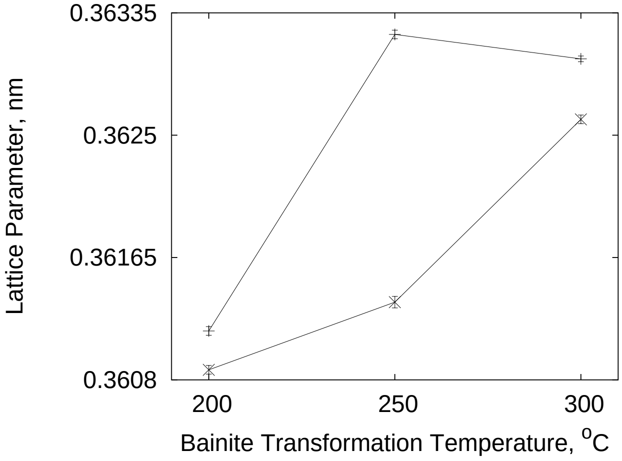

(a) Change in a_γ *vs* transformation temperature

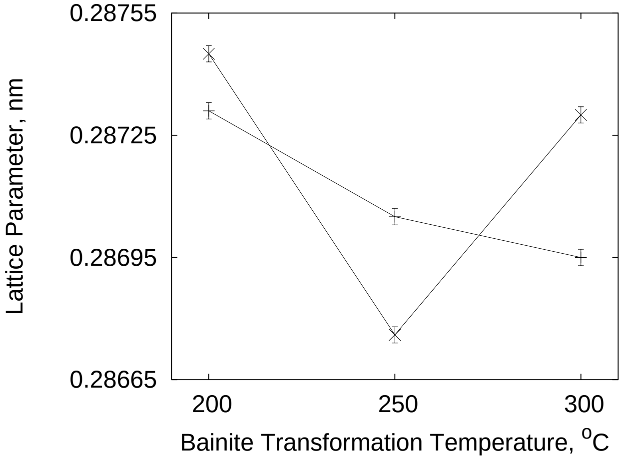

(b) Change in a_{α_b} *vs* transformation temperature

Figure 3.14: Lattice parameter change with bainite transformation temperature of the alloy Sp9c (×) and Sp10c (+). Unstrained specimens.

orthogonal to the loading axis (data marked +). The other was cut with the characterised surface parallel to the tensile axis (data marked ×).

As shown in figure 3.16, different austenite and bainitic-ferrite lattice parameters were observed in the fractured specimen depending on the orientation. This suggests heterogeneous lattice distortion caused by the plastic deformation.

In a recent study on austenitic stainless steel by Taran *et al.*, the ax-

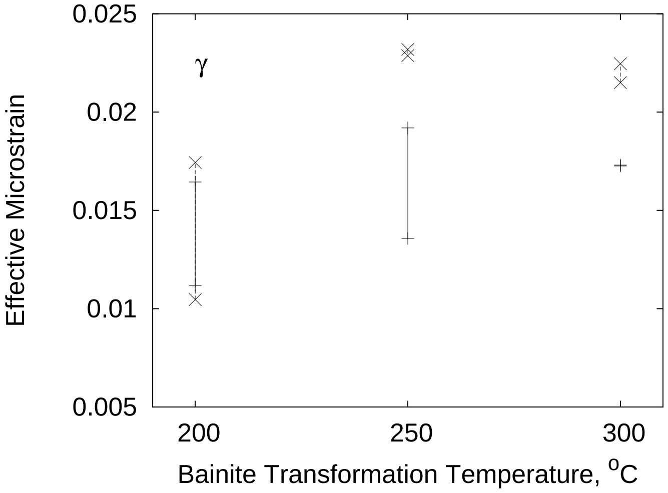

Figure 3.15: Austenite lattice microstrain *vs* bainite transformation temperature. Unstrained specimens. (+) and (×) denote Sp9c and Sp10c specimens respectively.

ial and transverse lattice parameters of the austenite and also those of the martensite were found not to be identical even in the unstressed condition [135]. This was attributed to possible deviatoric residual stresses which may arise as a result of processing. It clearly is difficult to assess lattice parameters of heavily plastically deformed steel microstructures.

3.7.8 Preferred Orientation

The grains in a steel microstructure may be preferentially crystallographically oriented due to processing. This texture causes systematic changes in line intensities in X-ray diffraction patterns [123].

To reduce the effect of texture, a rotating sample holder was used to enhance grain sampling [144, 145].
Sample oscillation around the diffractometer axis combined with rotation has been reported to provide better results [146]. Will *et al.* tested this method but it did not yield conclusive results [147].

Assuming axial symmetry about the scattering vector, the error due to texture can be corrected for by determining a single 'pole-density profile' [148]. Alternatively, this profile can be modelled using a mathemati-

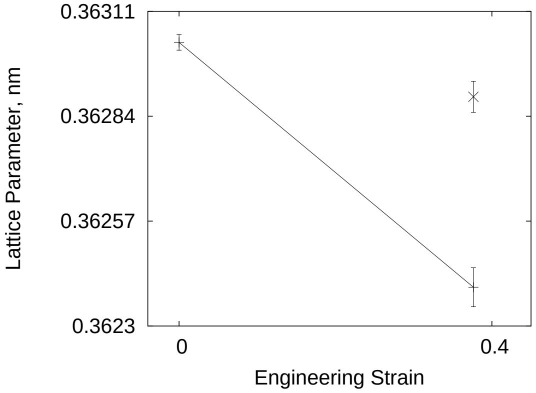

(a) Change in a_γ *vs* strain

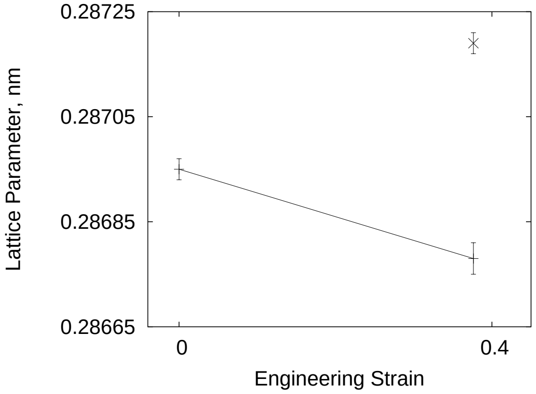

(b) Change in a_{α_b} *vs* strain

Figure 3.16: Lattice parameters change with strain of the alloy Sp10c transformed at 300°C. Data points marked (+) and (×) represent the specimens cut perpendicular and parallel to the sample axis respectively.

cal function whose parameters are included and refined in the least-squares crystal structure refinement procedure embedded in the Rietveld method. Amongst the available functions proposed in the literature (presented in [148]) March-Dollase function was implemented in the software package PHILIPS X'Pert Plus since it has been proved to provide a better performance [123, 148, 149]:

$$P_K = (G_1^2 \cos^2\vartheta + (1/G_1)\sin^2\vartheta)^{-3/2} \tag{3.19}$$

where G_1 is the refinable parameter and ϑ is the angle between the scattering

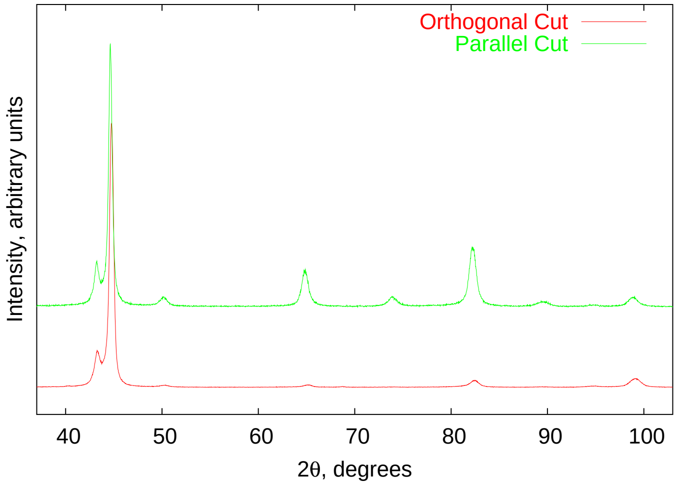

Figure 3.17: X-ray diffraction patterns measured in Sp10c sample transformed at 300°C and fractured. Two specimens were prepared for diffractometry; cutting planes of the specimens were orthogonal and parallel to the sample axis.

vector and the normal to the crystallites.

As previously demonstrated in equation 3.9, equation 3.19 is embedded in the Rietveld method thereby a mathematical correction for the preferred orientation problem was possible. As shall be presented in the following sections, a successful correction process would manifest itself if similar phase fractions could be obtained using the two apparently different diffraction patterns shown in figure 3.17.

Estimation of Preferred Orientation Direction

This is necessary for the texture error correction process embedded in Rietveld refinement. The estimation of the planes which are preferentially oriented parallel to the specimen's surface, *i.e.* orthogonal to the scattering vector, was carried out for each phase by comparing the relative intensities of the observed peaks with those calculated using standard diffraction patterns published by the International Union of Crystallography.

Ideally, texture parameters are determined using the classical pole figure, however, this is very time consuming.

Allowing for preferred orientation refinement resulted in a very significant reduction in the value of GOF therefore a proper fitting of the observed diffraction patterns was possible.

Using the refined lattice parameters of austenite and bainitic ferrite, a further investigation was carried out using the method proposed by Dickson [150] for the estimation of texture parameters.

For bainitic ferrite α_b, a texture parameter $P^*_{\alpha_b}$ in a dual-phase microstructure (α_b and γ) may be defined as:

$$P^*_{hkl_{\alpha_b}} = \frac{I_{hkl_{\alpha_b}}/R_{hkl_{\alpha_b}}}{\frac{1}{n_{\alpha_b}}\sum_0^{n_{\alpha_b}}(I_{\alpha_b}/R_{\alpha_b}) + \frac{1}{n_\gamma}\sum_0^{n_\gamma}(I_\gamma/R_\gamma)} \tag{3.20}$$

where I_{hkl} is the integrated intensity of the hkl reflection, n is the number of phase peaks observed and R_{hkl} is a factor given by:

$$R_{hkl} = \left(\frac{1}{\mathrm{V}^2}\right)\left(|F_K|^2 p(\frac{1+\cos^2 2\theta}{\sin^2\theta\cos\theta})\right)(e^{-2M}) \tag{3.21}$$

where V is the unit cell volume, p is the multiplicity factor, $(\frac{1+\cos^2 2\theta}{\sin^2\theta\cos\theta})$ is the Lorentz-polarisation factor and e^{-2M} is the temperature factor.

Although there was uncertainty in the texture history of the manufactured tensile test samples, all cut samples shared identical orientation in the as hot-rolled steel.

Using Dickson's method, the texture parameter P^* for each reflection line could be determined as presented in tables 3.5, 3.6 and 3.7.

As shown in tables 3.5 and 3.6, the highest values for P^* were observed for $\{110\}_{\alpha_b}$ and its higher order reflection $\{220\}_{\alpha_b}$ at 0.1 ε and fracture strain.

Unlike the samples which underwent bainite transformation at relatively higher temperatures, the alloy transformed at 200°C was observed to possess the highest values for the texture parameter in the $\{110\}_{\alpha_b}$ and the $\{211\}_{\alpha_b}$ reflection lines at 0.03 engineering strain and fracture strain.

	P^*				
Engineering strain	0	0.01	0.03	0.1	0.348 (F)
$\{111\}_\gamma$	0.42	0.30	0.32	0.39	0.34
$\{110\}_{\alpha_b}$	0.63	0.77	0.81	1.11	1.54
$\{200\}_\gamma$	0.37	0.33	0.43	0.25	0.06
$\{200\}_{\alpha_b}$	0.56	0.78	0.48	0.43	0.16
$\{220\}_\gamma$	0.46	0.29	0.30	0.13	NA
$\{211\}_{\alpha_b}$	0.66	0.69	0.71	0.57	0.30
$\{311\}_\gamma$	0.36	0.27	0.42	0.19	NA
$\{222\}_\gamma$	0.36	0.23	0.23	0.31	0.16
$\{220\}_{\alpha_b}$	0.58	0.63	0.65	0.87	1.26

Table 3.5: Variation of texture parameter of reflection lines of the alloy Sp9c transformed at 300°C with strain. 'F' denotes fractured.

	P^*				
Engineering strain	0	0.01	0.03	0.1	0.175 (F)
$\{111\}_\gamma$	0.33	0.25	0.30	0.28	0.34
$\{110\}_{\alpha_b}$	0.74	0.91	0.98	1.36	1.37
$\{200\}_\gamma$	0.28	0.24	0.25	0.12	0.10
$\{200\}_{\alpha_b}$	0.72	0.81	0.68	0.44	0.28
$\{220\}_\gamma$	0.28	0.25	0.18	0.07	NA
$\{211\}_{\alpha_b}$	0.78	0.71	0.69	0.59	0.40
$\{311\}_\gamma$	0.24	0.18	0.17	0.08	0.02
$\{222\}_\gamma$	0.21	0.15	0.22	0.15	0.20
$\{220\}_{\alpha_b}$	0.68	0.71	0.76	1.06	1.07

Table 3.6: Variation of texture parameter of reflection lines of the alloy Sp9c transformed at 250°C with strain.

	P^*			
Engineering strain	0	0.01	0.03	0.046 (F)
$\{111\}_\gamma$	0.34	0.28	0.20	0.28
$\{110\}_{\alpha_b}$	0.72	0.89	1.08	0.99
$\{200\}_\gamma$	0.34	0.24	0.05	0.07
$\{200\}_{\alpha_b}$	0.68	0.82	0.77	0.74
$\{220\}_\gamma$	0.35	0.25	NA	0.13
$\{211\}_{\alpha_b}$	0.67	0.72	0.92	0.89
$\{311\}_\gamma$	0.32	0.18	0.07	0.10
$\{222\}_\gamma$	0.31	0.18	0.07	NA
$\{220\}_{\alpha_b}$	0.59	0.67	0.82	0.81

Table 3.7: Variation of texture parameter of reflection lines of the alloy Sp9c transformed at 200°C with strain.

3.8 Microstructural Evolution

3.8.1 Phase Fractions

Since the austenite is partly responsible for the enhanced mechanical properties, its volume fraction was quantified as a function of plastic deformation.

As previously mentioned, preliminary data revealed errors in peak relative intensities. The volume fraction of austenite in strained samples was therefore estimated using the Rietveld method combined with the preferred orientation correction. For comparison, the method proposed by Dickson was also used [150].

According to Dickson, phase fractions of a multi-phase system could be calculated making use of the following relationship [150]:

$$\frac{V_\gamma}{V_{\alpha_b}} = \frac{\frac{1}{n_\gamma}\sum_0^{n_\gamma}(I_\gamma/R_\gamma)}{\frac{1}{n_{\alpha_b}}\sum_0^{n_{\alpha_b}}(I_{\alpha_b}/R_{\alpha_b})} \tag{3.22}$$

It is apparent that a stronger reflection from a preferentially oriented line will lead to erroneous results. For example, one may calculate volume fractions of γ and α_b using the first doublet, *i.e.* $\{111\}_\gamma$ and $\{110\}_{\alpha_b}$. However, in case of heavily deformed specimens, as presented in tables 3.5, 3.6 and 3.7, this will clearly lead to under-estimation of the austenite content. Dickson suggested that using higher order austenite and ferrite reflection lines is unnecessary in the analysis.

Dickson's method offers good statistics if the number of Bragg reflections provided for analysis is sufficiently large and representative of the microstructure and captures all major components of the texture, if present.

On the other hand, a crucial difference between Rietveld and Dickson's methods is that the former deals with preferred orientation mathematically through modelling the pole-density profile. The algorithm by which the phases in a multi-phase structure are quantified can be consulted elsewhere [151].

Experimental Findings

Figure 3.18 represents the evolution of the austenite phase as a function of engineering strain in steel Sp9c transformed at 200, 250 and 300°C using Dickson's and Rietveld methods. Note that the error bars of the data calculated using Dickson's method are too small to be visible.

Within experimental error, it is surprising that both methods yield comparable results, although Dickson's method resulted in a higher austenite volume fraction at fracture for all transformation temperatures.

Figure 3.19 presents the retained austenite volume fraction in alloy Sp10c subsequent to the completion of bainite transformation. With the exception of the values obtained at 300°C, the agreement between Dickson's and Rietveld methods is evident.

Figure 3.19 clearly shows the higher volume fraction of bainitic ferrite obtained when transformation temperature is lowered. Nevertheless, when transformation took place at 200°C, there seem to be no significant change in phase fractions, presumably due to the fact that transformation kinetics are indeed slower at lower temperatures.

Dickson's and the Rietveld methods were applied to the diffraction patterns presented in figure 3.17. Since they represent the same sample, identical phase fractions should be obtained. Results are presented in figure 3.20. As shown, the estimation of V_γ using Rietveld method led to more close values compared with the case when Dickson's method was applied.

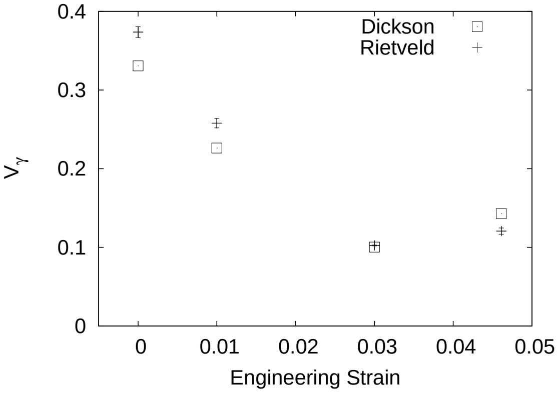

(a) Sp9c transformed at 200°C

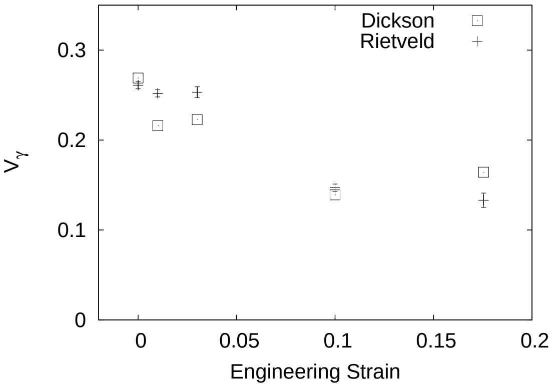

(b) Sp9c transformed at 250°C

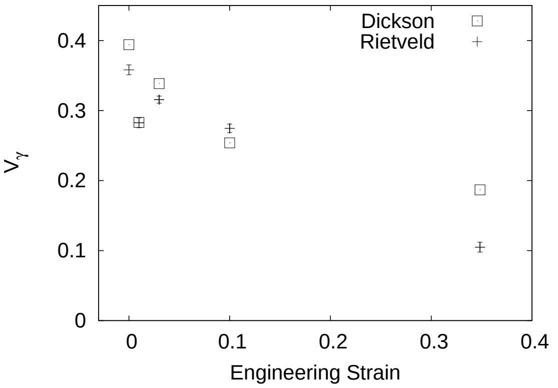

(c) Sp9c transformed at 300°C

Figure 3.18: Evolution of the volume fraction of retained austenite V_γ with strain in steel Sp9c.

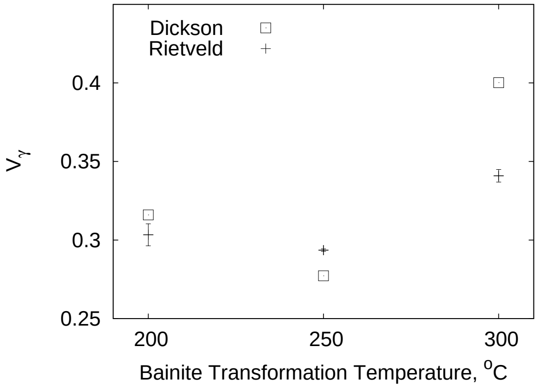

Figure 3.19: Volume fraction of retained austenite in alloy Sp10c transformed at different temperatures. No deformation was applied.

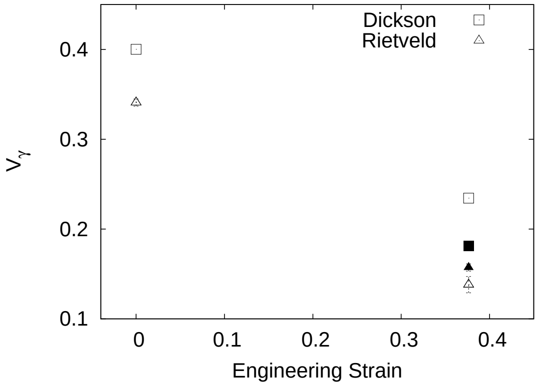

Figure 3.20: Volume fraction of the retained austenite in Sp10c bainitic structure transformed at 300°C *vs* strain. Solid data points represent austenite volume fraction estimated using a specimen cut parallel to the sample axis.

3.9 Stacking Faults

Peak shifts in X-ray diffraction patterns may arise as a result of systematic and random errors, compositional changes, residual stresses and stacking faults formed within the austenite phase. Nevertheless, it is well-known that the deformation of low-stacking fault energy phases such as the high-carbon austenite in steels leads to a high density of stacking faults [136]. Given the high-carbon concentration in the steels studied in the present work, such relative austenite peak shifts was expected.

Warren has developed a method by which, the probability of deformation-fault formation between two FCC (face-centred cubic) crystal layers can be calculated. The method makes use of the observed angular peak shifts in a diffraction doublet, namely $\{111\}_\gamma$ and $\{200\}_\gamma$, with deformation [152].

It follows that:

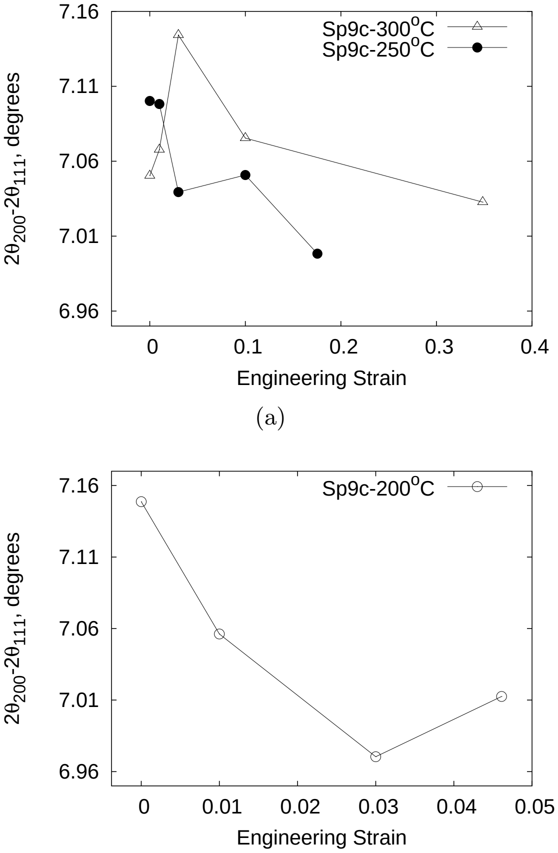

(a)

(b)

Figure 3.21: $\{111\}_\gamma$ and $\{200\}_\gamma$ doublet shifts as a function of strain.

$$\Delta(2\theta_{200} - 2\theta_{111}) = \frac{-90\sqrt{3}\alpha_p}{\pi^2}\left(\frac{\tan\theta_{200}}{2} + \frac{\tan\theta_{111}}{4}\right) \tag{3.23}$$

where α_p is the probability of stacking fault formation on $\{111\}_\gamma$ planes.

As shown in figure 3.21, angular shifts between $\{111\}_\gamma$ and $\{200\}_\gamma$ Bragg reflections were observed. It is apparent that the separation between the two

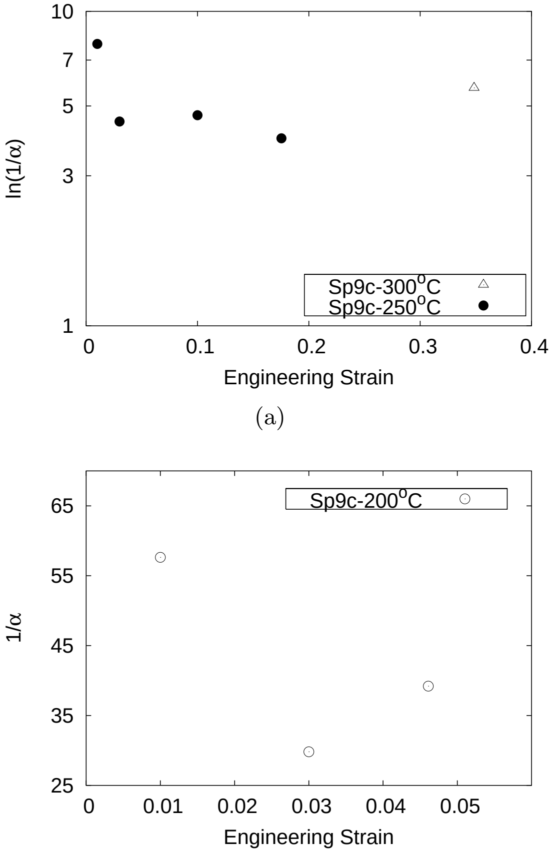

(a)

(b)

Figure 3.22: The average number of FCC-crystal atom layers ($1/\alpha_p$) between stacking faults estimated as a function of strain.

reflection lines decreased with deformation and it is systematic in the sense it decreases more with further straining. Figure 3.21 clearly shows these systematic shifts. However, only in alloy Sp9c transformed at 300°C the separation between the $\{111\}_\gamma$ and $\{200\}_\gamma$ doublet tended to increase initially. After further deformation, namely at 0.03 strain, the doublet started to move towards each other.

Figure 3.22 represents the estimated $1/\alpha_p$ value for the austenite in steel Sp9c at different strain levels. It is clear from figure 3.22(a) that, plastic deformation has increased the probability of stacking fault formation. Figure 3.22(b) shows that in alloy Sp9c transformed at 200°C, when strain was increased from 0.01 to 0.03, the number of $\{111\}_\gamma$ layers between two stacking faults in austenite crystal decreased from 58 to 30. The data point at fracture strain might be caused by experimental error. A further TEM examination could confirm the formation of deformation faults in the austenite.

3.10 Summary

The use of X-ray diffractometry has enabled a detailed characterisation of the steels investigated. Similar reports in the literature are almost absent, especially regarding fully bainitic steels. The following points may be summarised:

1. It was observed that a finer structure is obtained as the bainite transformation temperature is lowered.
2. By transforming at lower temperatures, the dislocation density in bainite increases. This was manifested in a lesser degree of carbon-enrichment in the austenite.
3. Texture and lattice distortions were observed in heavily deformed steels. This, unless taken into account, may lead to an erroneous assessment of phase fractions and, in the case at hand, their carbon contents.
4. Tempering at 300°C for 2 h caused carbon partitioning from the bainite to the retained austenite. No clear evidence was observed which might suggest crystal relaxation.
5. It has been demonstrated that stacking faults are induced in the austenite as a result of plastic deformation.

Chapter 4

Mechanical Properties

4.1 Introduction

The objective of the work presented here is to characterise the mechanical behaviour of the novel carbide-free bainitic steels. An interesting development has been the adoption of a strain-aging process. Steel performance is compared with published data from other types of steels.

4.2 Overview

Earlier work on carbide-free bainitic steels demonstrated promising combinations of strength and toughness [15, 20, 91, 92, 96, 97, 106, 107]. The observed enhanced properties were ascribed to the carbide-free microstructure which featured fine platelets of bainitic ferrite distributed in a finely-divided, carbon-enriched austenite matrix. Continuous yielding and a high work-hardening rate during tensile testing are characteristics of this microstructure. The reasonably stable retained austenite transforms in a progressive manner into martensite upon deformation. Since the transformation is accompanied by a shape and volume change, dislocations are generated and inherited by the ferrite [153], leading to strengthening and work-hardening, thereby delaying necking [61].

Table 4.1 shows preliminary results where, for example, the Sp10c sample transformed at 300°C exhibited total elongation of 37.6 % for a yield strength of 1130 MPa. On the other hand, there is a decrease in ductility as strength increases, particularly for samples transformed at lower temperatures.

Steel	Bainite transformation (°C)	YS MPa	TS MPa	UE %	TE %	YR
Sp9c	200	1193	2183	4.6	4.6	0.55
Sp9c	300	1030	1729	29.8	34.8	0.6
Sp10c	300	1130	1675	27.4	37.6	0.67
Sp11c	250	1620	2078	5.1	16	0.78

Table 4.1: Tensile properties at room temperature. The cross-head speed was 0.01 mm min^{-1}. The elongation is for a gauge length of 10 mm. YS is the yield strength (0.2% proof strength); TS the tensile strength; UE the uniform elongation; TE the total elongation and YR the yield ratio which is YS/TS.

The yield ratio, a lower value of which may result in better fatigue resistance, was the lowest for the steel transformed at 200°C with a value of 0.55. Sp9c and Sp10c transformed at 300°C exhibited similar mechanical behaviour given the similarities in chemical composition.

The objective of the work presented here was to enhance the mechanical properties further.

According to the data in table 3.4, the retained austenite was not further enriched in carbon as the transformation temperature is lowered to 200°C. This observation is because of carbon trapping in bainitic ferrite [102]. It would therefore be interesting to see how the microstructure and properties respond to low-temperature strain-aging treatments.

4.3 Experimental Procedures

Uniaxial tension tests on 5 mm diameter and 25 mm gauge length specimens were carried out at room temperature with a cross-head speed of 0.01 mm min^{-1} corresponding to a strain rate of 6.66×10^{-6} s^{-1}. Strain-aged samples were pre-strained to 2.5, 5 and 10% engineering strain followed by tempering at 300°C for 2 h. In some cases the samples were first tempered at 300°C for 2 h followed by straining.

The stress-strain curves were recorded during pre-straining, permitting changes in the yield strength to be monitored on the same sample before and after the strain-aging process.

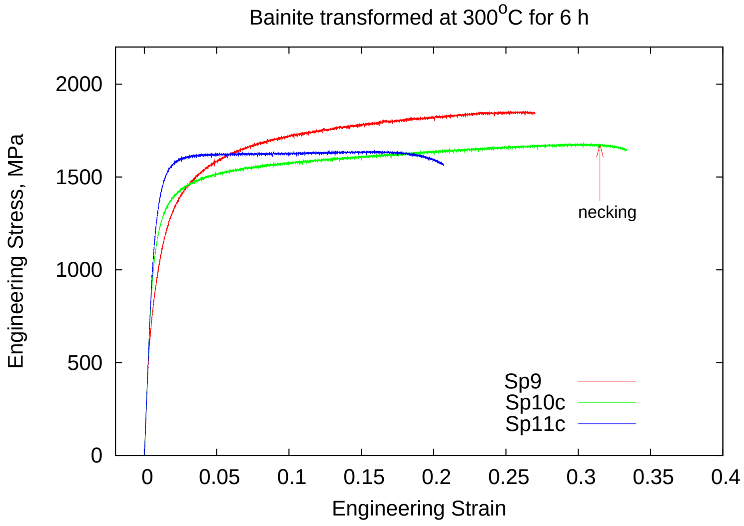

Figure 4.1: Engineering stress-strain curves of as-transformed samples.

Sample	YS MPa	TS MPa	UE %	TE %	YR	$V_{\gamma 0}$
Sp9	800	1853	26.3	27	0.43	0.39
Sp10c	1110	1680	30.3	33.4	0.66	0.4
Sp11c	1283	1641	15.4	20.7	0.78	0.28

Table 4.2: Properties of steels presented in figure 4.1.

4.4 Mechanical Behaviour

4.4.1 As-transformed Structures

Structures Transformed at 300°C

Figure 4.1 shows tensile curves for samples transformed at 300°C for 6 h. Almost all the large elongations observed were uniform with only a minor tendency to neck in Sp10c and Sp11c just before fracture (figure 4.2).

Strain-hardening was assessed by determining the incremental hardening exponent n_{incr} [154]:

$$\mathrm{n}_{incr} = \frac{d\ln\sigma_t}{d\ln\varepsilon_t} \tag{4.1}$$

where σ_t is the true stress and ε_t the true strain.

Figure 4.2: Samples corresponding to the tensile curves presented in figure 4.1 fractured in uniaxial tension.

The work-hardening behaviour of the samples shown in figure 4.1 is presented in figure 4.3. Although sample Sp11c exhibited the highest yield strength (table 4.2), the work-hardening rate in the early stages of deformation was the lowest. Therefore, it is anticipated that the increase in the YS of steel Sp11c is a result of the higher bainite volume fraction. The work-hardening rate of sample Sp9 was the highest in early stages of tensile deformation (figure 4.3), presumably resulting in a greater TS compared with Sp10c given the similar $V_{\gamma 0}$. It is possible that this is because the retained austenite in Sp9 is less stable to strain-induced martensitic transformation. Using a published austenite mechanical stability model [155], the driving force for martensite transformation $\Delta G^{\alpha' \gamma}$ in steels Sp9, Sp10c and Sp11c was calculated and found to be 1210, 1430 and 2008 J mol^{-1} respectively. This explains the better elongation exhibited by steel Sp10c when compared with Sp9. In this context, the ductility of steel Sp11c could have been the best given its austenite chemical stability, only at constant $V_{\gamma 0}$.

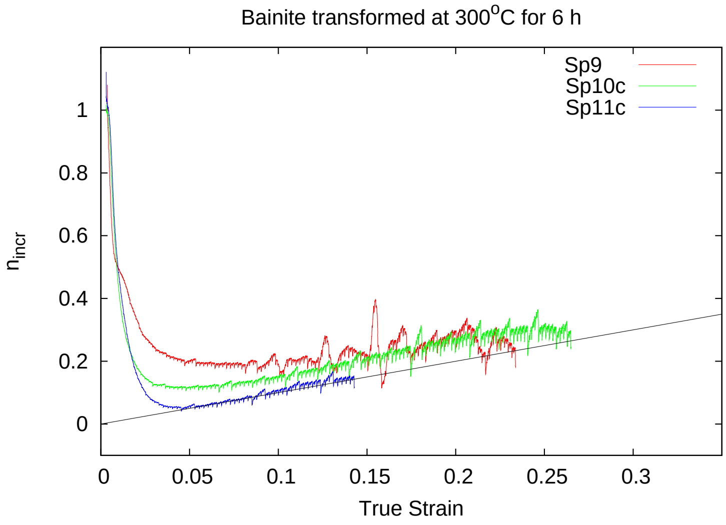

Figure 4.3: n_{incr} *vs* true strain curves of the as-transformed samples shown in figure 4.1. The straight line represents the instability criterion where uniform true strain is equivalent to n_{incr}.

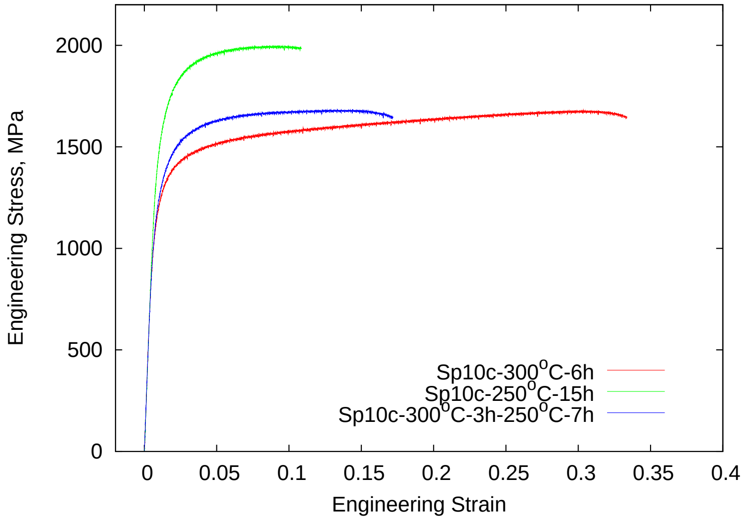

Figure 4.4: Engineering stress-strain curves of Sp10c steels transformed into bainite at different temperatures.

Stepped Transformation

Transformation was is some cases conducted in two steps, at 300°C for 3 h followed by treatment at 250°C for 7 h. The retained austenite content was found to be similar to when the steel was transformed at 300°C for 6 h with volume fractions 0.37 and 0.4 respectively. Transformation solely at 250°C resulted in a lower fraction of 0.28. Nevertheless, the carbon content in the retained austenite after the 2-step transformation process was relatively high, see table 4.3.

Figure 4.4 compares the tensile properties due to the different heat-treatments. The stepped heat-treatment results in intermediate properties, both in terms of the proof strength and total elongation (table 4.3). However, if the strength-ductility balance is considered, the steel transformed at 300°C for 6 h outperforms the step-transformed steel.

Clearly the 300/250°C sample exhibited inferior elongation. The result is surprising because the austenite in the doubly heat-treated sample has a greater concentration of carbon than for the 300°C sample. It is expected that the stepped steel would possess finer bainitic ferrite laths containing

Transformation temperature (°C)	YS MPa	TS MPa	UE %	TE %	YR	V_{α_b}	V_γ	C_γ wt%
300	1110	1680	30.3	33.4	0.66	0.6	0.4	1.573
250	1447	1999	8.7	10.9	0.72	0.72	0.28	1.632
300-250	1135	1686	14.4	17.2	0.67	0.63	0.37	1.667

Table 4.3: Mechanical properties of steel Sp10c transformed at different temperatures.

more defects and a greater amount of trapped carbon compared with the 300°C sample. In the as-transformed condition, X-ray results reveal bainitic ferrite crystallite sizes of 14–164 and 19–68 nm for the stepped and 300°C samples respectively.

As for the sample transformed at 250°C for 15 h, there is a significant loss in elongation at much greater strength.

As shown in figure 4.5, the stepped sample and that transformed at 250°C both experienced slightly higher strain-hardening during the early stages of deformation compared with the structure transformed at 300°C. However, the latter sample exhibited better strain-hardening at latter stages of deformation, consequently postponing the onset of necking to larger strains.

To summarise, the 2-step transformation procedure apparently did not enhance the strength compared with the 300°C specimen. The phase fractions are quite similar so it is concluded that the more ductile bainite in the sample transformed at 300°C contributed to its high elongation.

Structures Transformed at Lower Temperatures

Figures 4.6 and 4.7 show the mechanical test results for samples transformed at lower temperatures.

Firstly, higher strength levels are achieved, although at the expense of elongation.

An interesting observation is that Sp10c is more ductile compared with Sp11c which exhibited necking at an early stage of deformation (table 4.4).

Both steels Sp10c and Sp11c transformed at 250°C exhibited similar ini-

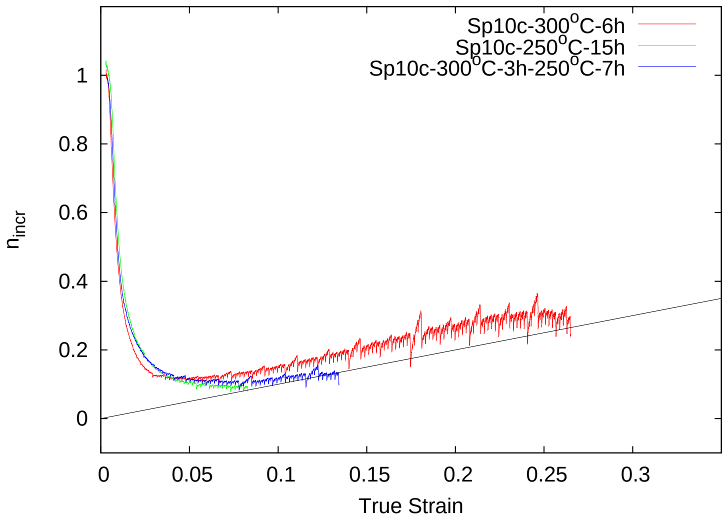

Figure 4.5: n_{incr} *vs* true strain curves of the as-transformed Sp10c samples shown in figure 4.4.

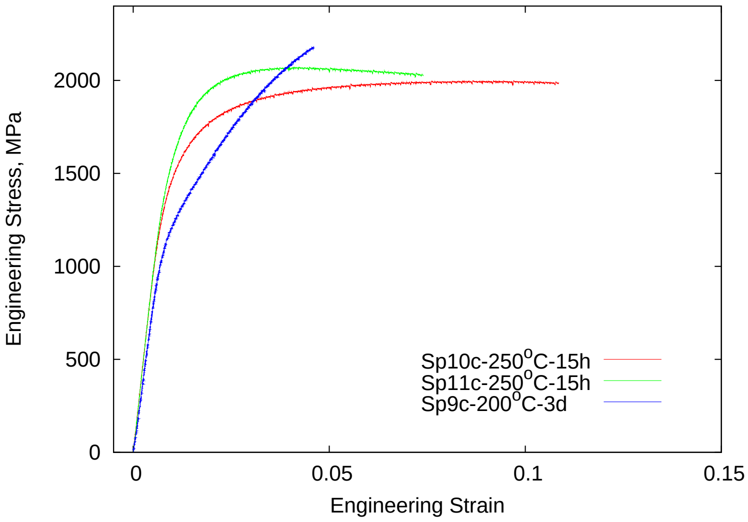

Figure 4.6: Stress-strain curves of steels transformed into bainite at relatively low temperatures.

Sample	YS MPa	TS MPa	UE %	TE %	YR	V_{α_b}	V_γ	C_γ wt%
Sp10c-250°C-15 h	1447	1999	8.7	10.9	0.72	0.72	0.28	1.632
Sp11c-250°C-15 h	1577	2072	4	7.4	0.76	–	–	–
Sp9c-200°C-3 d	1193	2183	4.6	4.6	0.55	0.67	0.33	1.001

Table 4.4: Mechanical performance of steels presented in figure 4.6.

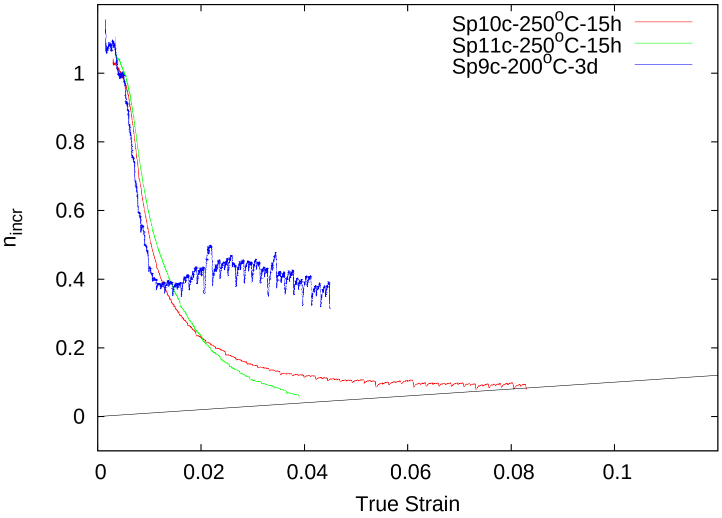

Figure 4.7: n_{incr} *vs* true strain curves of the as-transformed samples shown in figure 4.6.

tial work-hardening (figure 4.7). On the other hand, Sp9c steel transformed at 200°C although contained slightly higher austenite volume fraction, it is carbon content was remarkably low which apparently resulted in a non-progressive austenite transformation (figure 4.7).

4.4.2 Tempered Bainitic Structures

Tempering of the as-transformed steels (transformed at 300°C for 6 h and air-cooled to room temperature) was carried out at 300°C for 2 h.

As discussed earlier, tempering of Sp9c steel transformed at 250°C resulted in an increase in austenite lattice parameter, presumably due to carbon partitioning. A slight decrease in α_b lattice parameter was observed. Thermal

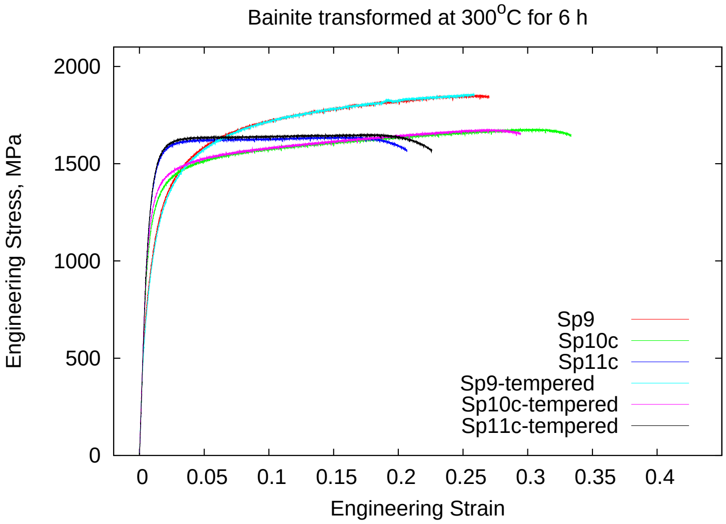

Figure 4.8: Engineering stress-strain curves of steels in the as-transformed, and transformed and tempered. Tempering was carried out at 300°C for 2 h.

signals were observed during tempering using differential scanning calorimetry[†]. It is therefore expected that tempering should have an influence on mechanical properties.

Within experimental error, it is apparent from figure 4.8 that tempering bainitic steels generated at 300°C has no major impact on tensile properties.

The proof strength of sample Sp9 has increased from 800 to 939 MPa after tempering with a consequent increase in the yield ratio from 0.43 to 0.51. No similar observations were found in Sp10c nor Sp11c steels. Figure 4.9 shows that the strain-hardening behaviour of steel Sp9 was comparable before and after tempering.

Nevertheless a series of sharp fluctuations in the n$_{incr}$ value has been observed (arrowed in figure 4.9). It is important to note that the relatively low rate of strain applied during the test combined with the high data-acquisition rate enabled recording such details. It is interesting that no local necking has been observed in the sample after fracture and therefore the observed sharp decrease in work-hardening might be ascribed to jerky

---

[†] See appendix A.

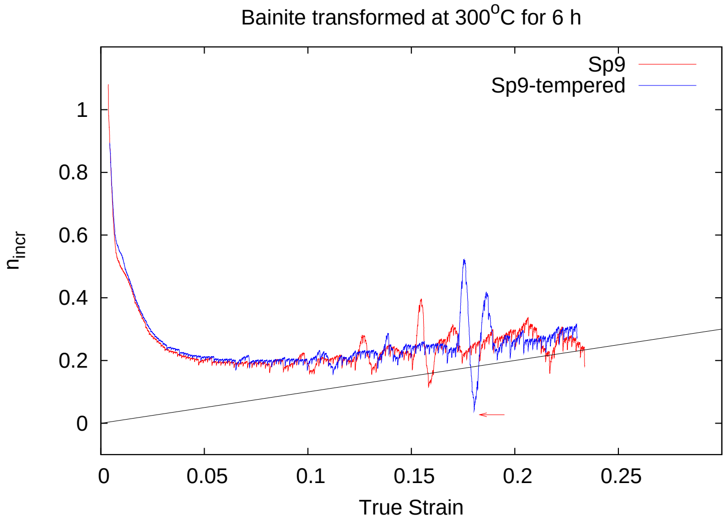

Figure 4.9: n_{incr} *vs* true strain curves of Sp9 and Sp9-tempered steels presented in figure 4.8. Arrow points to a sharp variations in n_{incr}.

transformation plasticity. Such features were largely smoothed as a result of tempering, presumably due to the greater austenite stability which yields a more progressive transformation.

4.4.3 Strain-aged Structures

Strain-aging of bainite has previously been reported by Kalish *et al.* [156, 157] and Fondekar *et al.* [158]. The process involves plastic deformation of the as-transformed bainitic structure preceded and or followed by tempering.

Kalish *et al.* used a steel of the composition 0.39C-0.25Mn-1Si-5.25Cr-1.39Mo-0.54V, austenitised at 1010°C for 30 min then transformed at 288°C for 4 h [156]. Tempering was then carried out at 288°C for 1 h. The strip was then rolled at room temperature such that the thickness was reduced by 3.5%. The steel was then re-tempered.

A huge increase in the yield strength from 827 to 1896 MPa was observed as a consequence of the thermomechanical processing. However, at that strength level, the elongation dropped from 12 to 5%. Tensile strength was found to slightly increase from 1896 to 1965 MPa.

Due to transformation, about half of the retained austenite content (33→16%)

decomposed at 2% plastic strain in uniaxial tension [156], indicating considerable austenite instability. For comparison, Sp9c transformed at 250°C for 15 h and tempered at 300°C for 2 h, lost half of the retained austenite from 26 to 13% when 10% strain was applied. As such, the ductility of strain-aged steels would be a concern.

Apparently, there is no current research regarding the development of modern bainitic steels with the strain-aging process implemented.

Strain-aging of the as-transformed structures involved straining in uniaxial tension ($\varepsilon \leq 0.1$) then tempering. In some cases, tempering prior to deformation was also applied. Tempering was conducted at 300°C for 2 h.

Performance of Steel Sp9 Transformed at 300°C

The elongation decreases following strain-tempering (figure 4.10), probably because of the reduction in retained austenite content. It is interesting that for the sample strained $\varepsilon = 0.05$, the ductility 'recovered' considerably following tempering suggesting that austenite fraction is not the only controlling parameter. The improvement in elongation was also accompanied by an increase in proof strength of about 100 MPa (table 4.5). Similarly, proof strength was greater in case of tempering alone, and also in the case where it was followed by strain-aging. Note that in both cases the tensile strength was almost unaffected.

The better elongation achieved following strain-tempering may relate to a greater mechanical stability of the austenite. For example, steel Sp9c transformed at 250°C and strained to 0.1 ε exhibited an increase in austenite lattice parameter from 0.36247±0.00006 to 0.36282±0.00003 nm upon tempering. The bainitic-ferrite lattice parameter was found to decrease from 0.2868±0.00002 to 0.28673±0.00002 nm, indicating carbon partitioning from α_b to γ. Lattice relaxation is believed to be unlikely given the low temperature at which tempering was carried out. Another contribution might arise from the bainitic ferrite recovery. In the above steel, the α_b lattice microstrain decreased from 0.016–0.0241 to 0.0135–0.0204 upon tempering.

The tempered strain-induced martensite may have also contributed to the enhanced ductility. On the other hand, for the tempered-strain-aged sam-

Process	YS (before deformation) MPa	YS MPa	TS MPa	UE %	TE %
0.05ε	733	1681	1872	12.7	13.2
0.05ε-t	731	1789	1866	20.6	23.6
t-0.05ε-t	825	1851	1881	16.4	20.2
0.1ε-t	740	1999	2047	1.6	5.8

Table 4.5: Mechanical properties of Sp9 transformed at 300°C for 6 h. 't' stands for tempering.

ple, elongation was less than that of the strain-aged sample. It is speculated that this might be due to a lower austenite fraction, however, this requires further experimental confirmation.

As shown in figure 4.10(a), as the degree of pre-strain is increased, although elongation decreases the strength increases.

Table 4.5 shows that the best strength-ductility balance is achieved in the 0.05 strained and tempered sample. Therefore, it was possible to increase the proof strength from 731 to 1789 MPa without considerable loss in ductility.

As shown in figure 4.10(b), the stress-strain curves of the strain-aged samples was not smooth, exhibiting a sequence of local necking events (shown in figure 4.12).

Figure 4.11 shows the strain-hardening data. As shown in figure 4.11(a), the as-transformed sample is characterised by a plateau of n_{incr} at about 0.2. Upon further straining, the structure is continuously, however slightly, hardened presumably *via* martensitic transformation up to the onset of necking. On the other hand, the pre-strain sample exhibited a different behaviour. Clearly strain-hardening lagged behind that of the as-transformed sample.

Comparison with Sp10c and Sp11c

Comparative data are presented in table 4.6. For same processing route, Sp10c is weaker than Sp9 and Sp11c, however, Sp10c exhibited the best elongation. It is remarkable the poor ductility exhibited by steel Sp11c after strain-tempering. As previously presented in table 4.2, steel Sp11c in the as-transformed condition possessed a relatively lower austenite volume fraction when compared with Sp10c for instance. Therefore, it is anticipated that

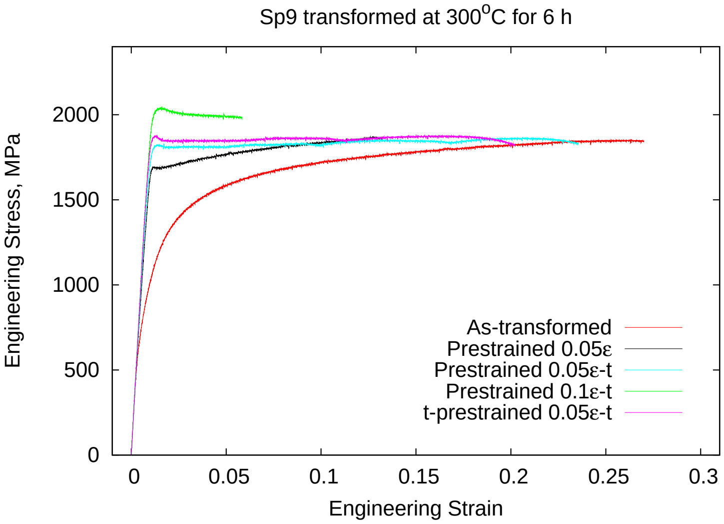

(a)

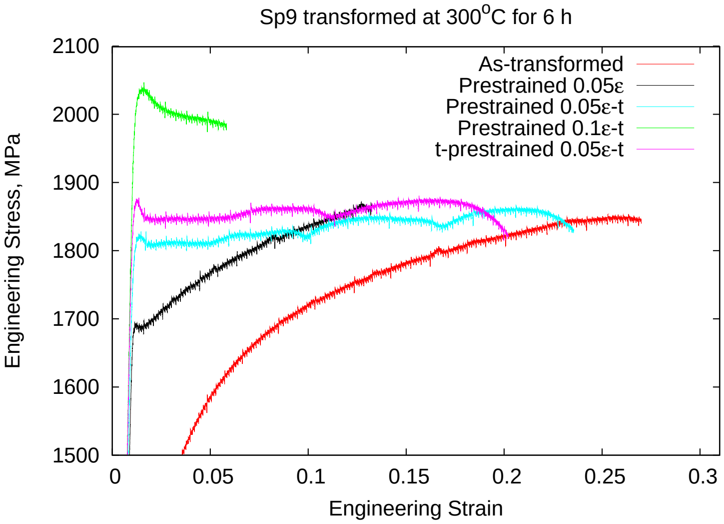

(b)

Figure 4.10: Stress-strain curves of steel Sp9 for various processing routes. (b) Shows the features following strain-aging.

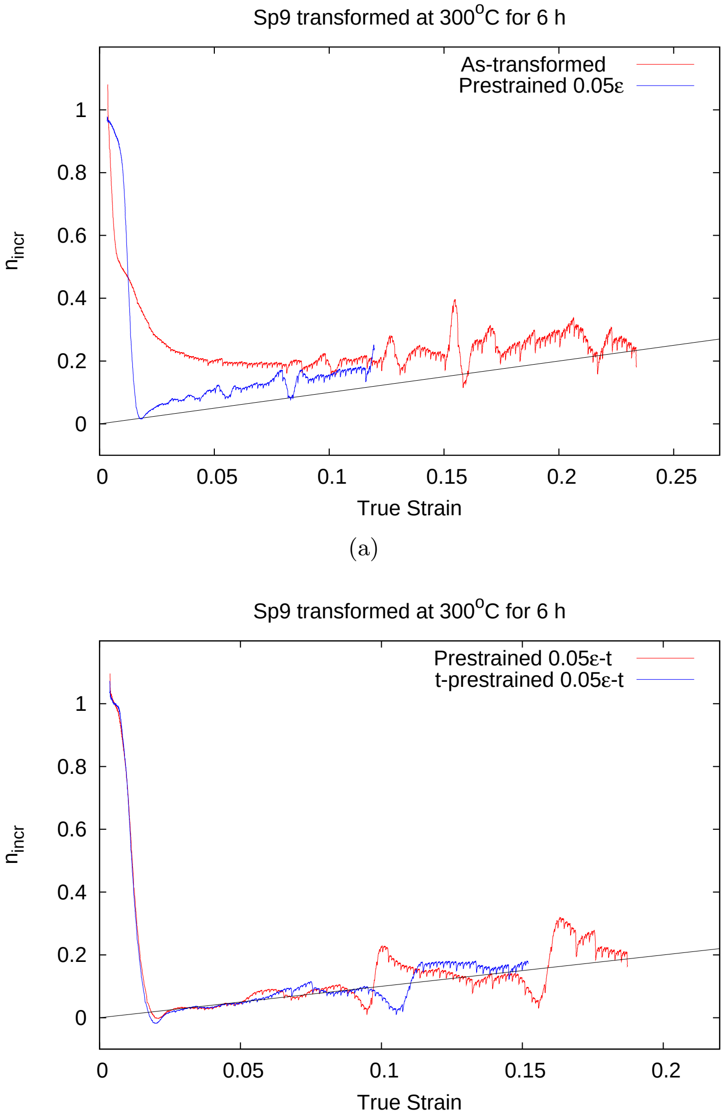

(a)

(b)

Figure 4.11: n$_{incr}$ *vs* true strain curves of the steel presented in figure 4.10.

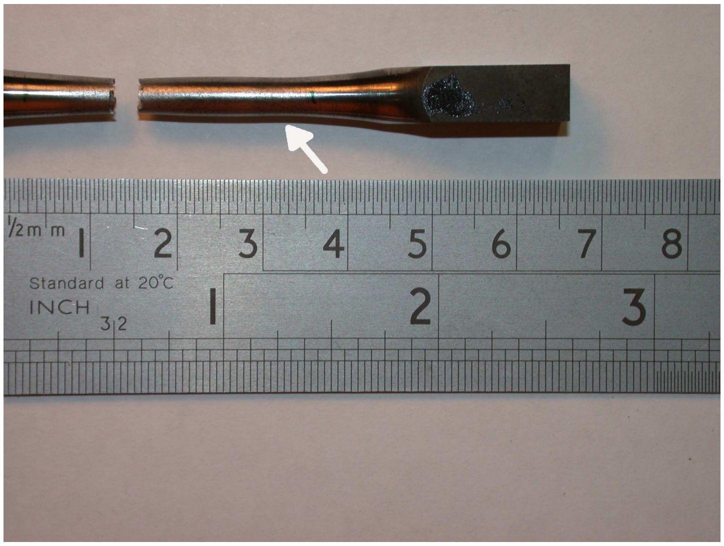

(a) Sample Sp9 transformed at 300°C then strain-aged. Mechanical behaviour is shown in (b). Arrow points to a 'local' neck.

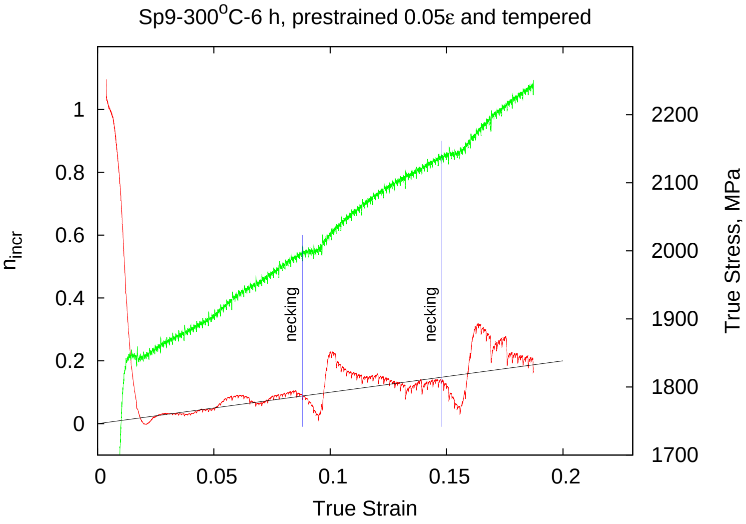

(b)

Figure 4.12: The mechanical performance of the sample shown in (a) during uniaxial tension.

this could be an explanation for the very low elongation obtained following the strain-tempering process.

The work-hardening behaviour is shown in figure 4.13.

Sample	Strain level	YS (MPa)	UE (%)	YR
Sp9	0.05	1789	20.6	0.96
Sp10c	0.05	1717	23.1	0.97
Sp10c	0.026	1660	26.4	0.98
Sp11c	0.023	1736	1.2	0.99

Table 4.6: Mechanical behaviour of different steels transformed at 300°C for 6 h then strain-tempered.

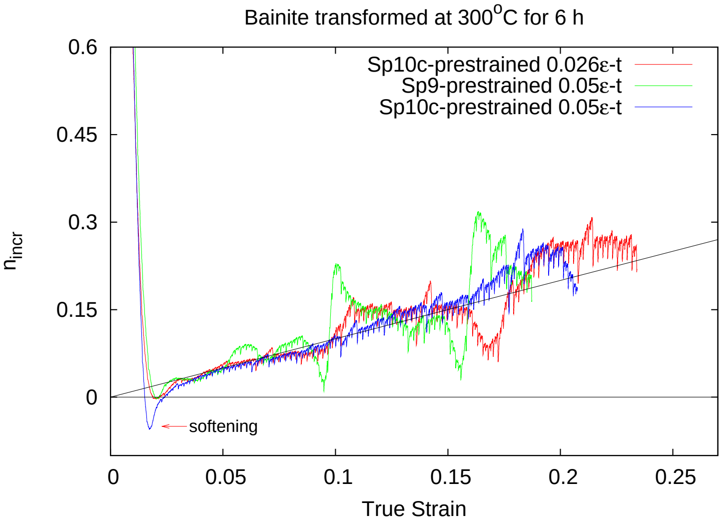

Figure 4.13: Variations in n_{incr} with true strain of structures transformed at 300°C then strain-aged. Arrow points to a softening behaviour.

Steels Transformed at Lower Temperatures

As shown in figure 4.14(a), the structure of Sp9 steel strain-aged by applying 0.025 strain and tempering following transformation at 250°C showed yield strength of 2121 MPa. Same material transformed at 300°C, pre-strained with double the strain level and tempered yielded only 1789 MPa YS. The loss of uniform elongation was also evident, decreasing from 20.6 in the latter to 3.1 % in the former.

Figure 4.14(a) shows proof strength levels obtained in steels Sp10c and Sp11c similar to that obtained in the strain-aged Sp9 steel. Nevertheless, the stress-strain curves of the former alloys, although they underwent similar processing, were remarkably different. The curves for Sp10c and Sp11c samples in the as-transformed condition are shown for comparison.

As shown in figure 4.14(b), due to the very small uniform elongation obtained in steels Sp10c and Sp11c, strain-tempered, the work-hardening behaviour could not be distinguished from that observed in the alloy Sp9. However, it is postulated that the lack of sufficient work-hardening in the former steels to be responsible for the premature failure.

To summarise, as far as the strength-ductility balance is concerned, it is apparent that the strain-aging process was beneficial especially in steels transformed at 300°C. Applying the strain-aging process on steels transformed at 250°C resulted mainly in an increase in proof strength on the expense of ductility. Nevertheless, the large yield strength values obtained (above 2 GPa) in that type of low-alloy steel are remarkable. For industrial applications where the focus is on providing a material with exceptional strength, applying strain-aging on steels transformed at lower temperatures, *i.e.* 250°C for example, would be beneficial and sufficient to provide materials with YS well above 2 GPa. In that sense, the use of steel Sp11c would be an advantage.

Figure 4.15 exhibits an overall summary of the mechanical performance of the studied steels as a result of applying different processing routes. In particular, the illustration demonstrates the advantage of the strain-aging process in terms of achieving higher yield strength without scarifying ductility.

4.4.4 Comparison with Other Steel Classes

It was believed beneficial to hold a comparison in terms of mechanical performance between steel systems developed in the present work with those currently under development by many research groups. In particular, steel data of a newly developed process, quenching and partitioning (Q&P) de-

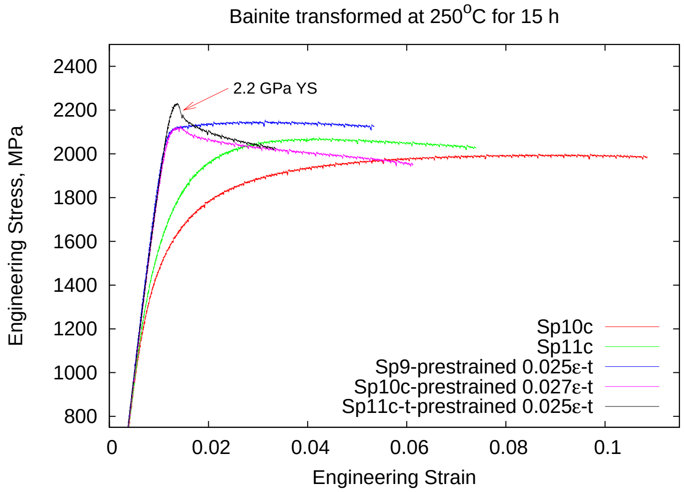

(a) Stress-strain curves of strain-aged and unprocessed steels transformed at 250°C. Arrow points to a sample where yield strength over 2.2 GPa was recorded

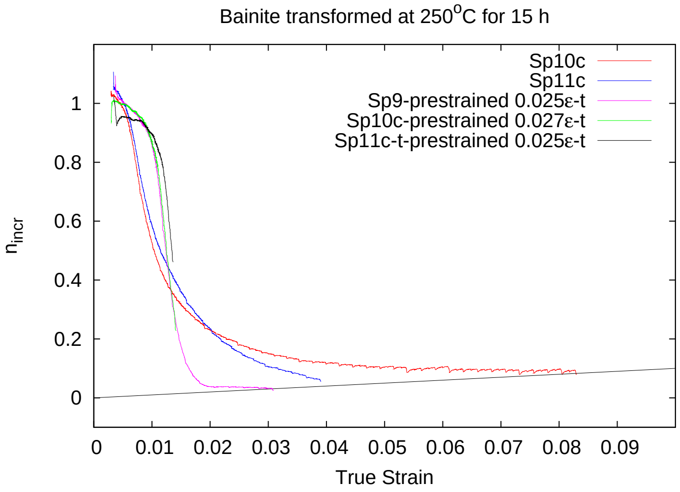

(b) Strain-hardening behaviour

Figure 4.14: Mechanical performance of bainitic steels under various processing conditions.

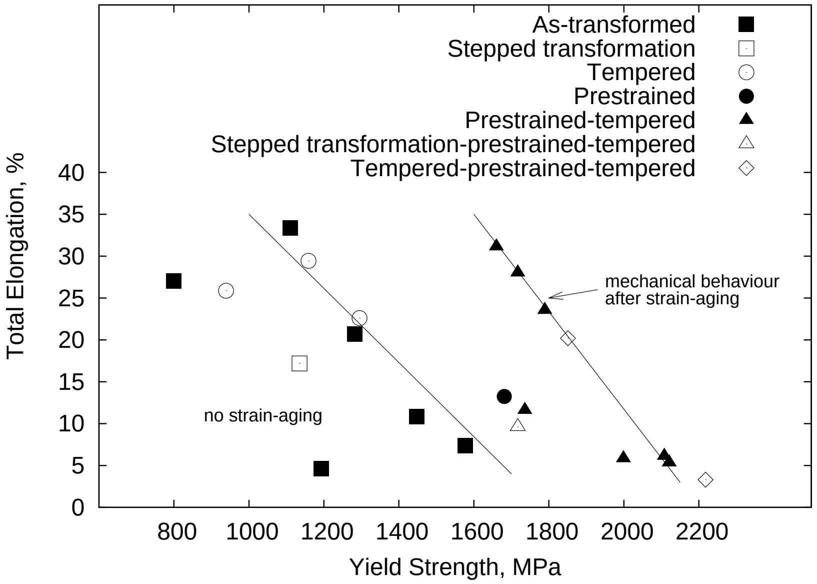

Figure 4.15: A plot demonstrates the advantage of applying the strain-aging process on current steels in terms of mechanical performance.

veloped by Speer and co-workers is included [9, 10].

Figure 4.16 clearly demonstrates the potential of the steels developed in the present work with a superior combination of strength and ductility.

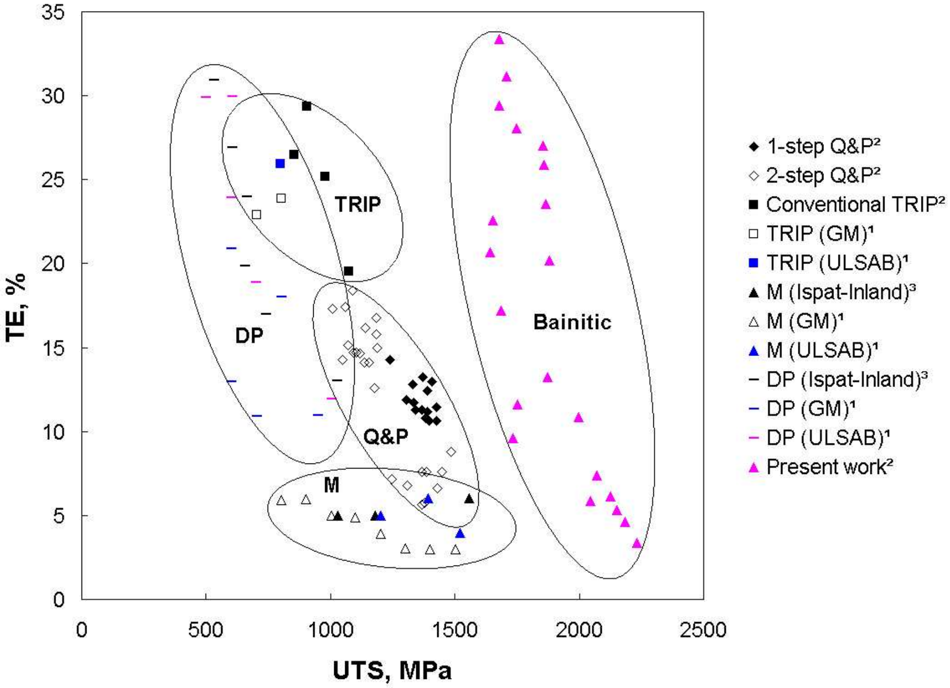

Figure 4.16: A comparison between steels developed in the present work with those types reported in the literature. Except for bainitic steel data, data regarding other steel types were collected from the work of Speer *et al.* [10]. '1' denotes 80 mm gauge length; '2' approximately 25 mm gauge length and '3' unspecified gauge length.

4.5 Summary

The mechanical behaviour of the bainitic steels studied here, both in the as-transformed and strain-aged condition, have been characterised. The effect of tempering of the as-transformed steels on mechanical performance was also presented. The steels exhibited excellent combinations of strength and ductility owing to the novel carbide-free nanostructure and the stable retained austenite.

Mechanical properties have been improved further through the adoption of the strain-aging process. With the exception of the Sp11c steel, when strain-aging process is applied to bainitic structures transformed at 300°C, the yield strength surpassed that exhibited by steels transformed at low temperatures such as 200°C. The former steels also showed far superior uniform elongation than the latter. This is an important achievement since the total processing time would be greatly reduced given the period needed to transform bainite at very low temperatures.

Chapter 5

Study of The Mechanical Behaviour Using *in situ* Neutron Diffraction

5.1 Introduction

As already described, microstructural changes and martensitic transformation take place during the deformation of bainitic steels containing retained austenite. These changes are directly responsible for the observed macroscopic mechanical behaviour and can in principle be followed during the course of deformation, using neutron diffraction.

5.2 Experimental Procedures

The use of neutrons yields better counting statistics since the considerable penetration power enables a greater volume of material to be assessed. The strain measurement instrument ENGIN-X at the ISIS neutron spallation source was used in the current investigation. Cylindrical samples of 5 mm diameter were deformed in uniaxial tension whilst subjected to a neutron beam. Diffraction spectra were recorded as the applied load was stepped up.

After macroscopic yielding, a position-control mode was implemented during continued deformation. The loading axis was aligned at 45° to the incident neutron-beam, as shown in figure 5.1.

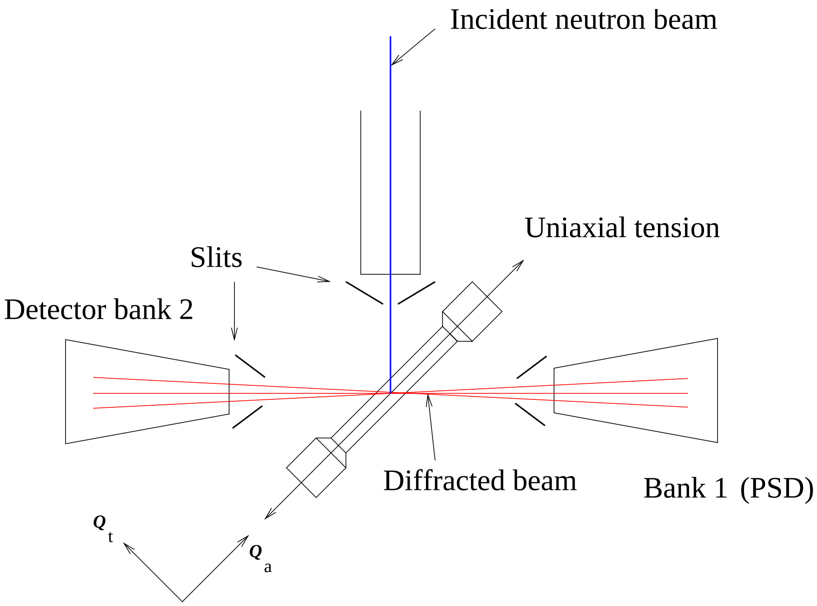

Figure 5.1: Geometric arrangement for *in situ* measurements in uniaxial tension using neutron diffraction. Q_a and Q_t denote the parallel and transverse scattering vectors respectively.

Two position sensitive detectors (PSD) were used to record time-resolved diffraction patterns at fixed scattering angles ±90° to the incident beam. Diffraction spectra were therefore acquired both parallel and transverse to the load axis.

The technique provides a *volume average* elastic strain measurement of aggregates of grains with identical orientation.

The primary objective of the work present in this chapter was to study the potential influence of the strain-aging process on microstructure and consequently mechanical behaviour. As has been outlined in Chapter 3, preferred orientation was observed to evolve as plastic deformation proceeded. As shown in figure 5.1, the use of *in situ* neutron diffraction instrument equipped with 2 PSDs in the shown arrangement allowed further investigation of this point.

A neutron spallation source provides pulses of neutrons with a continuous spectrum of wavelengths. The wavelength of a detected neutron is determined by the *time-of-flight* (t) from the moderator to the detector [159]:

$$\lambda = ht/m_n L_n \tag{5.1}$$

where h is Planck's constant, t is the time-of-flight, m_n is the neutron rest-mass and L_n is the neutron flight-path.

Three fully bainitic samples were investigated from alloy Sp10c. Sample S1 was transformed into bainite at 300°C for 6 h, and then subjected to uniaxial tension at room temperature to 2.5% engineering strain, with a cross-head speed of 0.1 mm min^{-1}. The sample was subsequent tempered at 300°C for 2 h.

For comparison, sample S2 was transformed at 300°C for 6 h without implementing the strain-tempering process.

Sample S3 was a tempered microstructure where bainite transformation was carried out at 200°C for 3 d followed by tempering at 300°C for 2 h. During the course of the experiments, samples S1 and S2 were deformed to the failure point whereas S3 was loaded beyond yield and then unloaded due to beam failure. Nevertheless, sample S3 was not expected to withstand large plastic strains (Chapter 4).

A single peak fitting approach was used in the data analysis by which peak position and intensity could be determined.

5.3 Preferential Transformation and Evolution of Texture

The macroscopic mechanical behaviour of the three samples is shown in figure 5.2.

Figure 5.3 shows axial and transverse spectra of S1 at zero-load and just before fracture. Figure 5.3(a) represents the axial diffraction spectrum at zero-load and at 0.126 ε.

Given the high degree of deformation, it is evident that the $\{220\}_\gamma$ reflection has completely disappeared whereas $\{200\}_\gamma$ and $\{311\}_\gamma$ are barely visible. $\{111\}_\gamma$ was considerably weakened. This is associated with the formation of strain-induced martensite. The austenite grains transform into martensite in a preferential manner depending on crystallographic orienta-

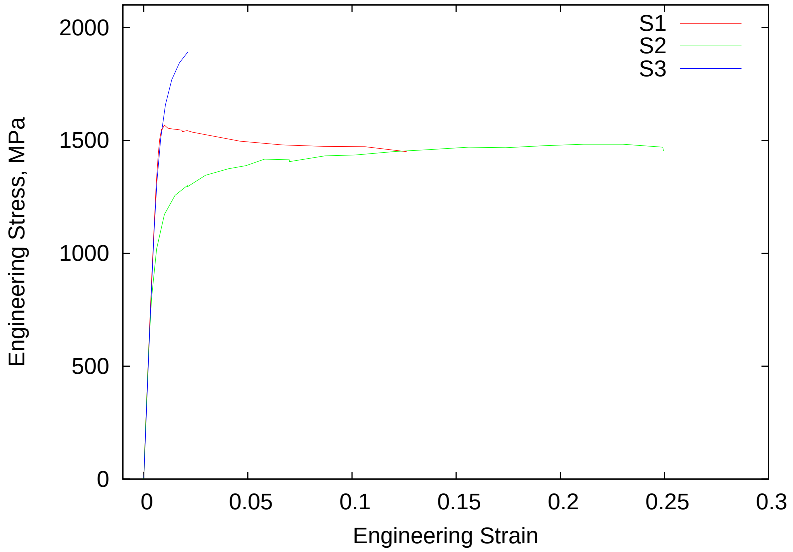

Figure 5.2: Macroscopic engineering stress-engineering strain curves acquired during diffraction. Note that the mechanical behaviour confirms that previously reported in Chapter 4.

tion. Therefore, there can be specific austenite reflections which are more sensitive to plastic deformation in the sense that their respective grains are more prone to martensite transformation [160]. It is believed that martensite peaks overlap with those from bainitic ferrite, for example, $\{110\}_{\alpha'}$ and $\{101\}_{\alpha'}$ with $\{110\}_{\alpha_b}$ reflection. Given the fineness of the structure (Chapter 3), peak broadening is expected which further makes resolution of martensite peaks difficult.

The transverse diffraction pattern shown in figure 5.3(b) is similar to that recorded by bank 1 in the zero-load condition. Upon deformation, however, the $\{111\}_\gamma$ reflection line was weaker than that exhibited by the axial diffraction pattern. Also, $\{220\}_\gamma$ did not disappear as a result of deformation compared with the case in the axial diffraction pattern.

In figure 5.3(a), the $\{211\}_{\alpha_b}$ and $\{200\}_{\alpha_b}$ reflections decreased in intensity as a result of deformation, whereas it was found that their intensity even enhanced in the transverse spectrum (figure 5.3(b)). This indicates a degree of grain rotation due to applied plastic strain, although a contribution

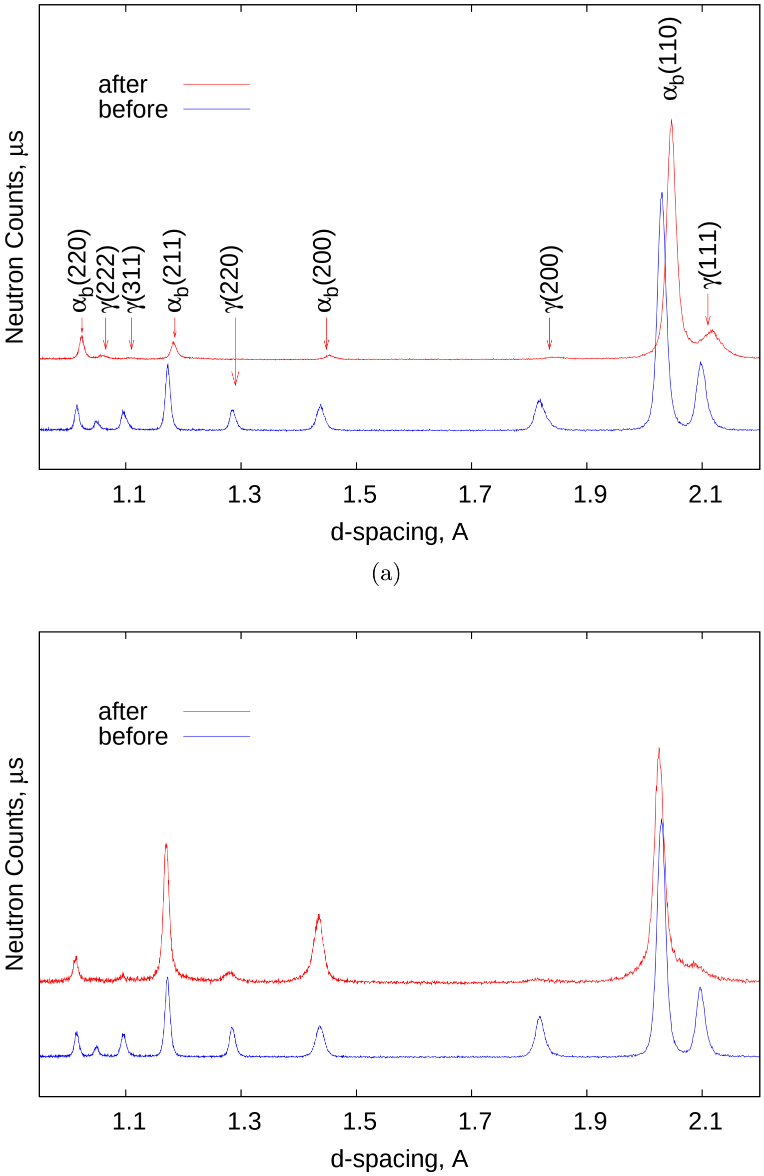

(a)

(b)

Figure 5.3: Axial (a) and transverse (b) diffraction spectra recorded for S1 in the unloaded and heavily deformed condition.

due to strain-induced martensitic transformation can not be ruled out. A similar finding was reported by Tomota *et al.* in their work on TRIP-aided steels [161]. Reflection $\{200\}_{\alpha_b}$ was found to weaken whereas the intensity of $\{110\}_{\alpha_b}$ increased with applied stress. This suggested that the change in reflection line intensity is a consequence of both transformation and grain rotation. Therefore, the evolution of texture as a consequence of heavy deformation is anticipated.

Also, it can be observed from figure 5.3(a) the peak shifts to higher d-spacing with deformation with probably an opposite tendency as can be seen, for example, in $\{110\}_{\alpha_b}$ reflection in figure 5.3(b).

Diffraction spectra observed in S2 deformed plastically up to $\varepsilon = 0.25$ exhibited a similar behaviour (figure 5.4).

5.4 *hkl*-specific Response to Mechanical Loading

Using the *in situ* neutron diffraction spectra, it was possible to assess the elastic lattice strain ε_{hkl} [162]:

$$\varepsilon_{hkl} = \frac{d_{hkl} - d^0_{hkl}}{d^0_{hkl}} \tag{5.2}$$

where d_{hkl} and d^0_{hkl} are the measured and stress-free lattice-plane spacings respectively. In the present work d^0_{hkl} was taken as the initial *hkl*-reflection measurement.

5.4.1 Sample S1

Figure 5.5 shows the lattice-plane strain *vs* applied stress in sample S1. Except for the austenite reflections shown in figure 5.5(d), the data presented cover the range of loading up to just before fracture, at 0.126 macroscopic strain.

Figure 5.5(a) shows the anisotropic response to loading of individual reflections of bainitic ferrite. Note that data acquired for a reflection represent the response of a family of grains with identical crystallographic orientation. It is noticeable that the $\{200\}_{\alpha_b}$ reflection seems to respond more readily

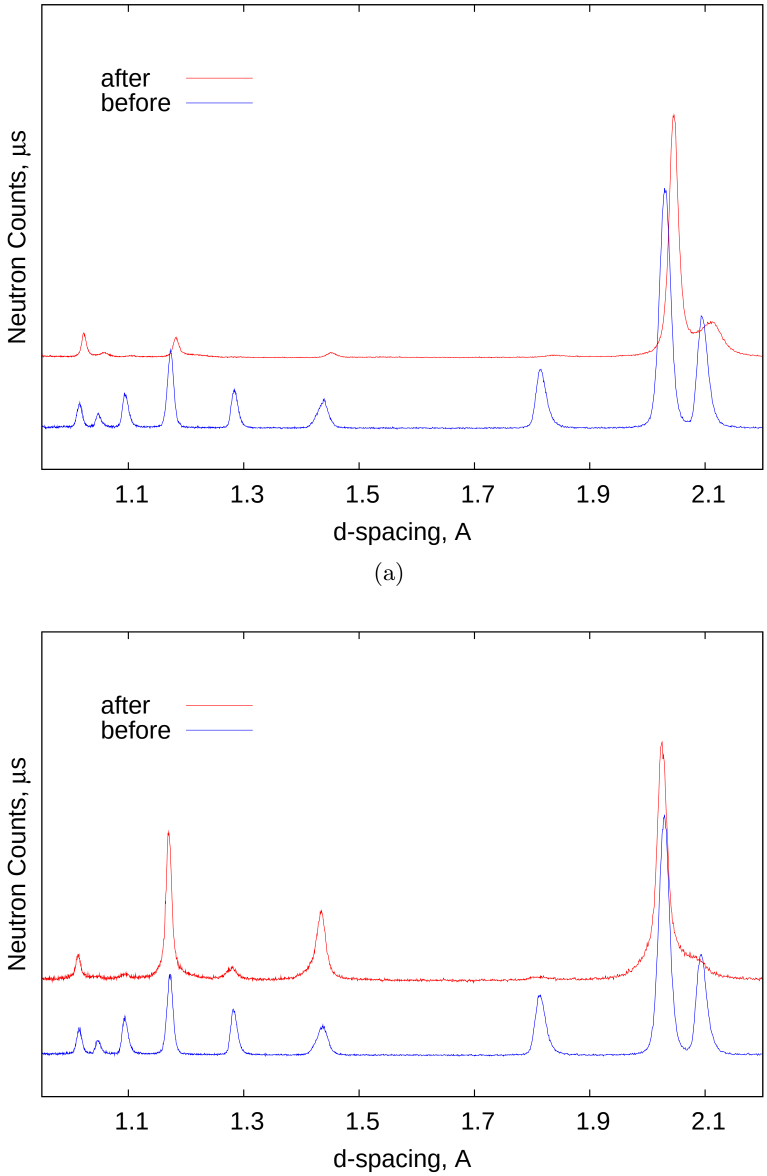

(a)

(b)

Figure 5.4: Axial (a) and transverse (b) diffraction spectra recorded for S2 in the unloaded and heavily deformed condition.

having a rather different diffraction elastic modulus whereas the other reflections are compared with the bulk response. As expected, beyond the onset of macroscopic yield, the lattice elastic strain for all reflections was almost constant as plastic deformation proceeded. This is consistent with figure 5.2 where it is seen that there is no macroscopic local hardening as plasticity progresses.

The transverse strains in the α_b (figure 5.5(c)) are consistent with the above discussion after considering the Poisson's effect, as are the observations in austenite (figures 5.5(b) and 5.5(d)).

5.4.2 Sample S2

Figure 5.6 shows the corresponding data for S2, up to 0.25 macroscopic strain. The key difference when compared with S1 is that, according to figure 5.2, there is macroscopic work-hardening following yielding. So the lattice elastic strains continue to increase (figure 5.6) beyond yielding, albeit at a smaller rate compared with pure elastic loading. This is consistent with the results previously presented in figure 4.5 where a steady, however small, increase in the work-hardening was observed in a similar sample. Thus, the primary difference between S1 and S2 is simply the strain-tempering of the former sample which leads to a different macroscopic stress-strain curve.

Tomota *et al.* observed a similar increase in austenite lattice-plane strain with loading in TRIP-aided multi-phase steels [161]. Two reasons for this observation were suggested. The first, is the stress partitioning between the ferrite and austenite; the second was the preferential martensitic transformation in carbon-low austenite regions. The latter has the effect of shifting austenite peaks due to compositional change. The authors concluded that stress partitioning was responsible for the current observation on the grounds that there were no obvious non-symmetries in austenite peak profile and even after applying high plastic deformation, the peak profile could still be fitted with a Gaussian function.
However, in the current investigation this was not the case as seen below.

Figure 5.7 represents the $\{110\}_{\alpha_b}$ and $\{111\}_\gamma$ peaks in the axial spectrum of sample S2 at zero-load condition. The two-peak fitting was performed

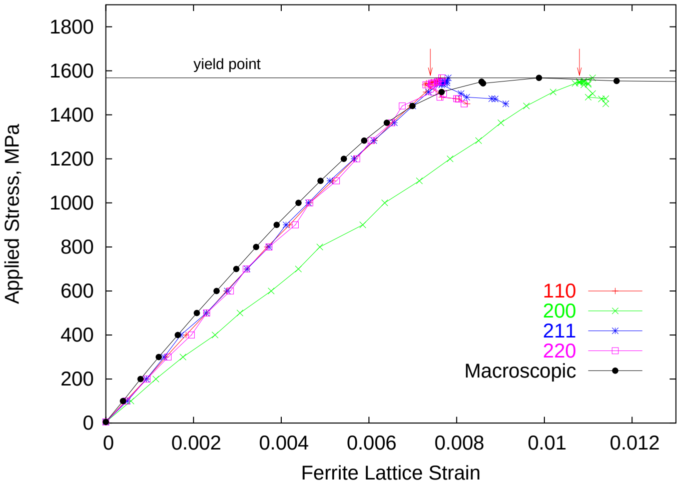

(a) Ferrite reflections as measured in the axial direction

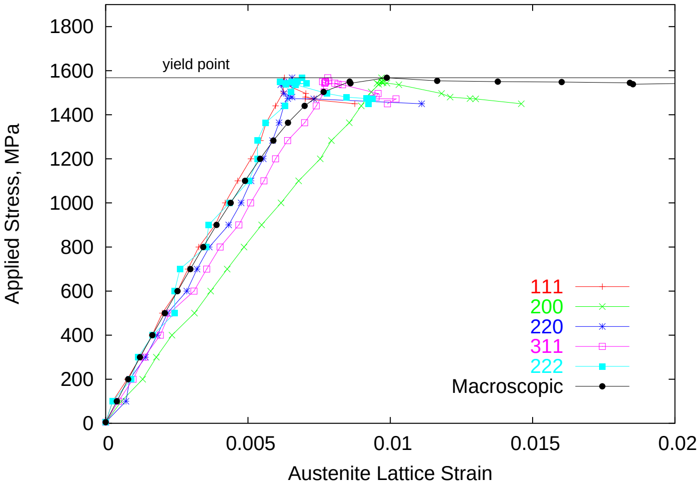

(b) Austenite reflections measured in the axial direction

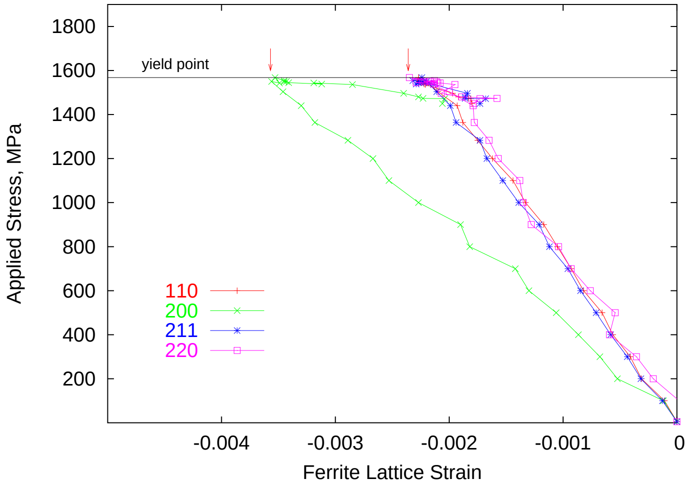

(c) Ferrite reflections as measured in the transverse direction

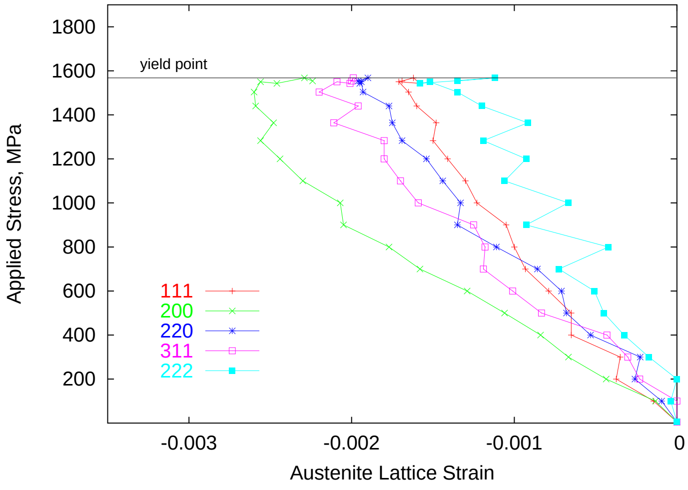

(d) Austenite lattice strains for various reflections as measured in the transverse direction

Figure 5.5: Change in the lattice-plane strain *vs* applied stress in sample S1. The horizontal line denotes yield.

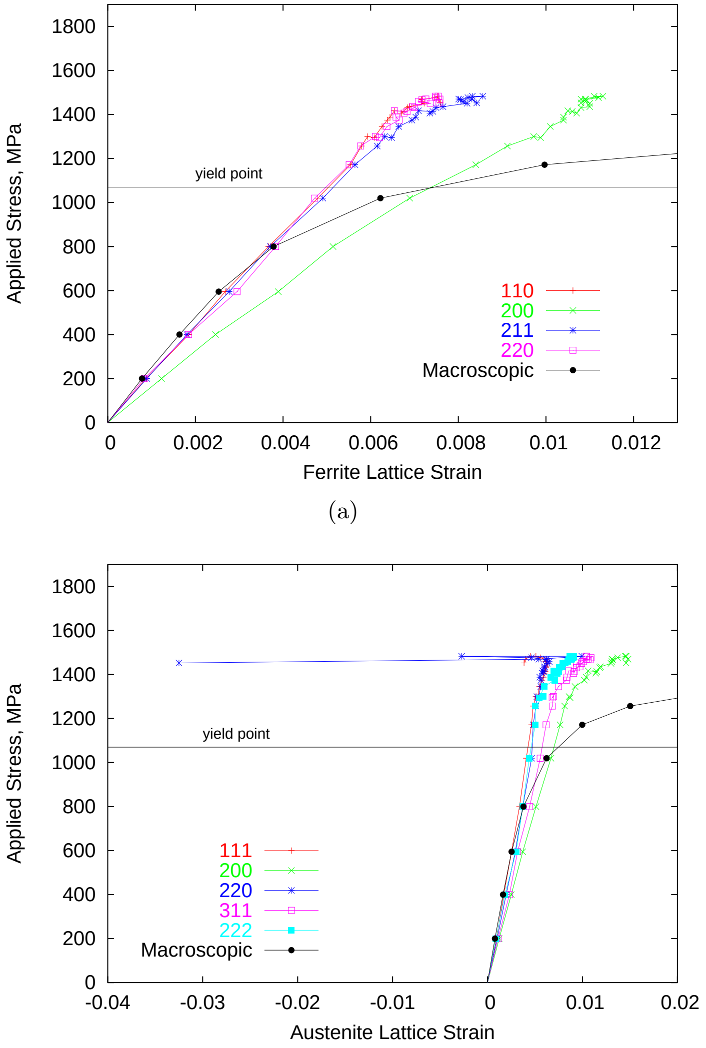

(a)

(b)

Figure 5.6: Change in the lattice strains *vs* applied stress in S2. The horizontal line denotes the yield point level. Spectra were acquired in the axial direction.

through fitting to a time-of-flight profile function which is composed of a convolution of Gaussian, Lorentzian and single exponential functions.
When a single $\{111\}_\gamma$ was fitted, the fit was poor as can be seen in figure 5.7(a). On the other hand, when two $\{111\}_\gamma$ peaks were assumed, the fit was far more satisfactory with negligible residuals (figure 5.7(b)). The two $\{111\}_\gamma$ peaks represent C-high and C-low austenite respectively. To test this hypothesis, the fit was performed for the $\gamma+\alpha_b$ doublet in diffraction spectra acquired up to failure. The result is shown in figure 5.8. Indeed the low-carbon austenite fraction, being less stable than the high-carbon type, diminishes with loading.
Matas and Hehemann observed two lattice parameters for the retained austenite corresponding to the heterogeneous distribution of carbon in the austenite [163].

As shown in figure 5.6(b), in the plastic strain regime, the lattice-plane strain of reflections $\{220\}_\gamma$ and $\{111\}_\gamma$ initially increased with loading, however, then decreased. This divergence has been ascribed to the development of internal compressive stresses triggered by martensite transformation [160]. This behaviour was not observed in sample S1.
The discrepancy in the lattice-plane strain of reflection {220} just before fracture could be an experimental error.

5.4.3 Sample S3

Sample S3 was examined only up to a macrostress level of 1893 MPa which corresponds to 0.021 macroscopic strain (figure 5.9). Few spectra were recorded with applied stress in excess of that of the proof strength. The $\{200\}_{\alpha_b}$ and $\{200\}_\gamma$ reflections exhibit the lowest diffraction elastic moduli, consistent with Allen *et al.* [164].

Unlike samples S1 and S2, the elastic lattice strain of austenite reflections diverges well ahead of the onset of macroscopic yield (figure 5.9), with the austenite reflection {111} deviating from linearity at approximately 700 MPa. This is indicative of a higher degree of structural anisotropy.

It is important to mention that, in stress measurements, when the lattice strain is attributed to the macroscopic stress applied in the plastic regime,

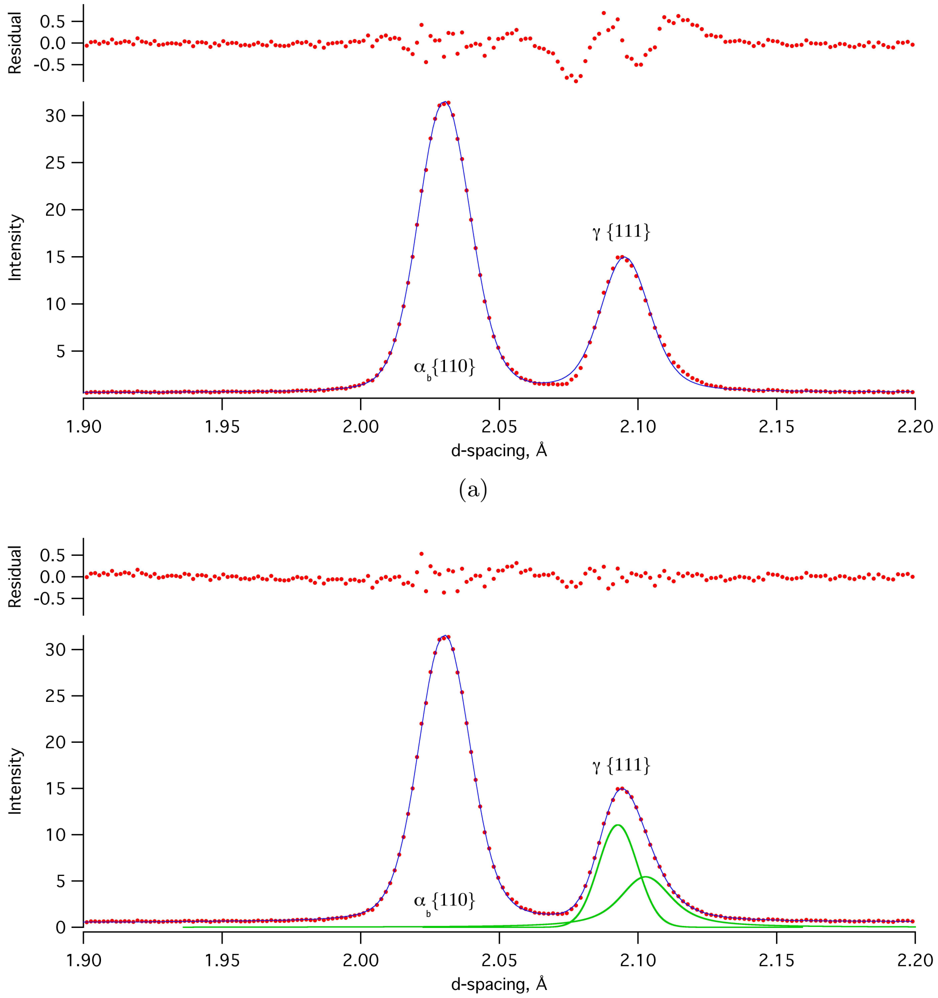

(a)

(b)

Figure 5.7: Two-peak fitting of $\{110\}_{\alpha_b}$ and $\{111\}_\gamma$ in S2, as-heat-treated. Axial diffraction spectrum.

the use of a reflection line which is known to be relatively insensitive to residual intergranular stresses is recommended [159].

In case of FCC and BCC iron, $\{311\}_\gamma$ and $\{211\}_{\alpha_b}$ lattice planes respectively are favoured since they exhibit a linear strain behaviour with ‘at least’ uni-axial loading [165].

As shown in figures 5.5(b), 5.6(b) and 5.9(b), indeed the austenite lattice plane {311} exhibits an intermediate strain behaviour with applied stress

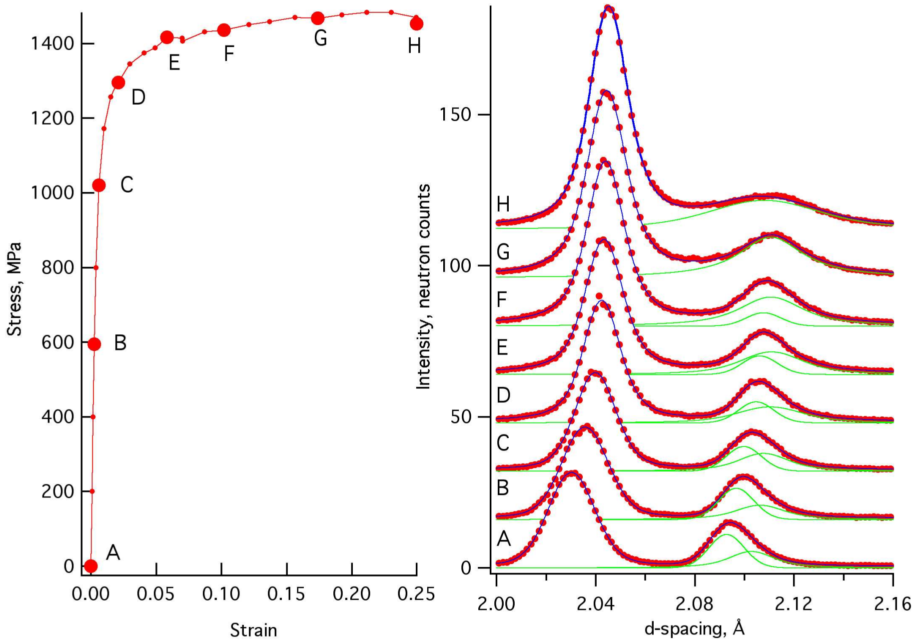

Figure 5.8: The evolution of low-carbon and high-carbon populations of the retained austenite with strain in sample S2. Diffraction spectra were acquired from bank 1.

compared with that of $\{200\}_\gamma$ and $\{111\}_\gamma$.

The possibility of strain-induced transformation into martensite has been considered through monitoring the evolution of austenite reflections intensities with applied stress as shown in figure 5.10. The intensity of reflection $\{200\}_{\alpha_b}$ is also presented for comparison. The strain-induced martensite transformation is naturally accompanied by a reduction in austenite intensities. As shown in figure 5.10, apparently the transformation only starts to take place at as high macroscopic stress level as 1657 MPa (vertical line). A value which is higher than the yield strength (1575 MPa). This indicates the exceptional austenite stability against stress-assisted martensitic transformation. Nevertheless, there is a certain anomaly with the $\{111\}_\gamma$ reflection intensity which initially increases with applied stress. Indeed this observation was previously reported in the literature where it was ascribed to grain rotation [160].

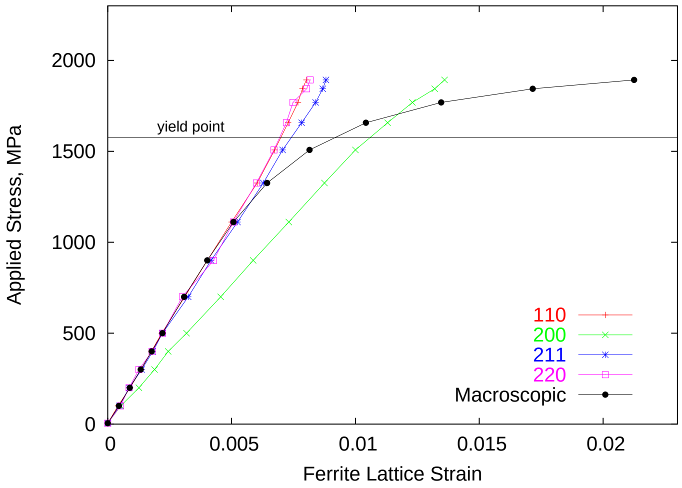

(a)

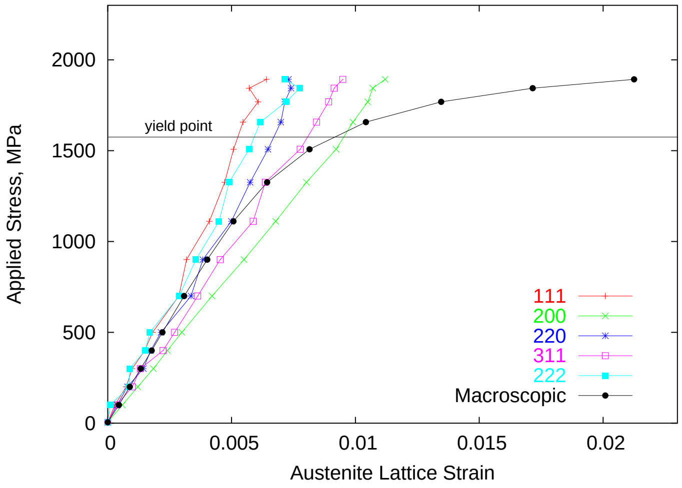

(b)

Figure 5.9: Change in the lattice-plane strain *vs* applied stress in S3. Diffraction spectra were acquired in the axial direction.

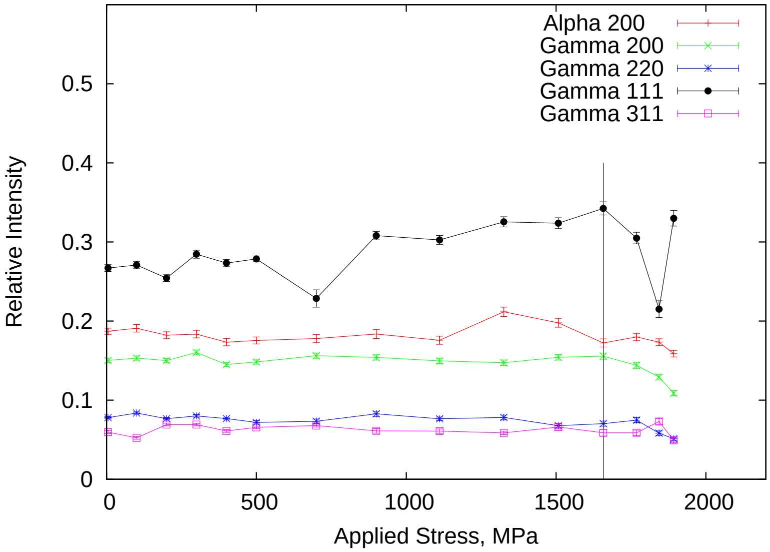

Figure 5.10: The evolution of peak intensities *vs* applied stress in sample S3. Data were measured in the axial direction. Intensities were normalised to that of $\{110\}_{\alpha_b}$ reflection.

5.5 Summary

Three differently processed bainitic steel samples were investigated using *in situ* neutron diffraction during the course of deformation. The following points may be summarised:

1. Preferential martensitic transformation, evolution of texture and grain rotation were observed as deformation proceeded.
2. The generation of *hkl*-specific compressive internal stresses in the austenite has been observed.
3. As previously observed using X-ray diffractometry, lattice distortions have been confirmed.
4. Compositional changes were observed in the austenite as a result of deformation. The change in the average austenite carbon content is a result of preferential transformation of the low-carbon austenite.

5. Anisotropy in austenite grains response to plastic deformation was observed. This could be explained in terms of intergranular stresses.

Chapter 6

Conclusions and Prospects

The present steels, in the as-transformed condition, offer an incredible combination of strength and ductility due to their high carbon content and proper alloying which enabled the formation of bainite at very low temperatures, yet within reasonable holding times. The result of the low-temperature transformation was the generation of a nanoscale microstructure in bulk samples.

This novel microstructure was obtained without excessive or expensive alloying. The high-Si concentration, and in some steels combined with Al, enabled a complete suppression of cementite during bainite transformation. These factors all support commercial exploitation.

The current work aimed at the further development of these remarkable steels in terms of strength and ductility. Strain-aging was adopted and found to result in a considerable improvement in strength without appreciable loss in ductility. As such, a superior combination of strength and ductility was possible *via* affordable, easy to produce, nanostructured steel with mechanical properties comparable to the far more expensive types of maraging steels and dimensionally limited metallic glasses.

Through optimising composition and processing routes, a wide spectrum of mechanical behaviour was observed, outperforming many commercially available steel grades.

A better assessment of the evolution of texture with plastic deformation was carried out using X-ray and *in situ* neutron diffraction. The implication on correct estimation of phase fractions was discussed and successfully dealt with using the Rietveld and Dickson methods. The impact of heavy deformation on erroneous estimation of lattice parameters, especially that of the austenite, was described. Evidence of a change in the austenite lattice parameter with plastic strain was also established. There are contributions both due to compositional change and from possible residual stresses which should not be ruled out. The response to plastic strain of two populations of carbon-rich and carbon-poor austenite was observed. This confirmed the findings by Matas and Hehemann [163].

The following points could be studied further:

1. Some less attended areas, for example, high-cycle and low-cycle fatigue properties, and the mechanical properties of steel structures strained prior to bainite transformation.

2. The texture developed in the plastically deformed steel structures could be investigated further using traditional pole figures.

3. The tempering behaviour of the current steels is not fully studied in the literature and a comprehensive study using transmission electron microscopy would be beneficial.

4. It would be interesting to attempt to model the mechanical behaviour of the current steels taking into account the present findings and various processing parameters.

Appendix A

Thermal Analysis

The work presented here deals with the tempering of carbide-free bainite. Differential scanning calorimetry, X-ray diffraction and scanning electron microscopy have been used to characterise the process.

A.1 Differential Scanning Calorimetry

Many phase transformations are accompanied by the generation or absorption of heat, which can be monitored using techniques such as differential scanning calorimetry (DSC). It works by assessing the heat flow between a sample and an inert reference during a specified temperature programme [166].

A sample weighing a few milligrammes is heated at a constant rate (isochronal annealing [167]) or studied isothermally.

A.1.1 The Zero-line

An isochronal DSC output is shown schematically in figure A.1.

The *zero-line* is measured without the sample to reflect the thermal behaviour of the measuring system [166]. Deviations from the zero-line when the experiment is repeated with a sample indicate activity in the sample.

In the present work, the determination of the zero-line was not necessary since the calorimeter used the Tzero$^{\mathrm{TM}}$ technique by which the measured curve is automatically corrected for thermal effects caused by the DSC apparatus. All further discussions assume a zero-line correction.

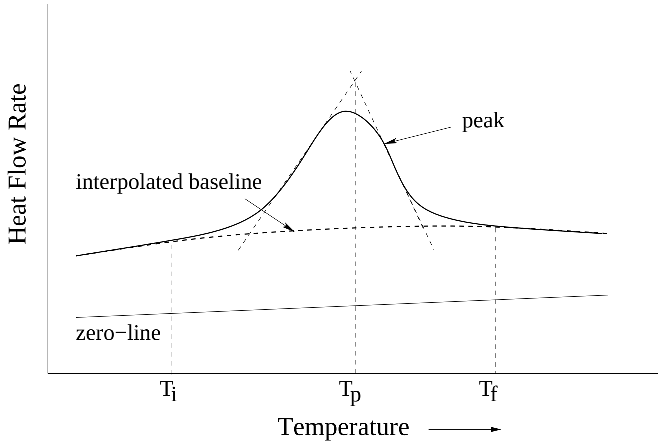

Figure A.1: An isochronal DSC curve. T_i is the initial peak-temperature; T_p is the peak-maximum temperature and T_f is the final peak-temperature.

A.1.2 The Baseline

Any enthalpy change can be determined by integrating the area under the heat capacity *vs* temperature thermogram. The *baseline* is that between T_i and T_f if there is no enthalpy change [166].

Figure A.2 shows a peak with the baseline constructed.

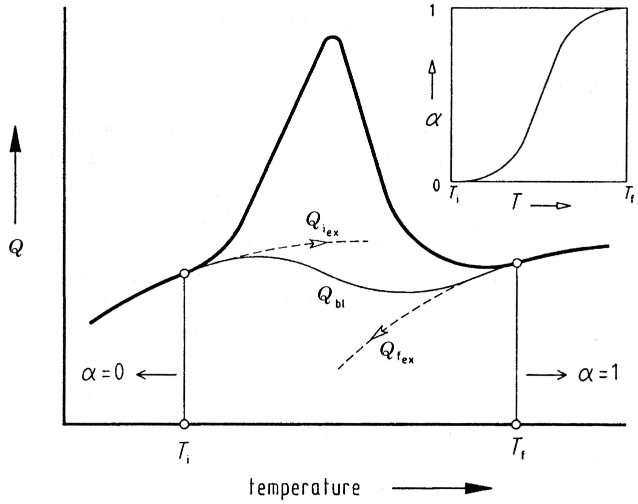

Figure A.2: Construction of the baseline [166].

The method used to estimate the baseline in present work is as follows [168]:
If the degree of reaction $\alpha(T)$ is known approximately, the change in the slope of the baseline under a peak between T_i and T_f may be expressed as:

$$\left(\frac{dQ}{dT}\right)_{bl} = (1-\alpha)\left(\frac{dQ}{dT}\right)_{T_i} + \alpha\left(\frac{dQ}{dT}\right)_{T_f} \tag{A.1}$$

where the subscript *bl* stands for 'baseline'.
It follows that Q_{bl} can be given as:

$$Q_{bl} = (1-\alpha)Q_{i,ex} + \alpha Q_{f,ex} \tag{A.2}$$

where $Q_{i,ex}$ and $Q_{f,ex}$ are the extrapolated parts of the measured curve as shown in figure A.2. In order for Q_{bl} to be calculated, $Q_{i,ex}$ and $Q_{f,ex}$ are extrapolated as polynomials between T_i and T_f.

Figure A.3 shows an example of a baseline construction for a peak measured in the scanning mode with calculated enthalpies and peak characteristic temperatures.

It is important to note that peak-maximum temperature is not necessarily the absolute maximum temperature (shown underlined), which is the temperature at the maximum difference between the measured DSC curve and the interpolated baseline.

A.1.3 The Specific Heat Capacity

Heat capacity is related to thermodynamic quantities such as free energy and entropy. The specific heat capacity can be estimated from the measured heat flow rate as follows [166]:

$$c_p = \frac{C_p}{m_s} = \frac{Q_m - Q_0}{m_s \Phi} \tag{A.3}$$

where Q_m is the measured heat flow rate, Q_0 is the heat flow rate corresponding to the zero-line, m_s is the sample mass and Φ is the heating rate. This assumes that the substance studied remains inert.

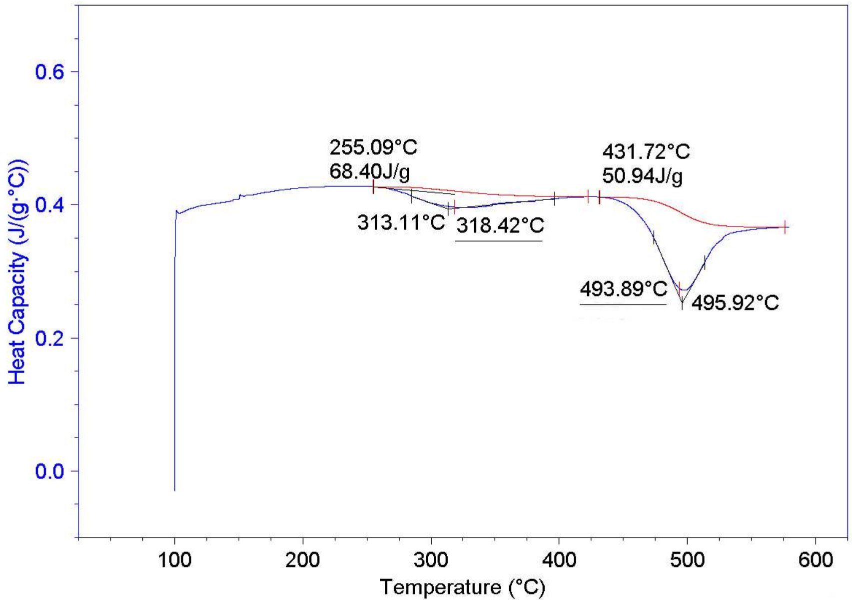

Figure A.3: DSC thermogram of Sp9c heat-treated at 200°C and pre-strained to 0.01 strain. The heating rate used was 30°C min^{-1}. Calculated areas under the peaks are shown.

A.1.4 Activation Energy

The activation energy (E) was calculated using a Kissinger-type method [169]:

$$\ln \frac{T_{f'}^2}{\Phi} = \frac{E}{RT_{f'}} + \text{constant} \tag{A.4}$$

where $T_{f'}$ denotes the temperature at which a specified degree of phase transformation is attained, E is the activation energy and $R = 8.3144$ J mol^{-1} K^{-1} is the gas constant. Using data from different heating rate experiments, the activation energy of a reaction can be determined by monitoring the change in $T_{f'}$ and plotting $\ln \frac{T_{f'}^2}{\Phi}$ vs $\frac{1}{RT_{f'}}$, the slope of which yields the activation energy E.

$T_{f'}$ was taken to be the peak-maximum temperature T_p. Except when T_p could not be determined due to overlap with other reactions, T_i was used instead.

A.2 Experimental Procedures

TA Instruments heat flux DSC Q 1000 was used. Dried nitrogen flow at 50 ml min^{-1} helped minimising oxidation during tempering. The measured temperature on heating was calibrated using the melting point of pure indium. Heat flow rate calibration was carried out using sapphire which allowed the determination of the $c_p(T)$ function for comparison against published data.

Three alloys have been analysed, Sp9c, Sp10c and Sp11c, with a variety of initial bainite microstructure and both in the undeformed and deformed states. The deformed samples were cut from tensile test specimens described in Chapter 3. When the tensile tests had been conducted to failure, the DSC samples were cut from as close to the fracture surface as possible.

Samples with weights ranging from 9–50 mg were characterised. Each sample was placed in an aluminium pan which was closed by lightly pressing an aluminium lid, thereby limiting the analysis to <600°C. An empty pan with known mass was used as a reference.

Two running modes have been used for the assessment of kinetic parameters; the isothermal and isochronal modes, the latter at 10, 20 and 30 °C min^{-1} constant heating rates. Isothermal experiments were carried out by equilibrating at 300°C for 2 h.

After the DSC runs, samples were prepared for metallographic investigation, details of which can be viewed elsewhere, and etched with nital (2%). A JEOL JSM-5500 LV scanning electron microscope (SEM) operated at 10 and 20 kV was used in secondary electron imaging mode to investigate structural variations after tempering. Given that samples underwent tempering during the DSC investigation, phase identification, in particular austenite and martensite, should be less ambiguous [170].

Phase fractions and austenite lattice parameters have also been carried out using X-ray diffractometry.

A.3 Analysis

A.3.1 Reactions in Isochronal Mode

Peaks in DSC thermograms represented exothermic reactions. Apparently there are no reported DSC investigations on the tempering of carbide-free bainitic steels. Fe-C, Fe-C-Cr and Fe-C-Cr-Mo martensites have been studied using DSC [139, 140, 167, 171, 172].

Gojić *et al.* used thermal analysis to study a hot-rolled carbide-containing bainitic steel (Fe-0.4C-0.85Mn-0.33Si-1.02Cr-0.24Mo wt%) [172]. The thermal events observed in the present work in the isochronal mode with $\Phi = 10°\text{C min}^{-1}$ were speculated to be:

- Segregation and clustering of carbon atoms;
- precipitation of transition carbides ε/η;
- decomposition of the retained austenite;
- precipitation of the θ-carbide (cementite).

Given the lack of reports in the literature regarding the tempering behaviour of fully bainitic carbide-free steels studied by DSC, the interpretation of observed peaks is speculative and further experimental evidence is thus required. Nevertheless, the results obtained stimulate the need for further research and direct observations.

Segregation & Clustering of Carbon Atoms

In carbon-supersaturated martensite, tempering is preceded by the redistribution of carbon atoms from an ordered interstitial sub-lattice to lower-energy sites such as dislocations and grain boundaries [139, 173].

In low-alloy low-carbon martensitic steels, this event is the first stage of tempering, although with a high M_S temperature, the segregation of carbon atoms may already have occurred during quenching as the martensite forms, a process known as ‘auto-tempering’ [174].

Precipitation of ε/η-carbides

Further tempering leads to the precipitation of transition metastable carbides. A 1.3 wt% C martensite tempered at 120°C for 5–40 days was found using X-ray diffraction to precipitate ε-carbide ($Fe_{2.3}C$) [175]. On the other hand, a further TEM study revealed a different orthorhombic η-carbide or η-Fe_2C [176]. Ohmori and Tamura reported the precipitation of the hcp ε-carbide [177]. A more recent study by Han *et al.* confirmed the precipitation of the η-carbide or η-Fe_2C in early stage of Fe-C martensite tempering [167]. It seems that ε/η carbides form in most steels containing more than 0.2 wt% [174]. On the other hand, a huge dislocation density can prevent precipitation by acting as strong traps for carbon.

Decomposition of Retained Austenite

The observed second stage during the tempering process is the decomposition of retained austenite, characterised by a large heat release (figure A.4).

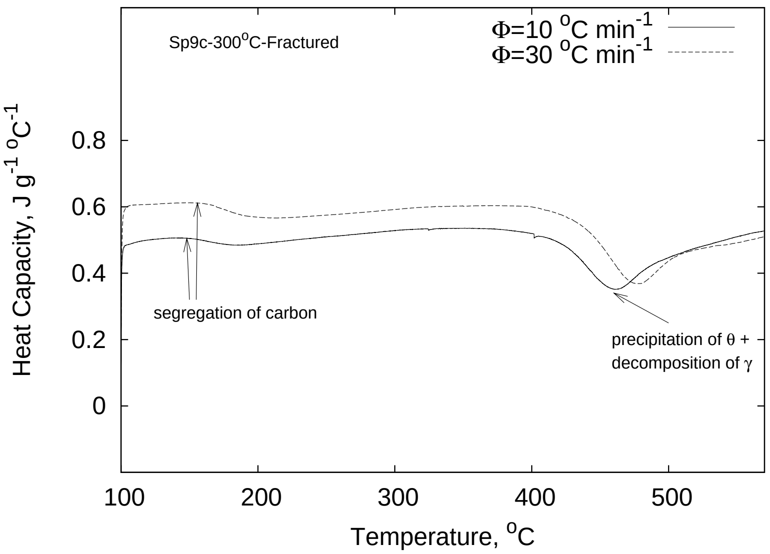

Figure A.4: DSC thermograms of Sp9c sample transformed into bainite at 300°C and subsequently strained to failure.

The decomposition products are ferrite plus fine carbides in the prior fine austenite regions, and pearlite in larger γ regions [138].

However, according to Speich and Leslie, retained austenite decomposition may be bainite [174].

In the work of van Genderen *et al.*, γ decomposition resulted in a more carbon-enriched austenite plus ferrite [139].

Precipitation of θ-carbide

The last thermal reaction observed is a peak which might denote the precipitation of cementite (θ-carbide, orthorhombic). This reaction could be accompanied by or after the decomposition of austenite. Transition carbides formed in earlier stages dissolve [139] allowing the more thermodynamically stable, the cementite, to form in a reaction which is largely accompanied by length reduction rather than heat release. This pronounced dimensional change makes dilatometry a complementary tool to DSC [140].

The morphology of cementite particles is plate-like which is detrimental to mechanical properties. Further tempering leads to particle coarsening and spheroidisation [178].

In the present work, cementite probably started to precipitate in the range 510–531°C.

Effect of Heating Rate on DSC Measurements

As shown in figure A.4[†], a higher heating rate shifts the peak to a greater temperatures, as expected in any thermally activated reaction.

Effect of Alloy Composition

The main difference between the steels studied is the Co and Al concentrations. Therefore, it was expected to observe differences in terms of the kinetic parameters during tempering.

As shown in figure A.5, the apparent heat capacity of the more alloyed steels Sp10c and Sp11c were greater than Sp9c. It is also apparent the occurrence of peak shift towards greater temperatures with Sp10c and Sp11c compared with Sp9c.

[†] Except for θ-carbide precipitation due to overlap with other reactions, arrows in DSC thermograms point to the initial reaction temperature.

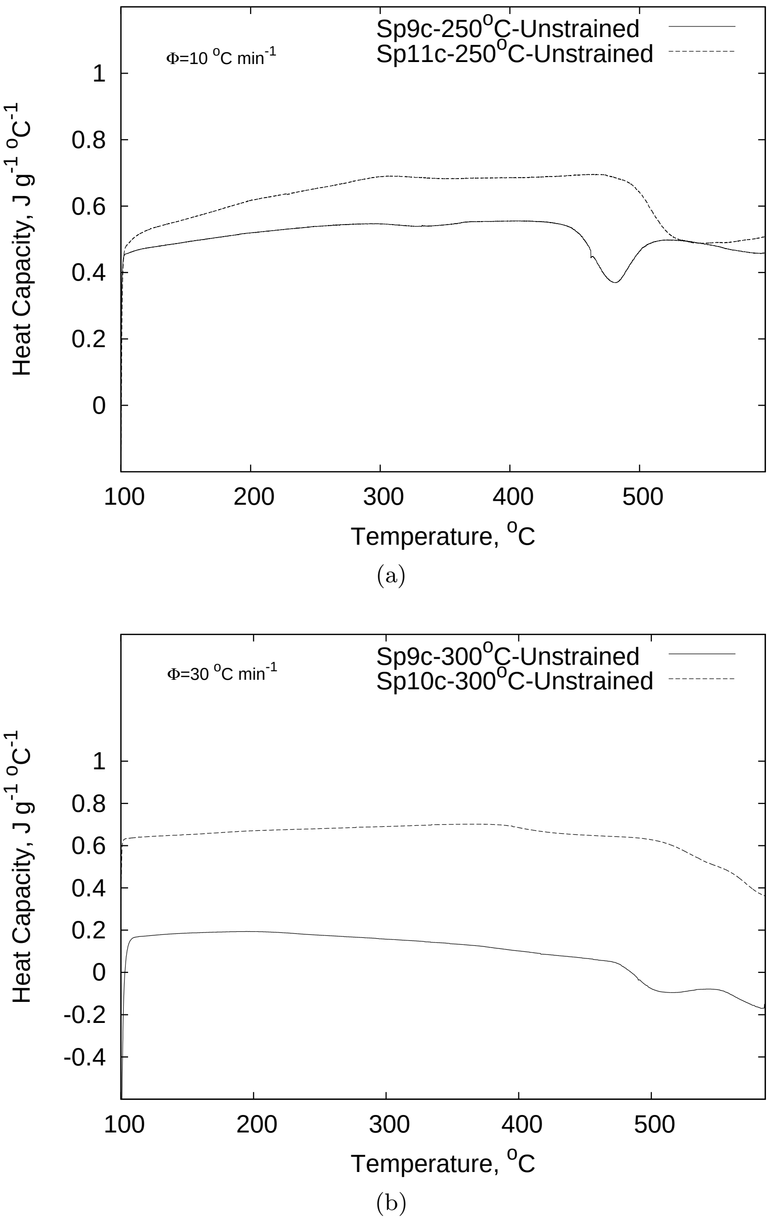

(a)

(b)

Figure A.5: DSC thermograms of studied steels tempered in the scanning mode.

Figure A.6(a) exhibits the microstructure of Sp9c following the DSC experiment. For comparison, figure A.6(b) represents the sample prior to heat-treatment.

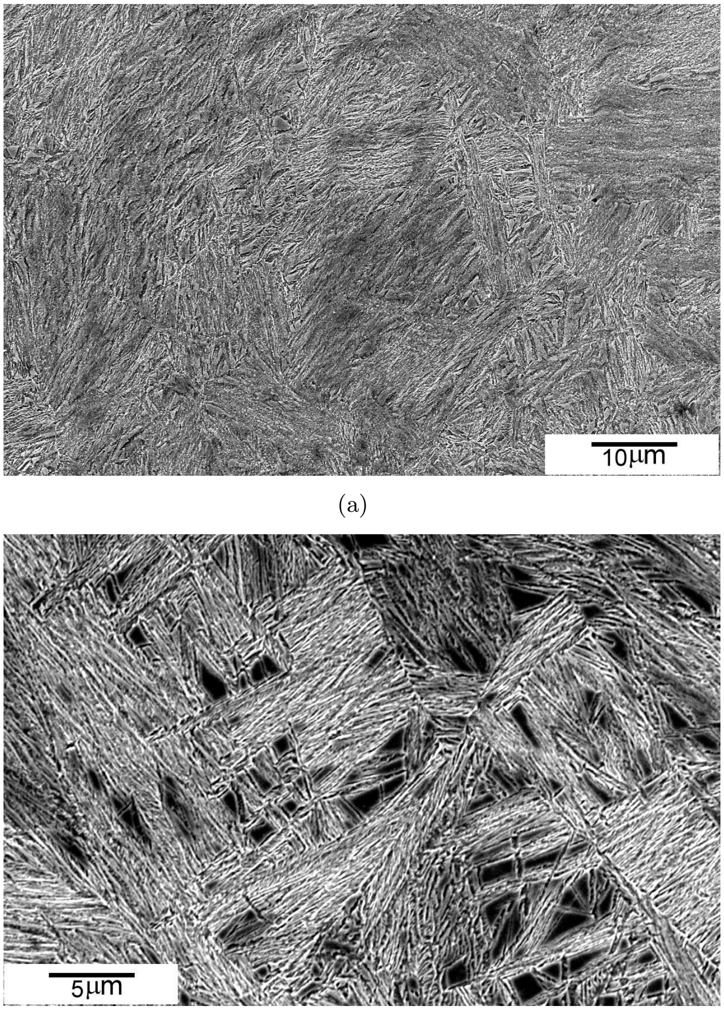

(a)

(b)

Figure A.6: SEM micrographs exhibit: (a) sample Sp9c, unstrained and tempered and (b) same sample, untempered. Samples underwent bainite transformation at 250°C for 15 h prior to DSC experiment. Tempering was carried out within the range 100°C to 600°C with the rate 10°C min^{-1}. Note the absence of the austenite in the tempered condition.

Effect of Bainite Transformation Temperature

Figure A.7 shows the DSC curves of Sp9c samples transformed into bainite at different temperatures.

The possible precipitation of transition carbides (arrowed) was delayed

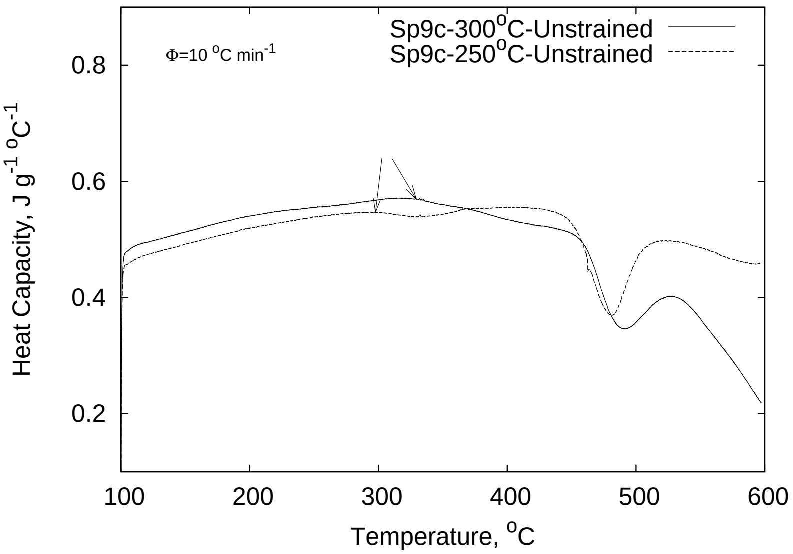

Figure A.7: Measured DSC curves demonstrate the possible effect of transforming bainite at different temperature on subsequent tempering kinetics.

for the steel transformed at 300°C compared with steel transformed at 250°C, however, the reaction was more prominent and overlapped with the subsequent peak presumably denoting the decomposition of austenite. Since the dislocation density in bainite formed by transformation at 300°C is less than that formed at 250°C [2], ε/η-carbide precipitation is favoured in the former.

Austenite carbon content C_γ was determined using X-ray diffraction and found to be 1.6 and 1.2 wt% carbon for the alloy transformed at 300 and 250°C respectively. According to measured C_γ, the retained austenite in Sp9c sample transformed at 250°C should be less stable in comparison with Sp9c-300°C. The would-be γ-decomposition peak-maximum temperature was 480.4°C in the former compared with 486.6°C in the latter.

As shown in figure A.7, a peak following the proposed γ-decomposition peak was observed in both samples. This peak is speculated to denote carbide precipitation. There is a striking difference between the two samples at this stage presumably due to the difference in C_γ.

Figure A.8 shows SEM micrographs of Sp9c-300°C.

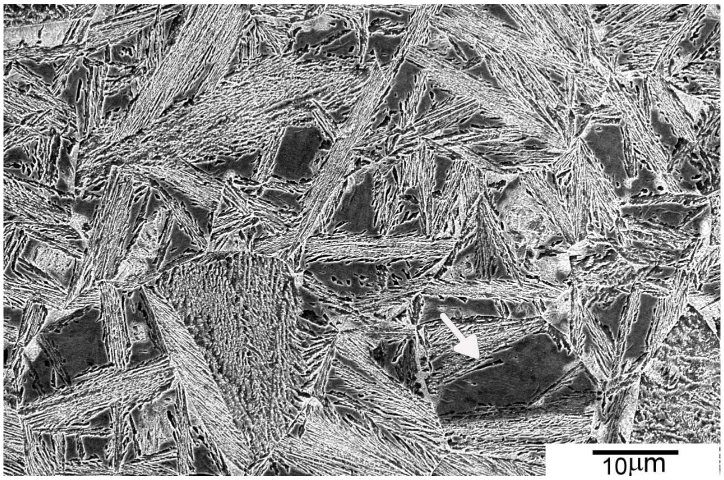

(a)

Figure A.8: Sp9c sample heat-treated at 300°C, unstrained. Sample was continuously heated within the range 100–600°C at 10°C min^{-1}. The bainitic structure is clearly visible with some bainite sheaves being etched preferentially. Arrow points to a possible austenite grain.

Effects of Strain

As presented in figure A.9, only deformed steels exhibited an early stage thermal reaction during tempering, presumably stands for carbon segregation (arrowed). This could be due to the presence of the strain-induced martensites.

The microstructure of Sp9c-300°C pre-strained to 0.1 ε is shown in figure A.10.

Figure A.9(b) clearly shows a different tempering behaviour at later stages marked also by peak shift towards lower temperature as the degree of pre-strain increased.

Upon deformation, austenite grain features smaller crystallites due to the introduction of dislocations. It is therefore possible that these dislocation bands provide nucleation sites which facilitate the decomposition of austenite into ferrite. It is known that the deformation of austenite in the intercritical annealing region *initially* accelerates the decomposition into bainite [179, 180].

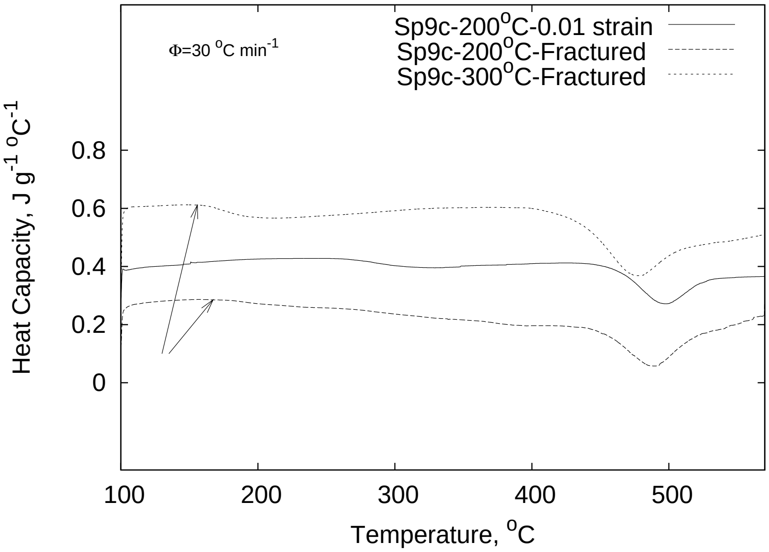

(a)

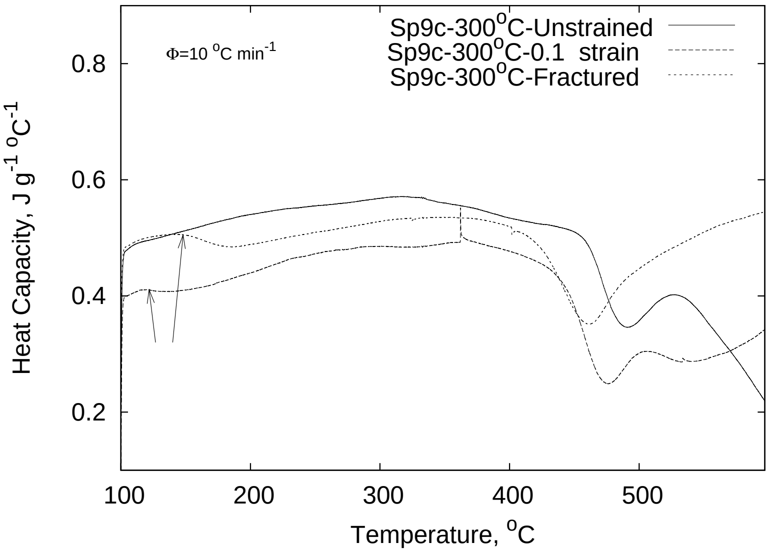

(b)

Figure A.9: DSC curves measured for sample Sp9c heat-treated at different temperatures and strained to various strain levels.

Table A.1 demonstrates that the activation energy of austenite decomposition in the fractured sample was slightly higher than that in the unstrained sample.

	Unstrained					Fractured				
Events	$\Phi = 10$ °C min^{-1}		$\Phi = 30$ °C min^{-1}		E (kJ mol^{-1})	$\Phi = 10$ °C min^{-1}		$\Phi = 30$ °C min^{-1}		E (kJ mol^{-1})
	T_i	T_p	T_i	T_p		T_i	T_p	T_i	T_p	
Segregation of C atoms	—	—	—	—	—	148	191	156	200	203.4 (T_i)
Precipitation of ε/η	329	—	210	—	—	—	—	—	—	—
Decomposition of γ	454	487	471	505	287.8 (T_i) 284.7 (T_p)	368	459	397	475	292.9 (T_p)
Precipitation of θ	530	—	548	—	333.1	—	—	—	—	—

Table A.1: Kinetic parameters of sample Sp9c heat-treated at 300°C for 6 h, unstrained and fractured. Heating range was 100–600°C.

Figure A.10: SEM micrograph shows the structure of sample Sp9c transformed at 300°C for 6 h and strained up to 0.1 strain. Tempering was carried out by heating from 100 to 600°C with $\Phi = 10°\text{C min}^{-1}$. Arrows point to a bainite sheaf (right) and a tempered-martensite grain (left).

A.3.2 Isothermal Mode

Figures A.11 and A.12 exhibit heat flow curves of steels Sp9c and Sp11c with bainitic structures transformed at 250°C, unstrained and strained measured in the isothermal mode at 300°C and held for 2 h.

As can be expected, the pre-strained samples showed an early decomposition of the strain-induced martensite. Note the relatively greater slope of the peak's leading edge in the pre-strained Sp9c sample which suggests a faster reaction rate compared with that in the Sp11c fractured sample.

The tempering behaviour of the unstrained samples was different with a gradual heat release with time.

It can be noticed from figure A.11 that, given the difference in the reaction or the rate by which the heat during tempering is released, the microstructure of alloy Sp11c, unstrained, exhibits a better stability against tempering compared with that of Sp9c; same strain condition. This resistance to tempering could be ascribed to the high Co content in alloy Sp11c.

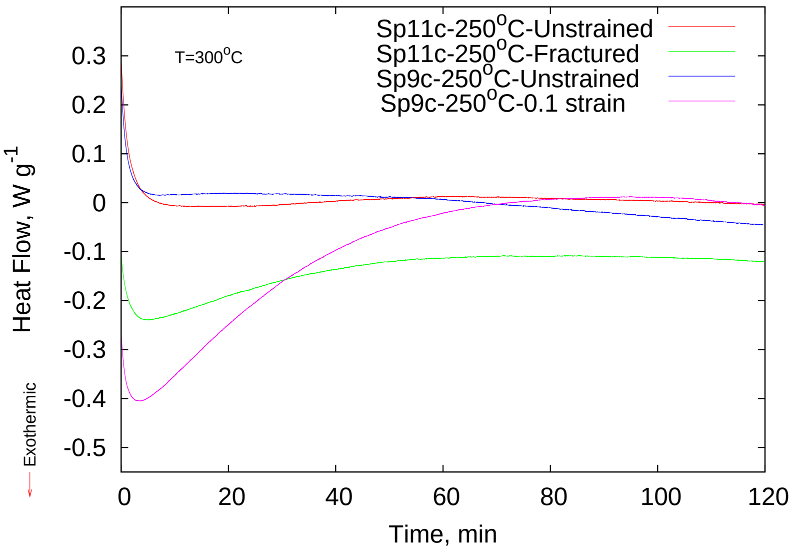

Figure A.11: Measured DSC curves in isothermal mode. See text for more details.

The Possibility of Austenite Decomposition

The decomposition of the retained austenite during the isothermal holding at 300°C for 2 h was minute as presented in table A.2.

Sp9c-250°C-15 h	a_γ (nm)	C_γ (wt%)	V_γ
0 strain	0.36134	1.16	0.27
0 strain+tempering	0.36181	1.33	0.26
0.1 strain	0.36247	1.55	0.14
0.1 strain+tempering	0.36282	1.68	0.13

Table A.2: Microstructural parameters following isothermal heating at 300°C for 2 h.

Furthermore, as can be observed from table A.2, the austenite carbon content increases after straining and or tempering.

As previously mentioned in the last chapter, during straining, austenite lattice parameter increases which might be ascribed to compositional changes caused by selective transformation into martensite which preferentially takes place in austenite regions which are relatively poor in carbon [60].

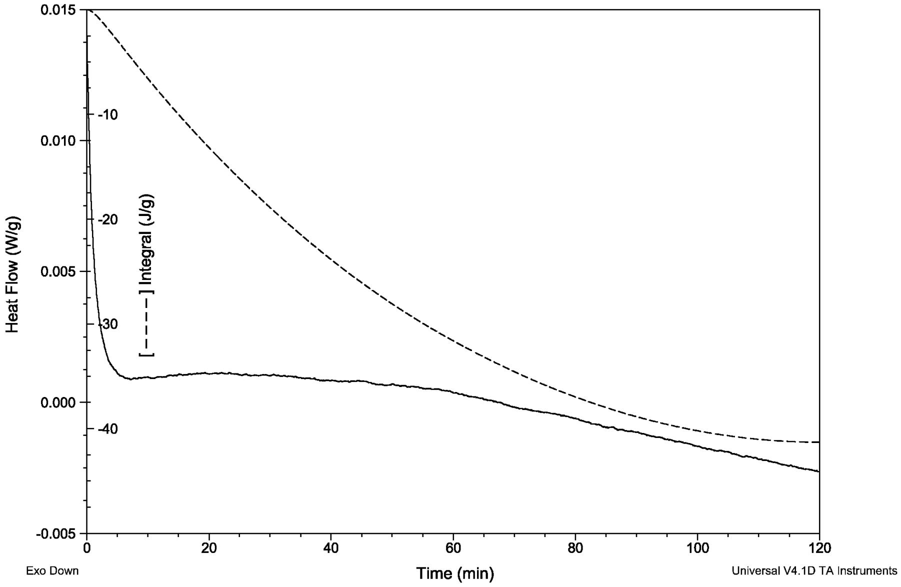

(a) Sp9c-250°C-unstrained. Tempered at 300°C for 2 h.

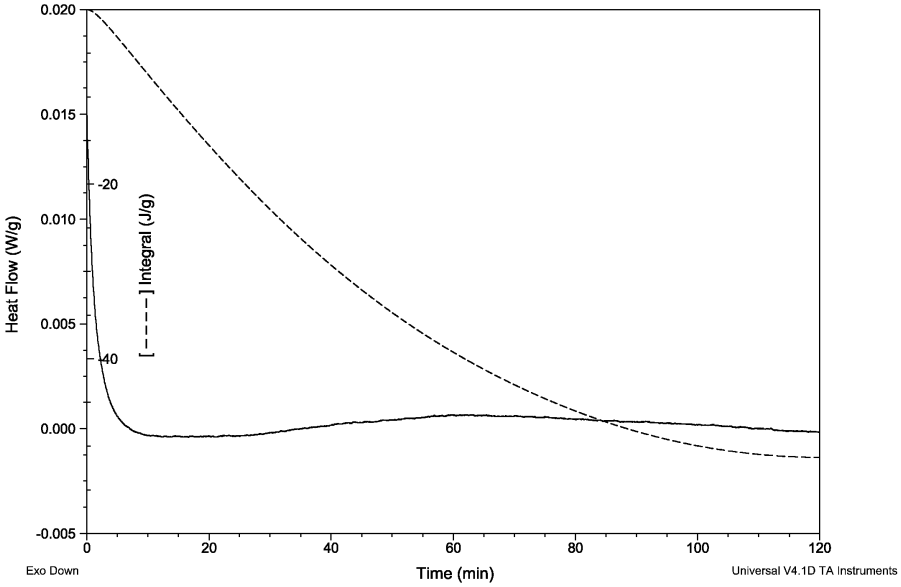

(b) Sp11c-250°C-unstrained. Tempered at 300°C for 2 h.

An increase in a_γ as a result of tempering can be a result of austenite carbon-enrichment.

From the aforementioned findings, it is possible to consider carbide precipitation during the isothermal tempering unlikely. Table A.3 presents

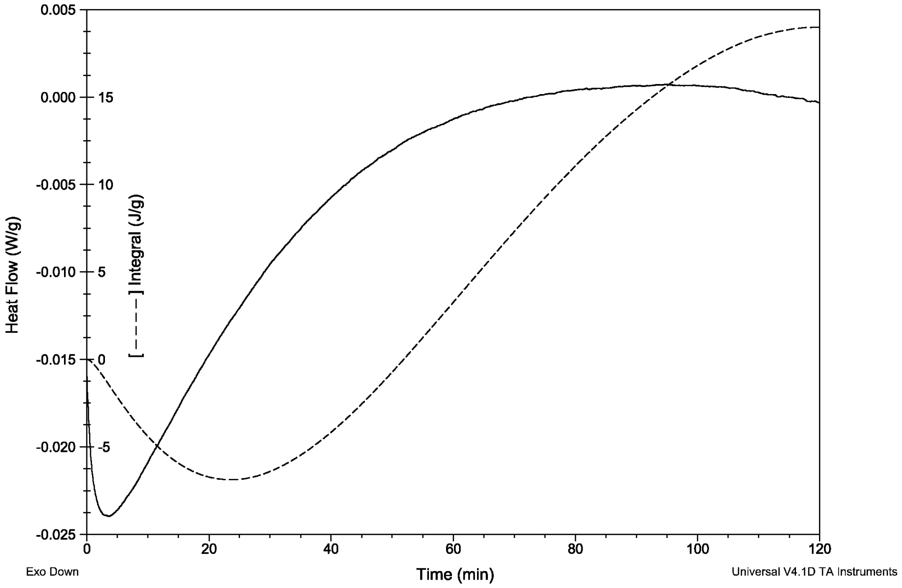

(c) Sp9c-250°C-0.1 strain. Tempered at 300°C for 2 h.

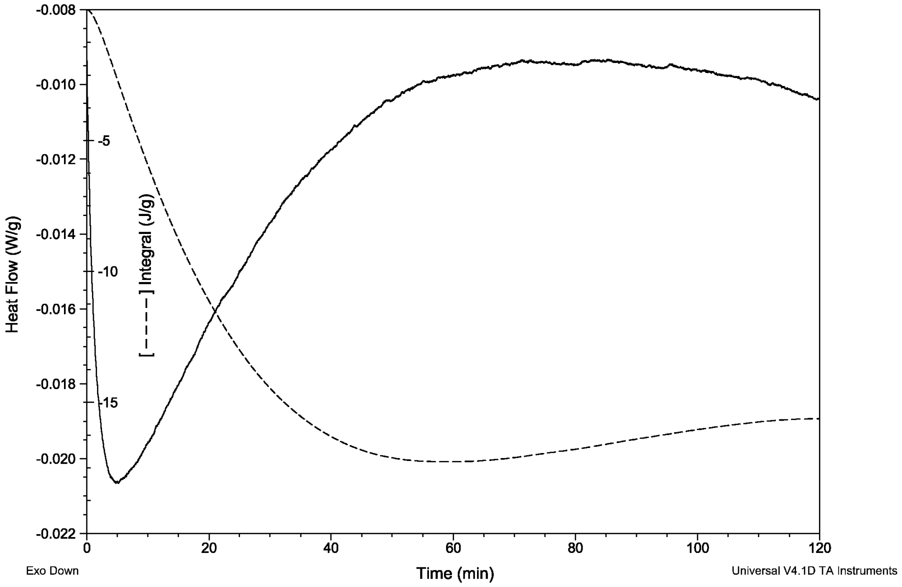

(d) Sp11c-250°C-Fractured. Tempered at 300°C for 2 h.

Figure A.12: Isothermal mode curves which demonstrate the rate of microstructural change during tempering. It is apparent that for pre-strained steel structures, tempering for about 1 hour brings about the necessary structural changes.

Phase	Mass fraction
`BCC_A2` (ferrite)	0.957
`GRAPHITE`	0.004
`M7C3`	0.028
`MC_SHP` (MoC)	0.001
`C2Cr3`	0.009

Table A.3: Phases present at equilibrium in alloy Sp9c held at 300°C. M stands for metal atom which is mainly Mn for M7C3 carbide. Note the absence of cementite.

equilibrium phases in alloy Sp9c when held at 300°C.

Figure A.13 shows microstructural changes following the isothermal holding at 300°C for 2 h of the samples presented in table A.2.

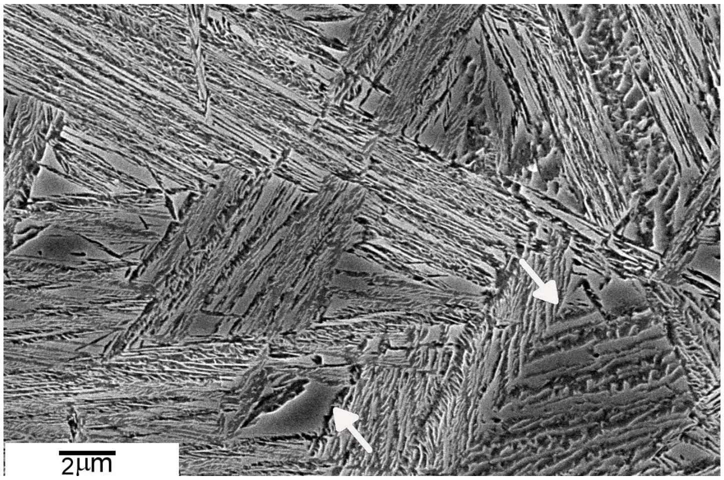

(a) Decomposed austenite region which features the bainitic structure (right) and an austenite grain with partial decomposition (left). Unstrained structure.

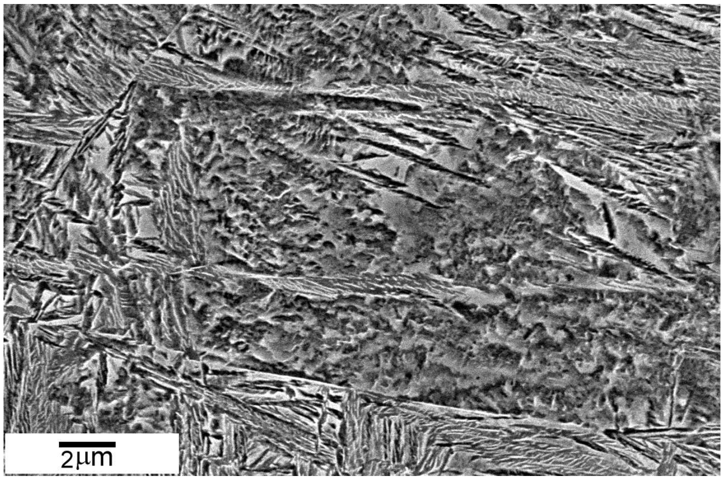

(b) A tempered-martensite grain. Pre-strained structure.

Figure A.13: SEM micrographs of sample Sp9c heat-treated at 250°C, unstrained and 10% strained. Both structures were isothermally held at 300°C for 2 h.

A.4 Summary

The following points may be summarised from the present work:

1. As might be expected, tempering kinetics of carbide-free bainitic steels resemble that of martensitic steels except for the early carbon enrichment stage which was believed to present in strained steel structures only.
2. Thermal effects which probably are associated with the precipitation of transition carbides were observed. However, further experimental evidence is needed.
3. A minor decomposition of austenite into bainite is likely, as has been suggested earlier [174].
4. The event of austenite decomposition does not necessarily involve the precipitation of carbides accompanied with ferrite formation, rather, austenite enrichment takes place combined with the formation of ferrite. This finding is in agreement with the result reported by Han *et al.* [167].
5. Generally, studied steels exhibited a strong tempering resistance.
6. Both elements Co [181] and Al resulted in peak shifts towards greater temperatures implying a higher degree of structural stability.
7. Tempering kinetics were accelerated by decreasing the temperature at which bainite transformed.
8. The austenite phase was observed to be fairly stable when held at 300°C for 2 h regardless the degree of pre-strain.
9. Sp11c was apparently more stable against tempering at lower temperatures, however, it is more sensitive when heated at relatively higher temperatures. The opposite is true for steel Sp9c.

Appendix B

Mechanical Stability of Austenite

The TRIP phenomenon occurs when upon mechanical loading, γ transforms into martensite or any product which leads to a transformation strain.

Mechanical loading to a level below the macroscopic yield strength can assist on existing nucleation sites in austenite so as to render them operative [182]. These nucleation sites would normally be activated by undercooling below the M_S temperature. This is 'stress-assisted' transformation. On the other hand, the transformation process can be induced by plastically deforming the austenite, *i.e.* 'strain-induced transformation'. The latter is true as long as deformation temperature is kept below M_d which is the temperature above which no transformation takes place, and straining simply plastically deforms the austenite islands.

The purpose of the present work is to demonstrate the success of the model proposed by Sherif *et al.* [155] in predicting the mechanical stability of retained austenite in TRIP-assisted steels. On the other hand, it was believed important to assess the model's applicability to other steel systems, for example, bainitic steels.

B.1 Models for Strain-induced Transformation

B.1.1 Sugimoto *et al.* Model

Another important relationship was proposed by Sugimoto *et al.* [55]:

$$\ln\{V_\gamma^0\} - \ln\{V_\gamma\} = k_\gamma \varepsilon \tag{B.1}$$

where k_γ is an empirical constant. Equation B.1 has been used to assess the extent of martensitic transformation. However, in spite of its usefulness, it lacks general applicability since experimental data are needed to derive the fitting parameter k_γ for each alloy and temperature.

As shown in figure B.1, k_γ is found to decrease as the deformation temperature increases.

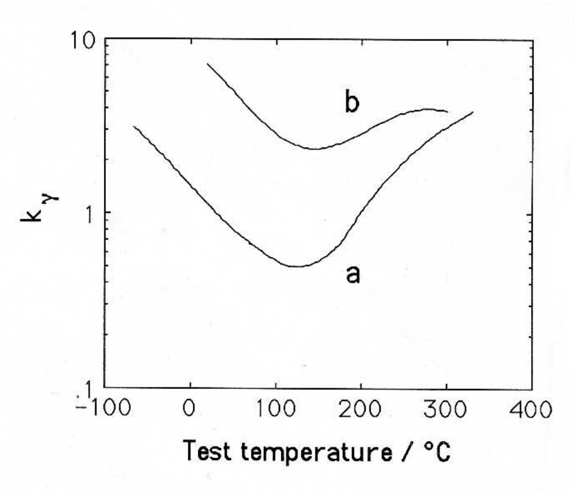

Figure B.1: Plot of the parameter k_γ in equation B.1 versus deformation temperature [55]. Steel a has $M_S = -61\,°\mathrm{C}$ and for b $M_S = -7\,°\mathrm{C}$.

B.1.2 Sherif *et al.* Model

In a recent model, a suggestion was made to explain the mechanical stability of the retained austenite [104, 155]. The transformation behaviour of austenite was ascribed to the free energy available for transformation, *i.e.* k_γ in equation B.1 should depend on $\Delta G^{\gamma\alpha'}$. The *magnitude* of the free energy can be expressed as $\Delta G^{\alpha'\gamma}$. Equation B.1 can be re-written as follows [104, 155]:

$$\ln\{V_\gamma^0\} - \ln\{V_\gamma\} = k_1 \Delta G^{\alpha'\gamma} \varepsilon \tag{B.2}$$

Consequently, $k_\gamma = k_1 \Delta G^{\alpha'\gamma}$ where k_1 is a constant, derived to be equal to 0.00446 mol J^{-1} which is alloy-independent. The value of k_1 was derived by fitting equation B.2 to experimental data of steels with broad range of chemical compositions and deformation temperatures [104, 155].

The free energy term in equation B.2 captures the effect of austenite chemical composition and deformation temperature. The model should be used at temperatures above M_S, up to about 200°C. According to Sugimoto *et al.* [55], beyond a temperature of about 200°C k_γ no longer decreases with temperature (figure B.1). An interesting outcome of the model is that, if the free energy available for transformation is zero, regardless the degree of plastic straining, martensite transformation can no longer be induced, *i.e.* the temperature at which deformation took place is the M_d temperature.

Therefore, it has been possible to establish an adequate model which is capable of predicting the transformation behaviour of retained austenite, particularly its mechanical stability as a function of plastic strain.

Further Validation

The model was further assessed using TRIP-aided steel data form the literature. Figure B.2 shows the result of the predictions made for data from Radu *et al.* [183]. Despite that the carbon content in austenite was not given, the model did predict austenite fractions adequately. Ferrite carbon content was assumed to be 0.03 wt% and C_γ was predicted using:

$$C_\gamma = \frac{\bar{x} - 0.03(1 - V_\gamma^0)}{V_\gamma^0} \tag{B.3}$$

Given an initial volume fraction of austenite 0.136, $C_\gamma = 1.21$ wt%. Therefore, free energies were calculated using MTDATA. Only uniaxial tension data were used.

The model was also applied to *in situ* X-ray diffraction data of TRIP-aided steel reported by Zhao *et al.* [184]. Steel composition had the composition 0.17C-1.46Mn-0.26Si-1.81Al wt%. $C_\gamma = 0.93$ wt% corresponds to $\Delta G^{\alpha'\gamma} = 2856$ J mol^{-1} at room temperature. Figure B.3 shows the result. As shown, within experimental error, the model successfully predicted the evolution of the austenite fraction *vs* plastic strain.

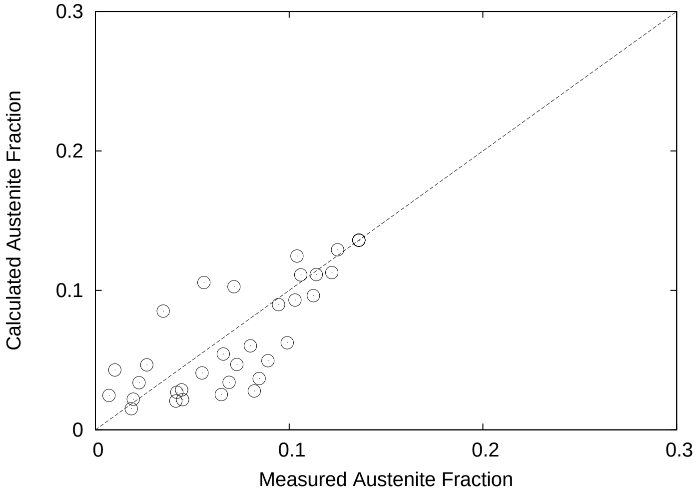

Figure B.2: Application of Sherif *et al.* model to experimental data from [183]. Correlation coefficient 0.82 and standard error ±0.025.

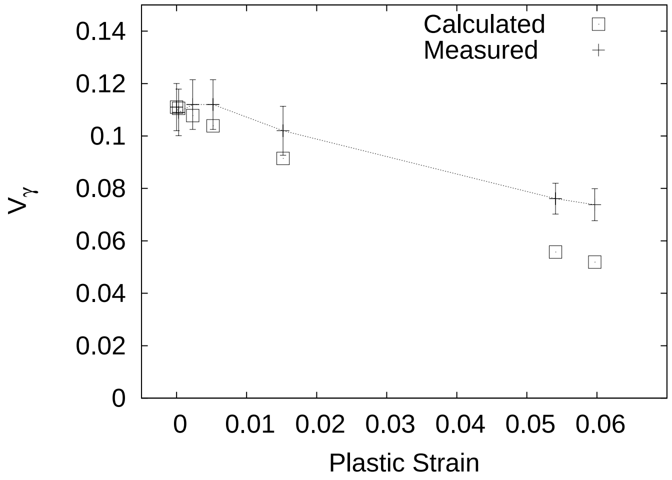

Figure B.3: Application of Sherif *et al.* model to experimental data from [184].

Applicability to Fully Bainitic Steels

Since Sherif *et al.* model has been successful in predicting austenite mechanical stability in TRIP-aided steels, it was believed important to test the model's validity in a different class of steels, for example the current bainitic steels. In principle, the model assesses austenite decomposition on the basis of its chemical free energy. Therefore, it was anticipated that the model would be successful with other steel systems. Figure B.4 shows a reproduction of experimental data previously presented in Chapter 3, with the model's predictions. $\Delta G^{\alpha'\gamma}$ values were 1166, 2165 and 2549 J mol^{-1} for samples transformed to bainite at 300, 250 and 200°C respectively.

As shown in figure B.4(a), the predictions were excellent except at the fracture strain where the model under-estimated the austenite content. It is apparent that the predictions were less successful in samples transformed at lower bainite transformation temperatures.

Since the model does not account for the heterogeneity in mechanical behaviour of individual phases, it is bound to over-estimate austenite content where the austenite grains are embedded within stronger matrix since the austenite in this case sustains greater plastic strain [185]. As previously mentioned throughout this work, bainite transformed at lower temperature is finer and stronger having higher dislocation density.

This explains the success of the model when applied to TRIP-aided steels since the allotriomorphic-ferrite matrix in that type of steels is softer than the austenite. This under-estimates the austenite content. On the other hand, at a given macroscopic plastic strain level, the austenite is under greater stress which is not accounted for in the free energy term in the model, leading to under-estimation of the free energy consequently over-estimation of the austenite content. Interestingly, it seems that these two inaccuracies in the model cancel out each other.

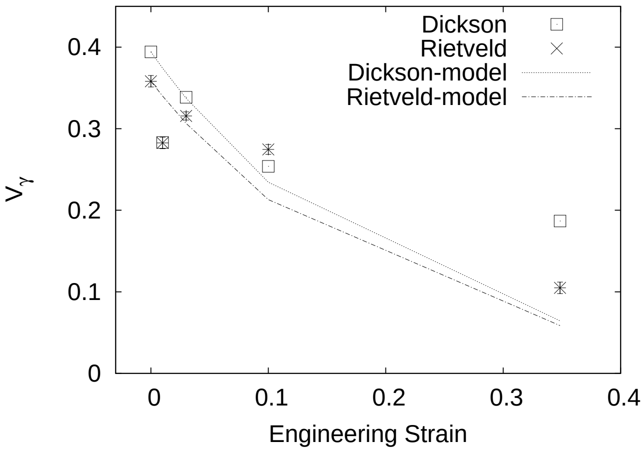

(a) Bainite transformation temperature 300°C

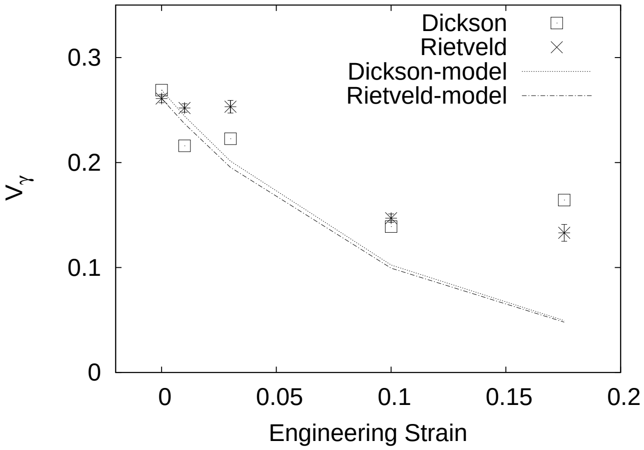

(b) Bainite transformation temperature 250°C

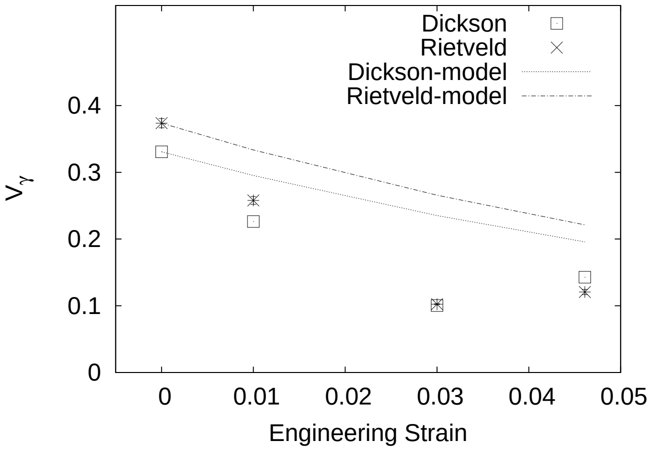

(c) Bainite transformation temperature 200°C

Figure B.4: Experimental and calculated austenite fractions *vs* plastic strain in steel Sp9c.

B.2 Summary

The model proposed by Sherif *et al.* can adequately be used for assessing the austenite mechanical stability in a wide range of TRIP-aided steels. The applicability to fully bainitic steels has been demonstrated.

The weaknesses of the model in terms of the absence of a mechanical contribution to the driving force for the martensitic transformation and the effect of phases other than the austenite have been identified.

Nevertheless, the model seems to be sufficient for TRIP-aided steels.

Bibliography

[1] H. K. D. H. Bhadeshia. *Bainite in Steels*. IOM Communications Ltd, London, second edition, 2001.

[2] M. Takahashi and H. K. D. H. Bhadeshia. *Mater. Sci. Tech.-Lond.*, 6:592–603, 1990.

[3] H. K. D. H. Bhadeshia. A rationalisation of shear transformations in steels. *Acta Metall.*, 29:1117–1130, 1981.

[4] M. Hillert. Paradigm shift for bainite. *Scripta Mater.*, 47:175–180, 2002.

[5] J. M. Oblak and R. F. Hehemann. pages 15–30. Climax Molybdenum Co, Ann Arbor, MI, 1967.

[6] A. Hultgren. *Trans. ASM*, 39:915, 1947.

[7] H. I. Aaronson, J. M. Rigsbee, B. C. Muddle, and J. F. Nie. Aspects of the surface relief definition of bainite. *Scripta Mater.*, 47:207–212, 2002.

[8] G. B. Olson, H. K. D. H. Bhadeshia, and M. Cohen. Coupled diffusional/displacive transformations. *Acta Metall.*, 37:381–390, 1989.

[9] J. Speer, D. K. Matlock, B. C. De Cooman, and J. G. Schroth. Carbon partitioning into austenite after martensite transformation. *Acta Mater.*, 51:2611–2622, 2003.

[10] J. G. Speer, D. V. Edmonds, F. C. Rizzo, and D. K. Matlock. Partitioning of carbon from supersaturated plates of ferrite, with applica-

tion to steel processing and fundamentals of the bainite transformation. *Curr. Opin. Solid State Mater. Sci.*, 8:219–237, 2004.

[11] B. C. Muddle and J. F. Nie. Formation of bainite as a diffusional-displacive phase transformation. *Scripta Mater.*, 47:187–192, 2002.

[12] A. Saha, G. Ghosh, and G. B. Olson. An assessment of interfacial dissipation effects at reconstructive ferrite-austenite interfaces. *Acta Mater.*, 53:141–149, 2005.

[13] C. Zener. Kinetics of the decomposition of austenite. *Trans. AIME*, 167:550–595, 1946.

[14] H. K. D. H. Bhadeshia and A. R. Waugh. Bainite: An atom-probe study of the incomplete reaction phenomenon. *Acta Metall.*, 30:775–784, 1982.

[15] C. García-Mateo, F. G. Caballero, and H. K. D. H. Bhadeshia. Development of hard bainite. *ISIJ Int.*, 43:1238–1243, 2003.

[16] R. W. K. Honeycombe and H. K. D. H. Bhadeshia. *Steels, Microstructure and Properties.* Edward Arnold, London, second edition, 1995.

[17] H. K. D. H. Bhadeshia. Steels for rails. In *Encyclopedia of Materials: Science and Technology*, pages 1–7. Elsevier Science Ltd., 2002.

[18] H. I. Aaronson, H. A. Domian, and G. M. Pound. Thermodynamics of the austenite-proeutectoid ferrite transformation: Fe-C alloys. *TMS AIME*, 236:753–767, 1966.

[19] D. Quidort and O. Bouaziz. The bainite transformation stage in the processing of TRIP-aided sheet steels. *Can. Metall. Q.*, 43:25–33, 2004.

[20] F. G. Caballero and H. K. D. H. Bhadeshia. Very strong bainite. *Curr. Opin. Solid State Mater. Sci.*, 8:251–257, 2004.

[21] K. Tsuzaki, A. Kodai, and T. Maki. Formation mechanism of bainitic ferrite in an Fe-2 Pct Si-0.6 Pct C alloy. *Metall. Mater. Trans. A*, 25:2009–2016, 1994.

[22] L. C. Chang. Bainite transformation temperatures in high-silicon steels. *Metall. Mater. Trans. A*, 30:909–916, 1999.

[23] J. Mahieu. *Contribution to The Physical Metallurgy of Crash-resistant Galvanized TRIP-assisted Steel for Automotive Structures*. PhD thesis, Ghent University, 2003.

[24] P. J. Jacques, E. Girault, A. Mertens, B. Verlinden, J. van Humbeeck, and F. Delannay. The developments of cold-rolled TRIP-assisted multiphase steels. Al-alloyed TRIP-assisted multiphase steels. *ISIJ Int.*, 41:1068–1074, 2001.

[25] A. Mertens, P. J. Jacques, L. Zhao, S. O. Kruijver, J. Sietsma, and F. Delannay. On the influence of aluminium and silicon contents on the kinetics of bainite transformation of intercritical austenite. *J. Phys. IV*, 112:305–308, 2003.

[26] M. F. Gallagher, J. G. Speer, D. K. Matlock, and N. M. Fonstein. In *44^{th} Mechanical Working and Steel Processing Conference Proceedings*, volume 40, pages 153–172, USA, 2002. Iron and Steel Society/AIME.

[27] S. Traint, A. Pichler, R. Tikal, P. Stiaszny, and E. A. Wemer. In *42^{nd} Mechanical Working and Steel Processing Conference Proceedings*, volume 38, pages 549–561, USA, 2000. Iron and Steel Society/AIME.

[28] A. Pichler, P. Stiaszny, R. Potzinger, R. Tikal, and E. Wemer. In *40^{th} Mechanical Working and Steel Processing Conference Proceedings*, volume 36, pages 259–274, USA, October 1998. Iron and Steel Society/AIME.

[29] J. Wang and S. van der Zwaag. Theoritical study of P-containing transformation-induced plasticity steel – part 2: Analysis of the potential TRIP effect. *Z. Metallkd.*, 92:1306–1311, 2001.

[30] J. Wang and S. van der Zwaag. Theoritical study of P-containing transformation-induced plasticity steel – part 1: Determination of the phosphorus concentration. *Z. Metallkd.*, 92:1299–1305, 2001.

[31] M. Bouet, J. Root, E. Es-Sadiqui, and S. Yue. In *40th MWSP conference proceedings*, volume 36, pages 675–684, USA, 1998. Iron and Steel Society/AIME.

[32] M. Bouet, J. Root, E. Es-Sadiqui, and S. Yue. *Mater. Sci. Forum*, 284–286:319–326, 1998.

[33] P. Jacques, X. Cornet, Ph. Harlet, J. Ladrière, and F. Delannay. Enhancement of the mechanical properties of a low-carbon, low-silicon steel by formation of a multiphased microstructure containing retained austenite. *Metall. Mater. Trans. A*, 29:2383–2393, 1998.

[34] A. Z. Hanzaki, P. D. Hodgson, and S. Yue. The influence of bainite on retained austenite characteristics in Si-Mn TRIP steels. *ISIJ Int.*, 35:79–85, 1995.

[35] I. Tsukatani, S. Hashimoto, and T. Inoue. Effect of silicon and manganese addition on mechanical properties of high-strength hot-rolled sheet steel containing retained austenite. *ISIJ Int.*, 31:992–1000, 1991.

[36] H. C. Chen, H. Era, and M. Shimizu. Effect of phosphorus on the formation of retained austenite and mechanical properties in Si-containing low-carbon steel sheet. *Metall. Trans. A*, 20:437–445, 1989.

[37] M. De Meyer, D. Vanderschueren, and B. C. De Cooman. The influence of the substitution of Si by Al on the properties of cold rolled C-Mn-Si TRIP steels. *ISIJ Int.*, 39:813–822, 1999.

[38] H. Matsuda, F. Kitano, K. Hasegawa, T. Urabe, and Y. Hosoya. Metallurgy of continuously annealed high strength TRIP steel sheet. In B. C. De Cooman, editor, *International Conference on TRIP-aided High Strength Ferrous Alloys*, pages 113–119, Ghent, 2002.

[39] A. Pichler and P. Stiaszny. TRIP steel with reduced silicon content. *Steel Res.*, 70:459–465, 1999.

[40] S. Traint, A. Pichler, P. Stiaszny, K. Spiradek-Hahn, and E. A. Werner. Mechanical properties and phase transformations of an aluminum al-

loyed TRIP steel. In *43^{rd} MWSP conference proceedings, ISS*, pages 449–467, 2001.

[41] Y. Sakuma, O. Matsumura, and H. Takechi. Mechanical properties and retained austenite in intercritically heat-treated bainite-transformed steel and their variation with Si and Mn additions. *Metall. Trans. A*, 22:489–498, 1991.

[42] P. J. Jacques. Experimental investigation of the influence of the austenite grain size on the mechanism and kinetics of the bainite transformation in steels. *J. Phys. IV*, 112:297–300, 2003.

[43] P. J. Jacques, E. Girault, T. Catlin, N. Geerlofs, T. Kop, S. van der Zwaag, and F. Delannay. Bainite transformation of low carbon Mn-Si TRIP-assisted multiphase steels: influence of silicon content on cementite precipitation and austenite retention. *Mater. Sci. Eng. A*, 273–275:475–479, 1999.

[44] K.-i. Sugimoto, M. Misu, M. Kobayashi, and H. Shirasawa. Effects of second phase morphology on retained austenite morphology and tensile properties in a TRIP-aided Dual-phase steel sheet. *ISIJ Int.*, 33:775–782, 1993.

[45] A. Z. Hanzaki, P. D. Hodgson, and S. Yue. Retained austenite characteristics in thermodynamically processed Si-Mn transformation-induced plasticity steels. *Metall. Mater. Trans. A*, 28:2405–2414, 1997.

[46] K. K. Park, S. T. Oh, S. M. Baeck, D.-I. Kim, J. H. Han, H. N. Han, S.-H. Park, C. G. Lee, S.-J. Kim, and K. H. Oh. *In Situ* deformation behavior of retained austenite in TRIP steel. *Mater. Sci. Forum*, 408–412:571–576, 2002.

[47] H. K. D. H. Bhadeshia and D. V. Edmonds. Bainite in silicon steels: new composition-property approach Part 2. *Met. Sci.*, 17:420–425, 1983.

[48] W. C. Jeong, D. K. Matlock, and G. Krauss. Observation of deformation and transformation behavior of retained austenite in a 0.14C-

1.2Si-1.5Mn steel with ferrite-bainite-austenite structure. *Mater. Sci. Eng. A*, 165:1–8, 1993.

[49] H. K. D. H. Bhadeshia and D. V. Edmonds. Bainite in silicon steels: new composition-property approach Part 1. *Met. Sci.*, 17:411–419, 1983.

[50] V. F. Zackay, E. R. Parker, D. Fahr, and R. Bush. The enhancement of ductility in high-strength steels. *T. Am. Soc. Metal.*, 60:252–259, 1967.

[51] O. Matsumura, Y. Sakuma, and H. Takechi. Enhancement of elongation by retained austenite in intercritical annealed 0.4C-1.5Si-0.8Mn steel. *Trans. ISIJ*, 27:570–579, 1987.

[52] O. Matsumura, Y. Sakuma, and H. Takechi. TRIP and its kinetic aspects in austempered 0.4C-1.5Si-0.8Mn steel. *Scripta Metall. Mater.*, 21:1301–1306, 1987.

[53] Y. Sakuma, D. K. Matlock, and G. Krauss. Intercritically annealed and isothermally transformed 0.15 pct C steels containing 1.2 pct Si-1.5 pct Mn and 4 pct Ni: Part I. transformation, microstructure, and room-temperature mechanical properties. *Metall. Trans. A*, 23:1221–1232, 1992.

[54] K.-i. Sugimoto, T. Iida, J. Sakaguchi, and T. Kashima. Retained austenite characteristics and tensile properties in a TRIP type bainitic sheet steel. *ISIJ Int.*, 40:902–908, 2000.

[55] K.-i. Sugimoto, M. Kobayashi, and S.-i. Hashimoto. Ductility and strain-induced transformation in a high-strength transformation-induced plasticity-aided dual-phase steel. *Metall. Trans. A*, 23:3085–3091, 1992.

[56] J. Burke. *Kinetics of Phase Transformation in Metals.* Pergamon Press, Oxford, 1965.

[57] V. T. T. Miihkinen and D. V. Edmonds. *Mater. Sci. Tech.-Lond.*, 3:422, 1987.

[58] I. B. Timokhina, P. D. Hodgson, and E. V. Pereloma. Effect of microstructure on the stability of retained austenite in transformation-induced-plasticity steels. *Metall. Mater. Trans. A*, 35:2331–2343, 2004.

[59] H. K. D. H. Bhadeshia and D. V. Edmonds. The mechanism of bainite formation in steels. *Acta Metall.*, 28:1265–1273, 1980.

[60] P. J. Jacques, J. Ladrière, and F. Delannay. On the influence of interactions between phases on the mechanical stability of retained austenite in transformation-induced plasticity multiphase steels. *Metall. Mater. Trans. A*, 32:2759–2768, 2001.

[61] P. Jacques, Q. Furnémont, A. Mertens, and F. Delannay. On the sources of work hardening in multiphase steels assisted by transformation-induced plasticity. *Philos. Mag. A*, 81:1789–1812, 2001.

[62] P. J. Jacques, E. Girault, Ph. Harlet, and F. Delannay. The developments of Cold-rolled TRIP-assisted multiphase steels. Low silicon TRIP-assisted multiphase steels. *ISIJ Int.*, 41:1061–1067, 2001.

[63] Y. Sakuma, O. Matsumura, and O. Akisue. Influence of C content and annealing temperature on microstructure and mechanical properties of 400°C transformed steel containing retained austenite. *ISIJ Int.*, 31:1348–1353, 1991.

[64] A. Perlade, O. Bouaziz, and Q. Furnémont. A physically based model for TRIP-aided carbon steels behaviour. *Mater. Sci. Eng. A*, 356:145–152, 2003.

[65] H. K. D. H. Bhadeshia. TRIP-assisted steels? *ISIJ Int.*, 42:1059–1060, 2002.

[66] R. Rodríguez and I. Gutiérrez. Mechanical behaviour of steels with mixed microstructures. In *2^{nd} International Conference on Thermo-*

mechanical Processing of Steels, TMP'2004, pages 356–363, Liege, Belgium, June 15–17 2004. Verlag Stahleisen GmbH, Düsseldorf.

[67] S. Bandoh, O. Matsumura, and Y. Sakuma. *Trans. ISIJ*, 28:569, 1988.

[68] M. Imagumbai, R. Chijiiwa, N. Aikawa, M. Nagumo, H. Homma, S. Matsuda, and H. Mimura. *HSLA Steels: Metallurgy and Applications*, page 557. ASM International, Ohio, 1985.

[69] K. Yamamoto, S. Matsuda, T. Haze, R. Chijiiwa, and H. Mimura. *Residual and Unspecified Elements in Steel*. ASM International, Ohio, November 1987.

[70] R. Chijiiwa, H. Tamehiro, M. Hirai, H. Matsuda, and H. Mimura. In *Offshore Mechanics and Arctic Engineering Conference (OMAE)*, page 1, Houston, Texas, 1988.

[71] K. Nishioka and H. Tamehiro. In *Microalloying '88: International Symposium on Applications of HSLA Steel*, page 1, Chicago, Illinois, September 1988.

[72] H. K. D. H. Bhadeshia. *Steel Technology International*. Sterling Publications International Ltd., London, 1989.

[73] Y. Tomita and K. Okabayashi. *Metall. Trans. A*, 14:485, 1983.

[74] Y. Tomita and K. Okabayashi. *Metall. Trans. A*, 16:73, 1985.

[75] V. T. T. Miihkinen and D. V. Edmonds. *Mater. Sci. Tech.-Lond.*, 3:432, 1987.

[76] V. T. T. Miihkinen and D. V. Edmonds. *Mater. Sci. Tech.-Lond.*, 3:441, 1987.

[77] K. J. Irvine and F. B. Pickering. *ISI Spec. Rep.*, 93:110–125, 1965.

[78] K. J. Irvine, F. B. Pickering, W. C. Heselwood, and M. Atkins. *JISI*, 195:54–67, 1957.

[79] P. Bowen, S. G. Druce, and J. F. Knott. *Acta Metall.*, 34:1121–1131, 1986.

[80] K. J. Irvine and F. B. Pickering. *JISI*, 201:518–531, 1963.

[81] R. Devanathan and P. Clayton. Rolling/sliding wear behaviour of three bainitic steels. Private communication, 1990.

[82] F. B. Pickering. *Physical Metallurgy and The Design of Steels*. Applied Science Publishers, England, 1978.

[83] J. Sun, H. Lu, and M. Kang. *Metall. Trans. A*, 23:2483, 1992.

[84] Y. Tomita. *J. Mater. Sci.*, 29:2605, 1994.

[85] G. Thomas. *Metall. Trans. A*, 9:331, 1978.

[86] J. Deliry. *Mém. Sci. Rev. Métall.*, 62:524, 1965.

[87] H. K. D. H. Bhadeshia and D. V. Edmonds. *Metall. Trans. A*, 10:895, 1979.

[88] R. Valiev. Nanomaterial advantage. *Nature*, 419:887–889, 2002.

[89] Y. Wang, M. Chen, F. Zhou, and E. Ma. High tensile ductility in a nanostructured metal. *Nature*, 419:912–915, 2002.

[90] R. Z. Valiev, R. K. Islamgaliev, and I. V. Alexandrov. Bulk nanostructured materials from severe plastic deformation. *Prog. Mater Sci.*, 45:103–189, 2000.

[91] F. G. Caballero, H. K. D. H. Bhadeshia, K. J. A. Mawella, and D. G. Jones. Very strong low temperature bainite. *Mater. Sci. Tech.-Lond.*, 18:279–284, 2002.

[92] B. P. J. Sandvik and H. P. Nevalainen. Structure-property relationships in commercial low-alloy bainitic-austenitic steel with high strength, ductility, and toughness. *Metal. Tech.*, pages 213–220, June 1981.

[93] L. C. Chang and H. K. D. H. Bhadeshia. Austenite films in bainitic microstructures. *Mater. Sci. Tech.-Lond.*, 11:874–881, 1995.

[94] F. B. Pickering. *Transformation and Hardenability in Steels.* Climax Molybdenum Corporation, Michigan, 1967.

[95] V. M. Pivovarov, I. A. Tananko, and A. A. Levechenko. *Phys. Met. Metallogr.*, 33:116, 1972.

[96] F. G. Caballero, H. K. D. H. Bhadeshia, K. J. A. Mawella, D. G. Jones, and P. Brown. Design of novel high strength bainitic steels: Part 1. *Mater. Sci. Tech.-Lond.*, 17:512–516, 2001.

[97] F. G. Caballero, H. K. D. H. Bhadeshia, K. J. A. Mawella, D. G. Jones, and P. Brown. Design of novel high strength bainitic steels: Part 2. *Mater. Sci. Tech.-Lond.*, 17:517–522, 2001.

[98] R. Hammond. *Shock and Ballistic Properties of Bainitic Steels.* PhD thesis, University of Cambridge, June 2004.

[99] D. A. Porter and K. E. Easterling. *Phase Transformations in Metals and Alloys.* Chapman and Hall, London, second edition, 1981.

[100] Y. Tomita and K. Morioka. Effect of microstructure on transformation-induced plasticity of silicon-containing low-alloy steel. *Mater. Charact.*, 38:243–250, 1997.

[101] C. G. Lee, S.-J. Kim, T.-H. Lee, and S. Lee. Effects of volume fraction and stability of retained austenite on formability in a 0.1C-1.5Si-1.5Mn-0.5Cu TRIP-aided cold-rolled steel sheet. *Mater. Sci. Eng. A*, 371:16–23, 2004.

[102] M. Peet, S. S. Babu, M. K. Miller, and H. K. D. H. Bhadeshia. Three-dimensional atom probe analysis of carbon distribution in low-temperature bainite. *Scripta Mater.*, 50:1277–1281, 2004.

[103] W. Steven and A. J. Haynes. *JISI*, 183:349–359, 1956.

[104] M. Y. Sherif. Strain-induced transformation of very strong metal. Master's thesis, University of Cambridge, August 2003.

[105] B. Pickering. volume 7 of *Materials Science and Technology.* 1991.

[106] C. García-Mateo, F. G. Caballero, and H. K. D. H. Bhadeshia. Low temperature bainite. In *International Conference on Martensitic Transformations, ICOMAT'02*, Helsinki, Finland, 2002.

[107] C. García-Mateo, F. G. Caballero, and H. K. D. H. Bhadeshia. Acceleration of low-temperature bainite. *ISIJ Int.*, 43:1821–1825, 2003.

[108] H. K. D. H. Bhadeshia. `map_steel_mucg73`. Materials Algorithms Project (MAP), http://www.msm.cam.ac.uk/map/. Phase Transformations Group, Department of Materials Science and Metallurgy, University of Cambridge, Cambridge, UK.

[109] C. García-Mateo and H. K. D. H. Bhadeshia. Mechanical properties of low-temperature bainite. 2003.

[110] Z. Zhao, C. Liu, Y. Liu, and D. O. Northwood. A new emperical formula for the bainite upper temperature limit of steel. *J. Mater. Sci.*, 36:5045–5056, 2001.

[111] C. García-Mateo. Unpublished research, 2003.

[112] W. Parrish. In A. J. C. Wilson, editor, *International Tables for Crystallography*, volume C, pages 46–66. Kluwer Academic Publishers, 1992.

[113] R. Jenkins and R. L. Snyder. *Introduction to X-ray Powder Diffractometry.* John Wiley & Sons, New York, 1996.

[114] A. J. C. Wilson. *J. Sci. Instr.*, 27:321, 1950.

[115] C. Dong, F. Wu, and H. Chen. Correction of zero shift in powder diffraction patterns using the reflection-pair method. *J. Appl. Crystallogr.*, 32:850–853, 1999.

[116] M. U. Cohen. *Rev. Sci. Instrum.*, 6:68–74, 1935.

[117] H. P. Klug and L. E. Alexander. *X-ray Diffraction Procedures.* John Wiley & Sons, New York, 1954.

[118] B. D. Cullity and S. R. Stock. *Elements of X-ray Diffraction.* Prentice Hall, New Jersey, third edition, 2001.

[119] L. V. Azároff and M. J. Buerger. *The Powder Method in X-ray Crystallography.* McGraw-Hill, 1958.

[120] H. Toraya and M. Kitamura. Simultaneous peak-shift correction in the least-squares determination of unit-cell parameters of a sample with standard reference material. *J. Appl. Crystallogr.*, 23:282–285, 1990.

[121] G. S. Smith and R. L. Snyder. f_n: A criterion for rating powder diffraction patterns and evaluating the reliability of powder-pattern indexing. *J. Appl. Crystallogr.*, 12:60–65, 1979.

[122] G. Caglioti, A. Paoletti, and F. P. Ricci. Choice of collimators for a crystal spectrometer for neutron diffraction. *Nucl. Instrum.*, 3:223–228, 1958.

[123] R. A. Young, editor. *The Rietveld Method.* Number 5 in IUCr Monographs on Crystallography. Oxford University Press, 1993.

[124] A. L. Ortiz and L. Shaw. X-ray diffraction analysis of a severely plastically deformed aluminum alloy. *Acta Mater.*, 52:2185–2197, 2004.

[125] J. I. Langford, A. Boultif, J. P. Auffrédic, and D. Louër. The use of pattern decomposition to study the combined X-ray diffraction effects of crystallite size and stacking faults in ex-oxalate zinc oxide. *J. Appl. Crystallogr.*, 26:22–33, 1993.

[126] W. H. Hall. *Proc. Phys. Soc. A*, 62:741, 1949.

[127] G. K. Williamson and W. H. Hall. X-ray line broadening from filed aluminium and wolfram. *Acta Metall.*, 1:22–31, 1953.

[128] C. Suryanarayana. Mechanical alloying and milling. *Prog. Mater Sci.*, 46:1–184, 2001.

[129] A. M. Streicher-Clarke, J. G. Speer, D. K. Matlock, B. C. DeCooman, and D. L. Williamson. Analysis of lattice parameter changes following deformation of a 0.19C-1.63Si-1.59Mn transformation-induced plasticity sheet steel. *Metall. Mater. Trans. A*, 36:907–918, 2005.

[130] M. R. Daymond, M. A. M. Bourke, R. B. Von Dreele, B. Clausen, and T. Lorentzen. Use of Rietveld refinement for elastic macrostrain determination and for evaluation of plastic strain history from diffraction spectra. *J. Appl. Phys.*, 82:1554–1562, 1997.

[131] I. C. Noyan and J. B. Cohen, editors. *Residual Stress.* Springer-Verlag, New York, 1987.

[132] A. Itami, M. Takahashi, and K. Ushioda. Plastic stability of retained austenite in the cold-rolled 0.14%C-1.9%Si-1.7%Mn sheet steel. *ISIJ Int.*, 35:1121–1127, 1995.

[133] K.-i. Sugimoto, M. Kobayashi, and S. Yasuki. *Metall. Mater. Trans. A*, 28:2637–2644, 1997.

[134] S.-M. Song, K.-i. Sugimoto, S. Kandaka, A. Futamura, M. Kobayashi, and S. Masuda. Effects of prestraining on high-cycle fatigue strength of high-strength low alloy TRIP-aided steels. *Mater. Sci. Res. Int.*, 9:223–229, 2003.

[135] Yu. V. Taran, M. R. Daymond, and J. Schreiber. Interplay of stresses induced by phase transformation and plastic deformation during cyclic load of austenitic stainless steel. *Physica B*, 350:98–101, 2004.

[136] L. Barbé, K. Conlon, and B. C. De Cooman. Characterization of the metastable austenite in low-alloy FeCMnSi TRIP-aided steel by neutron diffraction. *Z. Metallkd.*, 93:1217–1227, 2002.

[137] D. E. Kaputkin, L. M. Kaputkina, and S. D. Prokoshkin. Transformation of retained austenite during tempering of high carbon steel. *J. Phys. IV*, 112:275–278, 2003.

[138] C. García-Mateo, M. Peet, F. G. Caballero, and H. K. D. H. Bhadeshia. Tempering of hard mixture of bainitic ferrite and austenite. *Mater. Sci. Tech.-Lond.*, 20:814–818, 2004.

[139] M. J. van Genderen, M. Isac, A. Böttger, and E. J. Mittemeijer. Aging and tempering behavior of iron-nickel-carbon and iron-carbon martensite. *Metall. Mater. Trans. A*, 28:545–561, 1997.

[140] P. V. Morra, A. J. Böttger, and E. J. Mittemeijer. Decomposition of iron-based martensite. A kinetic analysis by means of differential scanning calorimetry and dilatometry. *J. Therm. Anal. Calorim.*, 64:905–914, 2001.

[141] W. C. Leslie. *The Physical Metallurgy of Steels*. McGraw-Hill, New York, 1982.

[142] D. J. Dyson and B. Holmes. *JISI*, 208:469, 1970.

[143] W. B. Pearson. *A Hand Book of Lattice Spacings and Structure of Metals and Alloys*, volume 2. Pergamon Press, London, 1967.

[144] W. Parrish and T. C. Huang. *Adv. X-ray Anal.*, 26:35–44, 1983.

[145] M. Ahtee, M. Nurmela, P. Suortti, and M. Järvinen. Correction for preferred orientation in Rietveld refinement. *J. Appl. Crystallogr.*, 22:261–268, 1989.

[146] K. Yukino and R. Uno. *Jpn. J. Appl. Phys.*, 25:661–666, 1986.

[147] G. Will, M. Bellotto, W. Parrish, and M. Hart. Crystal structures of quartz and magnesium germanate by profile analysis of Synchrotron-radiation high-resolution powder data. *J. Appl. Crystallogr.*, 21:182–191, 1988.

[148] W. A. Dollase. Correction of intensities for preferred orientation in powder diffractometry: Application of the March model. *J. Appl. Crystallogr.*, 19:267–272, 1986.

[149] A. March. *Z. Kristallogr.*, 81:285–297, 1932.

[150] M. J. Dickson. The significance of texture parameters in phase analysis by X-ray diffraction. *J. Appl. Crystallogr.*, 2:176–180, 1969.

[151] R. J. Hill and C. J. Howard. Quantitative phase analysis from neutron powder diffraction data using the Rietveld method. *J. Appl. Crystallogr.*, 20:467–474, 1987.

[152] B. E. Warren, editor. *X-ray Diffraction.* Dover Publications, New York, 1990.

[153] P. J. Jacques. Transformation-induced plasticity for high strength formable steels. *Curr. Opin. Solid State Mater. Sci.*, 8:259–265, 2004.

[154] A. K. Sachdev. Effect of retained austenite on the yielding and deformation behaviour of a dual phase steel. *Acta Metall.*, 31:2037–2042, 1983.

[155] M. Y. Sherif, C. García-Mateo, T. Sourmail, and H. K. D. H. Bhadeshia. Stability of retained austenite in TRIP-assisted steels. *Mater. Sci. Tech.-Lond.*, 20:319–322, 2004.

[156] D. Kalish, S. A. Kulin, and M. Cohen. Bainitic structures and thermomechanical treatments applied to steel. *JOM*, pages 157–164, 1965.

[157] D. Kalish, M. Cohen, and S. A. Kulin. Strain tempering of bainite in 9Ni-4Co-0.45C steel. *J. Mater.*, 5:169–183, 1970.

[158] M. K. Fondekar, A. M. Rao, and A. K. Mallik. Strain tempering of bainite. *Metall. Trans.*, 1:885–890, 1970.

[159] M. T. Hutchings, P. J. Withers, T. M. Holden, and T. Lorentzen. *Introduction to the Characterization of Residual Stress by Neutron Diffraction.* Taylor & Francis, 2005.

[160] E. C. Oliver, P. J. Withers, M. R. Daymond, S. Ueta, and T. Mori. Neutron-diffraction study of stress-induced martensitic transformation in TRIP steel. *Appl. Phys. A*, 74[Suppl.]:S1143–S1145, 2002.

[161] Y. Tomota, H. Tokuda, Y. Adachi, M. Wakita, N. Minakawa, A. Moriai, and Y. Morii. Tensile bahavior of TRIP-aided multi-phase steels studied by in situ neutron diffraction. *Acta Mater.*, 52:5737–5745, 2004.

[162] S. Harjo, Y. Tomota, P. Lukáš, D. Neov, M. Vrána, P. Mikula, and M. Ono. *In situ* neutron diffraction study of α-γ Fe-Cr-Ni alloys under tensile deformation. *Acta Mater.*, 49:2471–2479, 2001.

[163] S. J. Matas and R. F. Hehemann. *Trans. Met Soc. AIME*, 221:179–185, 1961.

[164] A. J. Allen, M. Bourke, W. I. F. David, S. Dawes, M. T. Hutchings, A. D. Krawitz, and C. G. Windsor. Effect of elastic anisotropy on the lattice strains in polycristalline metals and composites measured by neutron diffraction. In C. Beck, S. Denis, and A. Simon, editors, *2^{nd} International Conference on Residual Stresses*, pages 78–83. Elsevier Applied Science, 1989.

[165] G. A. Webster, editor. *Polycrystalline Materials—Determinations of Residual Stresses by Neutron Diffraction*. Geneva, 2001. ISO/TTA3 Technology Trends Assessment.

[166] G. W. H. Höhne, W. F. Hemminger, and H.-J. Flammersheim. *Differential Scanning Calorimetry*. Springer-Verlag, second edition, 2003.

[167] K. Han, M. J. van Genderen, A. Böttger, H. W. Zandbergen, and E. J. Mittemeijer. Initial stages of Fe-C martensite decomposition. *Philos. Mag. A*, 81:741–757, 2001.

[168] G. van der Plaats. *Thermochim. Acta*, 72:77–82, 1984.

[169] E. J. Mittemeijer. Analysis of the kinetics of phase transformations. *J. Mater. Sci.*, 27:3977–3987, 1992.

[170] E. Girault, P. Jacques, Ph. Harlet, K. Mols, J. Van Humbeeck, E. Aernoudt, and F. Delannay. Metallographic methods for reveal-

ing the multiphase microstructure of TRIP-assisted steels. *Mater. Charact.*, 40:111–118, 1998.

[171] R. Bagramov, D. Mari, and W. Benoit. Internal friction in a martensitic high-carbon steel. *Philos. Mag. A*, 81:2797–2808, 2001.

[172] M. Gojić, M. Sućeska, and M. Rajić. Thermal analysis of low alloy Cr-Mo steel. *J. Therm. Anal. Calorim.*, 75:947–956, 2004.

[173] M. J. van Genderen, A. Böttger, R. J. Cernik, and E. J. Mittemeijer. *Metall. Mater. Trans. A*, 24:1965, 1993.

[174] G. R. Speich and W. C. Leslie. Tempering of steel. *Metall. Trans.*, 3:1043–1054, 1972.

[175] K. H. Jack. *JISI*, 169:26–36, 1951.

[176] Y. Hirotsu and S. Nagakura. Crystal structure and morphology of the carbide precipitated from martensitic high carbon steel during the first stage of tempering. *Acta Metall.*, 20:645–655, 1972.

[177] Y. Ohmori and I. Tamura. Epsilon carbide precipitation during tempering of plain carbon martensite. *Metall. Trans. A*, 23:2737–2751, 1992.

[178] E. D. Hyam and J. Nutting. *JISI*, 184:148, 1956.

[179] R. H. Larn and J. R. Yang. The effect of compressive deformation of austenite on the bainitic ferrite transformation in Fe-Mn-Si-C steels. *Mater. Sci. Eng. A*, 278:278–291, 2000.

[180] H. K. D. H. Bhadeshia. The bainite transformation: unresolved issues. *Mater. Sci. Eng. A*, 273–275:58–66, 1999.

[181] G. R. Speich, D. S. Dabhowsko, and L. F. Porter. Strength and toughness of Fe-10Ni alloys containing C, Cr, Mo and Co. *Metall. Trans.*, 4:303–315, 1973.

[182] G. B. Olson and M. Cohen. Kinetics of strain-induced martensitic nucleation. *Metall. Trans. A*, 6:791–795, 1975.

[183] M. Radu, J. Valy, A. F. Gourgues, F. Le Strat, and A. Pineau. Continuous magnetic method for quantitative monitoring of martensitic transformation in steels containing metastable austenite. *Scripta Mater.*, 52:525–530, 2005.

[184] L. Zhao, N. M. van der Pers, J. Sietsma, and S. van der Zwaag. In situ X-ray diffraction measurements of deformation-induced austenite martensite transformation in a multiphase TRIP steel. *Mater. Sci. Forum*, 500–501:379–386, 2005.

[185] Q. Furnémont, P. Jacques, T. Pardoen, F. Lani, S. Godet, P. Harlet, K. Conlon, and F. Delannay. In B. C. DeCooman, editor, *Int. Conf. on TRIP-Aided High Strength Ferrous Alloys*, pages 303–309, Aachen, Germany, 2002. Wissenschaftsverlag Mainz GmbH.